Reflection Zone Plates for X-ray Spectroscopy

Dissertation

zur Erlangung des
Doktorgrades der Naturwissenschaften (Dr. rer. nat.)

im Fachbereich Physik
der Freien Universität Berlin

vorgelegt von

Heike Löchel

Berlin, 2016

Erstgutachter: Prof. Dr. Alexei Erko
Zweitgutachter: Prof. Dr. Wolfgang Kuch

Tag der Disputation: 28.04.2017

Contents

1 Introduction

In modern X-ray photon science, a photon transport system with its X-ray optics is the link between the source and the experiment which probes materials on spatial and temporal scales down to nanometers and femtoseconds. With the development of new powerful X-ray sources, such as 4th generation synchrotron sources and X-ray lasers, new requirements for the design of X-ray optics must be defined: multy-dimensional time-space optics. However, reaching these limits is only possible if the optics which monochromatize and focus the photon beam optimally preserve the source brightness, coherence and time characteristics. Even for today's sources, the ability to fully exploit their beam properties is limited by the design and technology of the X-ray optics involved. With the new X-ray sources on the horizon, such as diffraction limited synchrotron radiation sources (DLSRs) and free electron lasers (FELs), a new generation of X-ray optics must be developed. Finally, all these efforts have to be accompanied by the development of integrated optical modeling and design software tools, addressed and maintained specifically for X-ray and UV optics. In this thesis, one of the future optical elements, namely Fresnel reflection optics and its applications, are described.

For the first time, the use of Fresnel reflecting structures for sharp focusing of X-ray radiation was published in pioneer works of Aristov et al. in 1986 [1]. Here for the first time, the use of a combination of Bragg diffraction on multilayer mirrors and Fresnel diffraction on a surface relief which corresponds to Fresnel's zone structures was suggested. Later, the effect of X-ray radiation focusing on such a structure, etched in multilayered mirrors or a perfect silicon (germanium) crystal, was demonstrated experimentally [2]. In practice, the first successful implementation of a Fresnel reflection structure to a synchrotron beamline was done in 1991 at LURE in Orsay [3]. Here, the first micro probe based on the multilayered Bragg-Fresnel lens (BFL) was constructed. The crystal analog of the LURE micro probe was tested later at the ESRF in Grenoble [4]. The LURE micro probe was successfully explored in user operation before the termination of the storage ring in 2005 and produced many published results in the micro fluorescent analysis of materials with synchrotron radiation. At the same time, other research teams paid attention to the dispersive properties of the Bragg-Fresnel reflecting structures. They were applied as spectrometer elements [5] in hard and soft X-ray radiation for spectral analysis of laser - plasma sources [6]. In the case of a soft X-ray range, the effect of full external X-ray reflection from super polished surfaces

was applied, instead of Bragg reflection on a crystal or multilayer. It considerably increased the energy range of a dispersive element due to the polychromatic nature of the reflection from a smooth surface which is not limited by an energy selectivity of Bragg reflection.

With modern developments in methods for the study of ultra-fast material processes with the use of synchrotron radiation, X-ray lasers and laboratory sources, such as high-harmonic generators and laser-plasma sources, the Fresnel reflection optics have found wide application. Unique properties of the reflection Fresnel optics or reflection zone plates (RZP) have been found very useful for the optical schemes with ultra-sensitive spectrometers [7] and ultra-high time resolution optical systems [8]. In addition to the possibility of Fourier time-energy resolution optimization, a combination of reflection, dispersion, and focusing in one element is increasing the transmission efficiency of optical schemes in orders of magnitude, due to the refusal of several additional optical elements for preparation of a parallel beam and its re-focusing.

The first descriptions of a mathematical model of RZPs and the calculation of their aberrational properties were published in 1996 [9]. However, the real design of optical schemes with the application of RZPs became possible only in 2012 with the development of the corresponding option in the ray tracing program RAY-UI [10], used at BESSY II and some other synchrotron radiation centers for the design of X-ray beamlines and optical systems. Since that time, a number of optical schemes was designed with the use of the program, and all calculations showed an ideal coincidence with experimental results on spatial and energy resolution. This program is also used as a basis for the calculation of all X-ray optical schemes done in this work, and it is the first major component of the definition of the RZP design parameters. The subject of this work, the second major component of RZP design, is actually the calculation and design of the Fresnel structure on a surface of a super - the polished substrate. The further analysis of the carried-out experimental tests, determination of the accordance of the calculated parameters and experimental data, serves to optimize the design and precision. A large part of this thesis is devoted to the creation of new algorithms for the calculation of the RZP structures.

The programs written on the basis of these algorithms are applied in the work for the calculation of a number of optical elements for different applications and shapes of focal spots. Additionally, a detailed analysis of experimental results obtained by experiments for spectroscopy and monochromatization with synchrotron and free electron laser sources is given.

In the experimental part of this work, the attention is mainly paid to the study of the dispersive and focusing properties of total external reflection RZPs in the hard X-ray energy range (around 8 keV). The experiments were carried out at the synchrotron radiation sources BESSY II (Berlin) and APS (Chicago). The main goal of this part of the experimental work is the further development of ultra-fast time resolved spectroscopy methods (XANES and EXAFS) in hard X-rays with the parallel registration of a spectrum with a time resolution better than 1 fs. Another remarkable example of a successful RZP application described in this work is the soft X-ray spectroscopy of highly diluted materials in a liquid jet with an excitation by ultra-short pulses of an X-ray free electron laser. The spectrometer based on RZP array shows an order of magnitude higher sensitivity in comparison with conventional X-ray spectrometers.

RZPs are almost ideal optical elements for X-ray lasers and ultra-powerful sources of X-rays. In addition to the three properties as focusing, reflection and dispersion mentioned above, they also show an exclusive radiation and temperature stability. RZPs are made on a massive substrate with the possibility of an effective cooling. It should also be mentioned that for the fabrication of RZPs as described in this work the most advanced methods available at the HZB nanotechnology laboratory were applied.

The thesis is divided into 6 chapters:

After the introduction, the second chapter of this thesis focuses on the theoretical background necessary to understand the physical principals of RZPs and their implementation into science.

The third chapter focuses on the process of the design and calculation of RZPs. Here, the development and mathematical background of the new and advanced calculation program as well as the basic design types of RZP structures are described.

In a short fourth chapter, the typical structure dimensions of RZPs for the hard X-ray range compared with RZPs for the soft X-ray range are given, followed by a short description of the fabrication process.

The fifth chapter is the first of two chapters in the experimental part. Here, the main part of the experimental work of this thesis is described, namely the characterization of the newly developed hard X-ray RZPs. The experiments were done at

synchrotron beamlines at BESSY II in Berlin, Germany and at the APS in Chicago, USA.

In the following experimental chapter, chapter six, the results of another RZP spectrometer characterization and optimization done within the framework of this thesis is shown, this time for an application in the soft X-ray range at the soft X-ray material science (SXR) beamline of the Linac Coherent Light Source (LCLS) in Stanford, USA. These characterization and optimization experiments were conducted at BESSY II beamlines.

The annex includes a mathematical derivations and the source code of the new calculation program.

2 Basic Theory

2.1 Absorption and Fluorescence

When X-rays hit atoms or molecules, they can cause various well-known effects interacting with the electron shells or even the atomic cores. The decrease of the intensity while propagating through matter caused by these effects plays an important role in X-ray optics. Generally, any intensity loss can be described by the Beer-Lambert law as a function of the thickness x of the material:

$$I(x) = I_0 \cdot e^{-\mu x}, \tag{2.1}$$

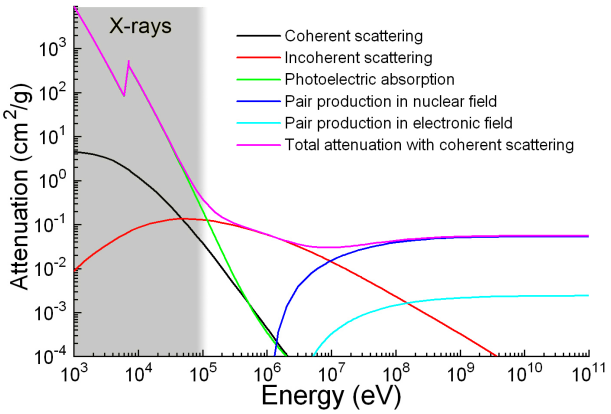

Figure 2.1: Components of the attenuation coefficient for iron depending on the incoming photon energy, with total attenuation shown in pink. The components are each caused by a different interaction effect. Retrieved from [11].

with the intensity I_0 of the incoming light. The linear attenuation coefficient μ can be split into three summands:

$$\mu = \mu_{scatt} + \mu_{photo} + \mu_{pair}, \tag{2.2}$$

which arise from different categories of effects in the material: scattering (μ_{scatt}), photo absorption (μ_{photo}), and pair production (μ_{pair}). The first effect, scattering, can be split into two subcategories. An X-ray quantum can be scattered either coherently or incoherently on a shell electron. The coherent case, also called Rayleigh scattering, mostly occurs at photon energies lower than X-ray energies, when the ionization energy of the electron is much larger than the energy of the X-ray. Here, the photon only changes its direction; its energy remains the same. The effect varies with the atomic number Z of absorber material and incident photon energy E by Z^2/E. In the incoherent case though, called Compton scattering which dominates at higher photon energies up to the gamma ray range, the photon transmits a part of its momentum onto an electron and therefore changes its energy. However, both scattering effects do not cause the main part of the attenuation for X-ray energies. Instead of just deflect-

ing the X-ray, most electrons are removed from the shell. This is called photoelectric effect. Mostly, electrons from the inner atomic shells (K and L shell) are ejected. The discrete energy levels of those strongly bound electrons result in the so called absorption edges, used in absorption spectroscopy. The third summand from equation (2.2), results from the production of electron-positron pairs and also only plays a role in the gamma ray range. Depending on the interacting field (nuclear or electronic), this effect is also parted into two subcategories. For both, threshold energies (the rest energies of the two particles $E_{min} \approx 1.02$ MeV for the interaction with the nuclear field and twice as much $E_{min} \approx 2.04$ MeV for the so called "triplet production", where an electron-positron pair and an electron are emitted) even mark sharp limits, below which these processes are impossible. Figure 2.1 shows the strength of the different components of the attenuation coefficient for iron as a function of the incoming photon energy. For X-rays, especially soft X-rays, the photo effect clearly dominates. The electron loss caused by this effect creates a hole in the atomic shell which is immediately refilled by an electron of an upper level. Within the relaxation, a photon corresponding to the energy difference of the two shell levels is emitted. This phenomenon is called X-ray fluorescence, since the emitted energies also lie in the range of X-rays. These characteristic fluorescence energies yield valuable information about the chemical composition and structure of a (in this case mostly metallic) sample and provide the analytical reason for the construction of fluorescence spectrometers.

2.2 Refraction and Reflection

For X-rays, vacuum is optically denser than any form of matter. Traveling from vacuum onto for example a metal block under an angle, X-rays are refracted towards the metal's surface unlike visible light, which is refracted towards the surface normal. This means that the refractive index n in a medium other than vacuum is actually smaller than $\hat{n} = 1$. For X-rays, the conventional notation is $\hat{n} = 1 - \delta + i\beta$, with the decrement of the real part δ and the imaginary part β describing the absorption index or extinction coefficient. The decrement δ is positive and ranges from 10^{-4} to 10^{-6}, so the difference to the refractive index for vacuum is very small. Still, this results in a phase velocity v higher than the vacuum speed of light c as n is defined as $n = c/v$. This does not break the law of relativity though, only requiring that signals carrying information do not travel faster than light. Such a signal propagates with the group velocity instead of the phase velocity. The group velocity of X-rays in any matter

remains of course still smaller than c. So, if an X-ray passes from vacuum ($\hat{n}_1 = 1$) into matter ($\hat{n}_2 < 1$) with an incoming angle θ_1, as usual, the resulting refractive angle θ_2 is given by Snell's law:

$$\hat{n}_1 \sin\theta_1 = \hat{n}_2 \sin\theta_2, \tag{2.3}$$

with the angles measured between the light rays and the surface normal. Because $\hat{n}_1 > \hat{n}_2$, θ_2 is larger than θ_1. The limit for the refractive angle is $\theta_2 = \pi/2 = 90\,\text{deg}$, so incident angles of incidence larger than $\theta_1 = \arcsin(\hat{n}_2)$ can only cause total external reflection. This effect is taken advantage of when using optical elements like mirrors and total external reflection zone plates, by illuminating these optical elements under very small angles (grazing incidence).

2.3 Diffraction

Equal to electromagnetic waves of other wavelengths, X-rays can be diffracted on periodic structures. On the one hand, these structures can be the internal atomic or molecular layers of crystalline materials or man-made multilayer materials, or, on the other hand they can be implemented onto the surface of a substrate. In the first case, incoming X-rays with an incident angle θ are reflected at different layers in the material and interfere negatively or positively depending on the wavelength λ of the photons, the distance d between the material layers and θ. The condition for positive interference is given by Bragg's law:

$$n\lambda = 2d\sin(\theta), \tag{2.4}$$

with an integer number $n \in \mathbb{N}$. This condition, illustrated in figure 2.2a, is responsible for the shape of the so-called "rocking-curves" of a crystal, which are recorded by rotating the crystal within a certain range of θ and the detector simultaneously by 2θ. In the second case, when electromagnetic waves are diffracted on a surface with periodical structures, the grating equation describes the condition for positive interference:

$$d \cdot (\sin\alpha - \sin\beta) = m\lambda, \tag{2.5}$$

with the structure period d, the incoming angle α, the outgoing angle β and another (positive or negative) integer number $m \in \mathbb{Z}$. Here, several diffraction maxima can be recorded, depending on the outgoing angle of the diffracted light. These are the so-

called diffraction orders, numbered by m. When the period of the surface structures changes depending on the surface coordinate according to a certain principle, these structures can accumulate the positive interference not just in a certain outgoing angle, but in a certain point in space. This is the basic principle of Fresnel zone plates, shown in section 2.4.1.

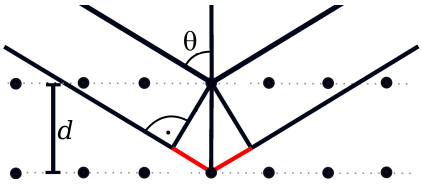

(a) Bragg-condition for positive interference on crystal layers: the sum of the red segments must cause a path difference equal to an integer multiple of the wavelength λ.

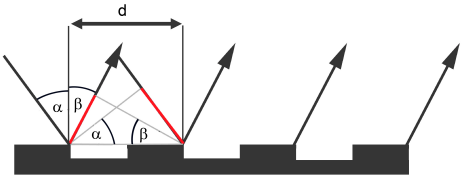

(b) Diffraction on a periodical surface structure: to fulfill the condition for positive diffraction orders (the grating equation 2.5), here, the difference between the red segments must be an integer multiple of λ.

Figure 2.2: Conditions for positive diffraction interference on a) crystal layers and b) a periodical surface structure

2.4 Total External Reflection Zone Plates

Fresnel zone plates are diffractive optical elements that combine the focusing (or imaging) properties of refractive lenses with the dispersive property of diffraction gratings. To understand this multifunctionality, the basic physical principles of Fresnel zones and the resulting geometrical conditions between the light source and diffraction image will be explained in this section. There are many different types of modified zone plates, especially of reflection zone plates used for X-ray spectroscopy, as described in the next chapter. They are all based on the most simple version though, a point-to-point ZP that transfers light from a point source to a detector point.

2.4.1 Point-to-Point Fresnel Zone Plates

Imagine two points A and B in a 3D space. If A is now seen as a light source and B is a detector point, a light ray that travels on a direct straight line from A to B propagated over the shortest possible distance of $\overline{AB}$. Any ray that takes a detour via a point q, has a different phase in B. As long as this phase difference is no larger than $\Phi = \pi$, both rays still interfere positively in B. At a phase difference of $\pi \leq \Phi \leq 2\pi$, the interference is negative. For any phase difference value, there is a matching path

difference Δp that defines an ellipsoid with A and B as foci. This ellipsoid is the set of points q to which the sum of distances $\overline{Aq} + \overline{qB}$ is constantly Δp. The ellipsoids that mark phase differences of integer multiples of π, ($\Phi = n\pi$, with $n \in \mathbb{N}$), equivalent to path differences of

$$\Delta p = n\lambda, \tag{2.6}$$

define certain zones of positive and negative interference. The volumes between two neighboring ellipsoids are the so-called Fresnel zones. If the light emitted in A is blocked in every second Fresnel zone and can not arrive in B, the interference is completely positive and there is a bright spot in B. This is the working principle of Fresnel zone plates (see figure 2.3).

There are two types of ZPs depending on the interaction of the light with the ZP material: transmissive ZPs (TZPs) and reflection ZPs (RZPs). TZPs work, as the name suggests, with the light being transmitted by the ZP material. Therefore, their optical axis, which is defined as the line that runs from A to B via the central point of the zone plate (Fresnel zone center, FZC), remains the direct line from A to B, $\overline{AB} = R_1 + R_2$, with $R_1 = \overline{A, FZC}$ and $R_2 = \overline{FZC, B}$. The zones of a TZP are concentric circles.

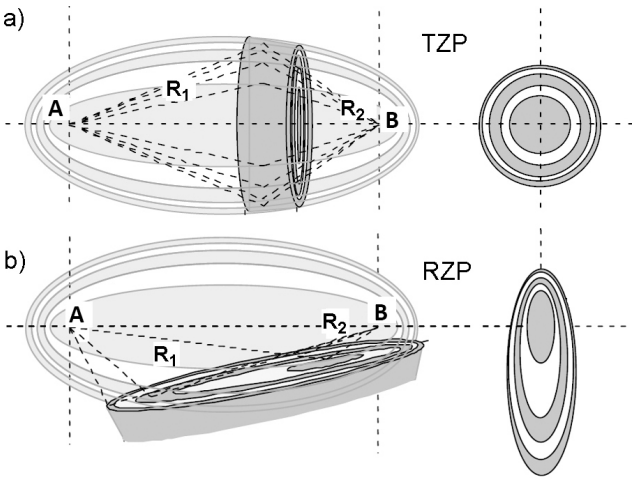

Figure 2.3: Schematical Fresnel zones between two points in space. Fresnel zone edges are ellipsoids with the two points as foci. A TZP is a cut through the direct connecting line between the two foci and an RZP cut does not cross this line [12].

Via chosing materials with appropriate absorption properties, the zones alternatingly absorb or transmit the light. Alternatively, if there is a material that meets these demands, the absorbing parts can be substituted with another material with a refractive index that causes an exact phase shift of π and so lets the second half of the light contribute to the positive interference as well. The phase shift of π is usually regulated via the TZPs thickness.

Reflection zone plates function via reflection instead of transmission. The resulting geometrical difference is that the optical axis does not run straight through the zone plate, but it is bent at the zone plate's center FZC. This means that the FZC is not crossed by the direct connection line between the source and the detector $\overline{AB}$. The

Fresnel zones of an RZP are created by alternating structure heights. In most cases, they have non-centric elliptical shapes (with the only concentric exception $R_1 = R_2$). Compared to TZPs, there is one additional variable - the angle of incidence α. The smaller α, the narrower are the resulting ellipses. For high reflectivities in the X-ray range, very small angles must be used in reality (see section 2.2). As an equivalent to transmission zone plates that shift the phase second half of the light by π instead of blocking it, there is an ideal structure depth t at which this phase shift is caused at the lower structure level (see figure 2.4). Similar to Bragg's law, it is given by

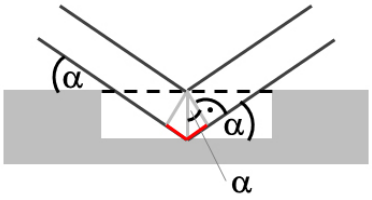

Figure 2.4: Condition for ideal (local) profile depth of an RZP. Depending on the incoming angle α, a certain height difference between the two structure levels causes a phase shift of π compared to the upper level. The path difference between the two rays is shown in red.

$$t = \frac{2n+1}{2}\frac{\lambda}{\sin\alpha}, \tag{2.7}$$

with $n \in \mathbb{N}$, and varies with the incoming angle α. With 3D-etching techniques that will be described in detail in chapter 4, the (usually only slightly varying) structure height can be fitted to the ideal one throughout the whole area of the RZP. Adjusting the profile depth significantly increases the RZP's efficiency.

For the calculation of the Fresnel zone structure of the RZP itself, the path difference condition (2.6) defines all zone edges. Starting at the FZC as 0^{th} zone edge, where the optical path between A and B is $R_1 + R_2$, all points q with $\overline{Aq} = R_1'$ and $\overline{qB} = R_2'$ of a subsequent zone edge must fulfill

$$R_1' + R_2' = R_1 + R_2 + n\lambda. \tag{2.8}$$

This results in an ellipsis functions in the coordinate system of the RZP plane and will be discussed in detail in the next chapter.

2.4.2 Imaging and Dispersion

The characteristic advantage of ZPs is that they can image (which can either mean that they focus or that they magnify) and disperse light from an X-ray source simultaneously. The mathematical background for these properties are two basic equations: the lens equation for the imaging and the grating equation for the dispersion. Using ZP in the reflective geometry, RZPs, and their varying periods complicate these conditions though, compared to normal lenses and diffraction gratings.

Imaging Properties

Like a thin refractive lens, a Fresnel zone plate fulfills the lens equation:

$$\frac{1}{L_1} + \frac{1}{L_2} = \frac{1}{f}, \tag{2.9}$$

with the focal distance f of the ZP. This holds for RZPs as well as TZPs. Other than TZPs, RZPs have an angled optical axis. As a result of the reflection, the image appears mirrored, meaning that compared to the source, it is flipped only horizontally, not vertically and horizontally like a normal lens image (see figure 2.5).

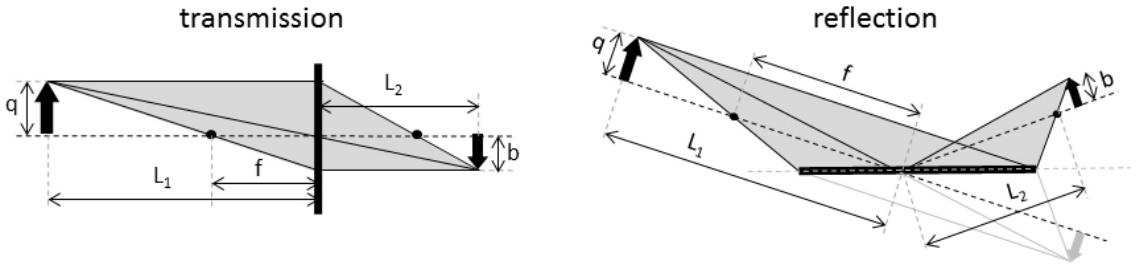

Figure 2.5: Imaging geometry for a transmission ZP (left) and a reflection ZP (right).

For a finite source size, as for refractive lenses, the magnification factor of an RZP is given by the ratio between the focal size Δf and the source size Δs. In vertical direction it is defined as:

$$M_v = \frac{\Delta f_v}{\Delta s_v} = \frac{R_2' \sin\alpha}{R_1' \sin\beta}. \tag{2.10}$$

The first component, R_2'/R_1' is the ratio between entrance and exit arm, equivalent to the magnification factor of a simple thin refractive lens. The second component is the so-called asymmetry factor, caused by the fact that the entrance angle differs from the exit angle. Counter-intuitively enough, in the first component, the source-side quantity is the denominator and in the second component it is the numerator. But with simple geometrical considerations, as shown in figure 2.6, this becomes clear: the two red triangles include the incoming and outgoing angles α und β as well as half of the RZP length L each. The trigonometrical relations

$$\sin\alpha = \frac{a}{L/2} \qquad \text{and} \qquad \sin\beta = \frac{b}{L/2}$$

describe the ratio between the halfs of the RZP length and their projections onto the beam profile, labeled as a and b. To transform the incoming beam profile at the RZP

$2a$ into the outgoing beam profile $2b$, a factor of

$$\frac{2a}{2b} = \frac{\sin\alpha}{\sin\beta}$$

is needed.

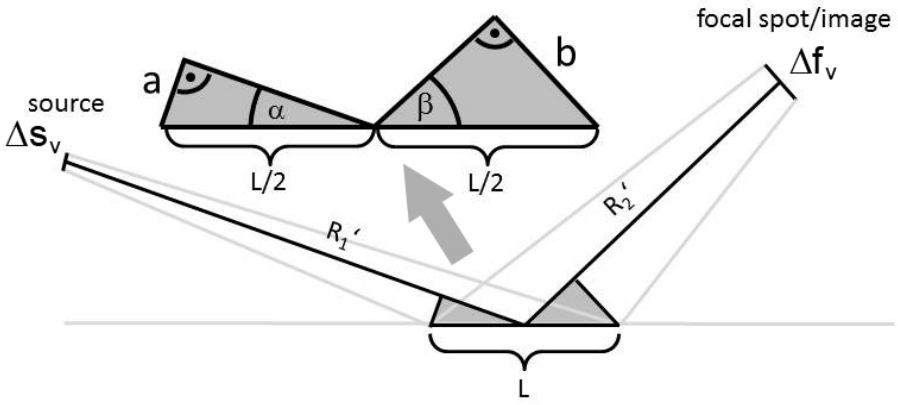

Figure 2.6: Geometrical connections at the FZC of an RZP, illustrated to clarify the asymmetry part of the magnification factor.

However, for RZPs symmetrical to the optical axis, the horizontal magnification factor is not influenced by any angles and therefore remains to the ratio between entrance and exit arm length:

$$M_h = \frac{R_2'}{R_1'}. \tag{2.11}$$

Dispersive Properties of Off-axis RZPs

Unlike normal diffraction gratings that are used at parallel incidence and produce interference minima and maxima depending only on the outgoing angle, ZPs deflect light from one point in space to another. This can only be reached if the period of the grating structure varies with the position on the grating. If the period of the grating is varied in only one direction according to the Fresnel condition (2.8), this results in a so-called varied line spacing (VLS) grating that focuses the incoming light onto a focal line in the detector plane (for

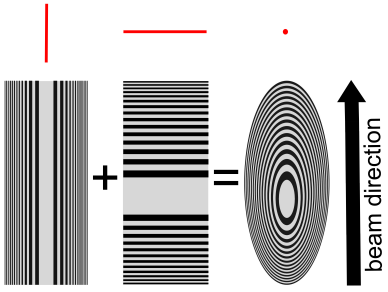

Figure 2.7: Schematical Fresnel zones of meridional VLS, sagittal VLS and RZP with corresponding image lines and points shown above in red. The RZP is an overlay of the two VLS gratings.

larger lateral opening angles the diffraction image differs from a line, see sections 3.8.2 and 3.9.1). Depending on the direction of the period gradient - along the beam (sagittal VLS grating) or orthogonal to the beam (meridional VLS grating) - the focal line will show vertically or horizontally on the detector (see figure 2.7). An RZP can be understood as an overlay of two VLS gratings in these orthogonal directions. For spectroscopic purposes, the gradient along the beam path is used (sagittal grating).

As described above, an RZP is designed for only one particular photon energy. For other photon energies, the position of the detector point changes along the optical axis. So, if the RZP was illuminated around its center, the direction of the dispersion would fall together with the optical axis perpendicular to the detector plane. For an actual spectral decomposition that is visible on the detector, a so-called off-axis segment not including the FZC must be used. This also causes a separation of the different diffraction orders of the RZP in the detector plane. The further away from the FZC, the larger this separation and the larger the energy resolution of the RZP. If the off-axis segment lies between the FZC and the source, the image point appears below the specular reflection in the image plane and if the segment lies on the other side of the FZC, the image point appears above the reflection. In the first case, the image point can be seen as a negative order of diffraction and in the second case as a positive diffraction order.

To calculate the vertical shift Δs of the image point in the detector plane that corresponds to a photon energy E differing from the design energy E_d of the RZP can be derived in a good approximation by using the grating equation for the central grating period d_c of the off-axis RZP segment:

$$\sin(\pi - \alpha) - \sin(\pi - \beta) = \frac{m\lambda}{d_c}, \tag{2.12}$$

with the number m of the diffraction order. The incoming and outgoing angles α and β are here measured between the RZP plane and the incoming beam (usually, the grating equation is used with the angles measured to the RZP surface normal). Solving this equation for β leads to

$$\beta = \arcsin\left(\sin(\pi - \alpha) - \frac{m\lambda}{d}\right) + \pi.$$

Knowing that the perpendicular s from the image point onto the RZP plane (see figure

2.8) is given by

$$s = R_2 \sin\beta, \tag{2.13}$$

and with $\lambda = hc/E$ (h = Planck constant, c = speed of light) this results in a vertical shift between the position s_d of the image point for the design energy and the position s for E of

$$\begin{aligned}\Delta s = s_d - s &= R_2 \arcsin\left(\sin\alpha - \frac{mhc/E_d}{d}\right) + \pi - R_2 \arcsin\left(\sin\alpha - \frac{mhc/E}{d}\right) - \pi \\ &= R_2 \frac{mhc}{d}\left(\frac{1}{E_d} - \frac{1}{E}\right).\end{aligned} \tag{2.14}$$

With this, any unknown energy corresponding to an image point shifted by a certain Δs can be recalculated from the diffraction pattern of the RZP. The intensity of the diffraction orders decreases with $I_m \propto 1/m^2$. Therefore, mostly RZPs for the $\pm 1^{st}$ order of diffraction are used.

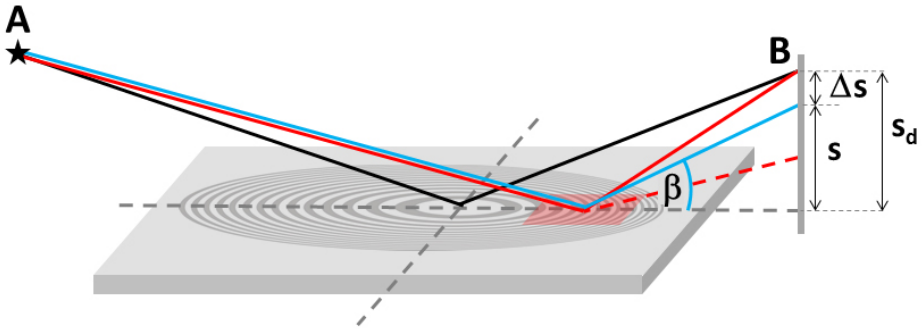

Figure 2.8: Geometrical connections at the FZC of an RZP, illustrated to clarify the asymmetry part of the magnification factor.

Diffraction Image with Multiple Photon Energies

As mentioned above, a single point-to-point RZP is a segment of the plane cut through the three-dimensional Fresnel zones between two points in space. For a vertical energy dispersion on the detector, this segment must be located outside the Fresnel zone center (off-axis) and symmetrical the optical axis projection (the y-axis in the RZP plane). The further away from the FZC, the better the separation between the diffraction orders and hence the better the resolution of the RZP. On the other hand, the outer parts of an RZP have higher line densities which yield less photon throughput and are less easy to fabricate. If the section is located in front of the center (along the beam direction, meaning on the source side of the RZP), the RZP focuses in its -1^{st} diffraction order, and if it is located behind the center, it focuses in its 1^{st} diffraction order. Figure 2.9 shows a CCD camera image, with a typical diffraction image of a 1^{st} order RZP illuminated with soft X-ray fluorescence from a sample containing just a few chemical elements. The 0^{th} order or specular reflection is located in the lower part of the image. The area of the RZP can be seen as darker part enframed by the reflection of the surrounding unstructured substrate. Above the 0^{th} order, a vertical row of 1^{st} order spots of different sizes can be seen. The smallest spot is caused by photons coming in with the design energy of the RZP, so this is the actual focal spot. For all other photon energies the spots are widened both vertically and horizontally. They resemble the circle of confusion of refractive lenses. Therefore, their shape is determined by the shape of the RZP aperture, which is, in this case, a trapeze (see section 3.7.3). Focal spots from lower energies than the design energy appear above the design energy spot, and higher energies appear below. For the analysis of the spectrum, the spectrometer has to be calibrated to apply an energy scale to the vertical position of the spots. Once this is done, any unknown fluorescence signal appearing on this scale can be assigned to its exact energy.

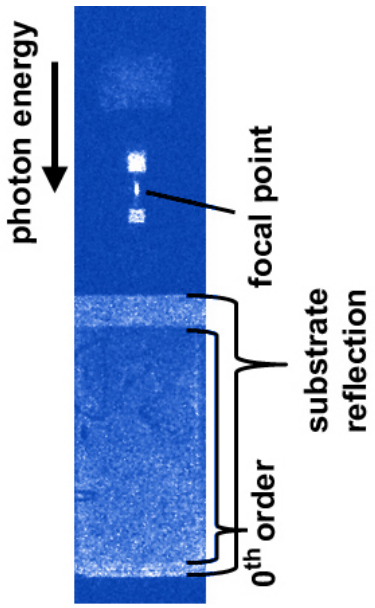

Figure 2.9: a typical diffraction image on a CCD camera with the 0^{th} order and 1^{st} order focal spots.

Diffraction-Limited Spatial Resolution

Via the Rayleigh-criterion, for a perfect point source (diffraction-limited), the spatial resolution Δl of zone plates and with that the minimum size of the focal spot Δf is defined by the width of the outermost zone $\delta r_{n_{max}}$:

$$\Delta f \approx 1.22 \cdot \delta r_{n_{max}}. \tag{2.15}$$

Due to technical fabrication limits for $\delta r_{n_{max}}$, zone plates can only be realized up to a certain aperture, which results in a spatial resolution limit. One of the advantages of RZPs compared to TZPs is the grazing incidence angle. For the same source-detector-geometry, meaning as cuts of the same 3D Fresnel zone ellipsoids, the zone widths of the RZP are much larger than those of the TZP. At an angle of incidence α on the RZP, they differ according to

$$r_n(TZP) = \sin\alpha \cdot r_n(RZP). \tag{2.16}$$

So, for the same setup, an RZP can be fabricated up to more zones, meaning a larger aperture, resulting in a better spatial resolution.

As mentioned above, this only holds for perfect point sources. For realistic source sizes, the focal spot is larger as well, as described further in 3.1.2.

2.4.3 Angle of Acceptance and Numerical Aperture

The angle of acceptance α_{acc} of an RZP is - as shown in figure 2.10 - the angle between the rays that hit the front end of the RZP (at an angle of α_1) and those that hit the back end (at α_2):

$$\alpha_{acc} = \alpha_1 - \alpha_2. \tag{2.17}$$

The numerical aperture NA of a refractive optical system is the dimensionless number that characterizes the angular range over which the system can accept or emit light. For ZPs, it is typically defined as the projected aperture onto a plane perpendicular to the optical axis. For a TZP, this coincides with the normal aperture A, but for RZPs, again, in vertical direction, the angle of incidence comes into play. Here,

$$NA_{vert}(RZP) = A \cdot \sin\alpha, \tag{2.18}$$

is a good approximation for this quantity. In horizontal direction, the numerical aperture is not influenced by angle and hence matches the total width of the RZP.

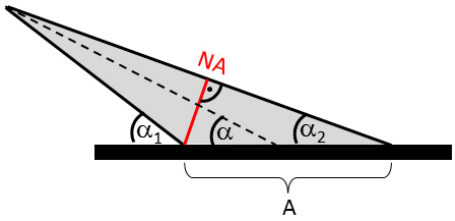

Figure 2.10: Numerical aperture of an RZP in vertical direction at an acceptance angle of $\alpha_2 - \alpha_1$.

2.4.4 Diffraction Limited Depth of Focus

The diffraction-limited depth of focus Δz of a ZP is defined as the permitted distance, away from the focal image plane, at which photon density on the optical axis is diminished by 20%. Mathematically, this is expressed by

$$\Delta z = \pm \frac{1}{2} \frac{\lambda}{(NA)^2}, \tag{2.19}$$

with the numerical aperture NA described above. The mathematical prediction of the real depth of focus depending on a finite source size is very complicated. Here, it is more convenient to rely on ray-tracing programs and other simulation software.

2.4.5 Temporal Elongation

As described above, the path difference between two light rays traveling via two neighboring Fresnel zone edges is equal to one wavelength. This means that in the detector point where the two rays interfere, the time interval between them is $\Delta\tau = \lambda/c$, with the speed of light c. The total time difference between the first and last ray diffracted by the RZP then is equal to

$$\Delta\tau_{tot} = N_{max} \cdot \lambda/c, \tag{2.20}$$

where N_{max} is the total number of Fresnel zones on the RZP. In ultra fast X-ray optics, the incoming light has a specific pulse duration that needs to be maintained. A diffractive optical element elongates the pulse by $\Delta\tau_{tot}$.

2.5 Efficiency Estimation

2.5.1 Theories

The efficiency of a reflective diffraction grating is a very complex quantity influenced by many factors. It is defined as the ratio between the intensity of the diffracted (monochromatic) light into a specific diffraction order m and the intensity of the incident light (absolute efficiency) or the intensity of the specular reflection from a mirror coated with the same material as the grating (relative efficiency).
Basically, there are two different types of efficiency theories: **scalar theories** that simplify the situation with three assumptions:

1. a significantly larger diffracting structure than the wavelength,
2. no polarisation effects and
3. the diffraction phenomena are observed in the far field,

and **vector theories** where Maxwell's equations are used to yield a more accurate determination of the diffraction intensities. Any precise calculation of the efficiency is usually done with a suitable simulation software with numerical methods that use these vector theories, for example the so-called rigorous coupled-wave analysis (RCWA). For a grating with a laminar profile that meets the 3 assumptions of scalar theories though, there is a rather simple formula with which the absolute efficiency in the m^{th} diffraction order $\epsilon(m)$ can be estimated sufficiently:

$$\epsilon(m) = \frac{4}{m^2\pi^2} \sin^2\left(\frac{m\pi g}{d}\right) \sin^2\left(\frac{\pi t}{\lambda}\left(\sin\alpha + \sin\beta_m\right)\right), \tag{2.21}$$

where g is the groove width, d the period, t the profile depth, α the incident angle (measured from the grating surface) and β_m the diffraction angle of the order m as shown in figure 2.11. The two sine factors do not exceed the value 1. Thus, the maximum possible grating efficiency for the $\pm m^{th}$ order is

$$\epsilon(m)_{max} = \frac{4}{m^2\pi^2} = \frac{1}{m^2} \cdot 40\%, \tag{2.22}$$

independent of the grating period and the incoming or outgoing angles.
This equation still describes an ideal case though, with a perfect grating surface and a 100% reflecting material. In a realistic case, the efficiency is decreased by the material

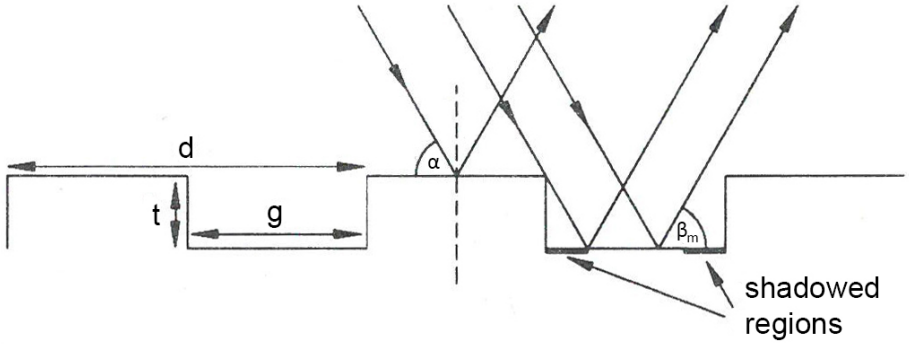

Figure 2.11: Geometry of rectangular profile of a laminar diffraction grating with the shadowed regions shown on the right.

properties.

For RZPs, another factor comes into play as well: since the period varies, the formula above and other efficiency simulation theories only hold for a local grating period at one point of the RZP. Furthermore, at almost all points on the RZP except the symmetry axis in the center, the incoming light rays are not perpendicular to the Fresnel zones. These facts have to be considered for realistic efficiency estimations of RZPs, described in detail in section 3.2. To understand the physical effects that influence the overall efficiency and to estimate the ranges within which these factors can be controlled, the following provides an overview of the same.

2.5.2 Influencing Parameters

Profile Depth and Shape

As mentioned in section 2.4.1, the profile depth of an RZP influences the efficiency significantly. The height difference between lower and upper level of a laminar profile causes a specific phase shift between rays reflected on the two levels. At the ideal profile depth (see equation 2.7), this phase shift is exactly $\Phi = \pi$. For RZPs, this ideal profile depth slightly changes throughout the area of the RZP, depending on the incoming angle.

Other profiles than a laminar one lead to other efficiency values. Usually, simulation programs feature a couple of profile options. The most prominent are sinusodial or blazed profiles. Blazed profiles have the advantage of high efficiencies due to the fact that the triangular shape with an angled surface in every grating unit diffracts the main peak intensity, that is usually deflected into the 0^{th} order, now appears in the diffraction order of interest, mostly the $\pm 1^{st}$. Ideally, the efficiency is then increased

to 100%. Due to their curvature of the zones and the strong variation in line density, for RZPs, a blazed profile is very hard to achieve. A sinusodial profile can arise as a product of etching inaccuracies at very small zone widths in the order of a few ten nanometers. Here, the maximum possible efficiency is only 34%.

Shadowing and Fill Factor

As shown in figure 2.11, there are always regions at the lower level of a grating structure that are not illuminated. An estimation [13] of the shadowed width g_s for any local grating period and profile depth t is given by

$$g_s = t(\cot\alpha + \cot\beta). \tag{2.23}$$

The effective groove width is then

$$g' = g - g_s. \tag{2.24}$$

By changing the so called fill factor f_{fill}, that is given by

$$f_{fill} = \frac{d - g'}{d}, \tag{2.25}$$

the maximal sum of the illuminated area on both structure levels can be optimized accordingly.

Material Properties

Independent of the surface structure, the material that the grating or RZP is made of plays a very important role. The mostly rather complicated interactions between the electromagnetic waves of the incoming X-rays and the electronic shell as well as sometimes the nucleus of the surface material cause different reflectivities for different materials. The reflectivity R_{refl} of a material is defined as the square of the magnitude of the Fresnel reflection coefficient. Here, the polarization of the incoming light comes into play. If the electrical field is oscillating perpendicular to the plane of incidence (s-polarization), the reflectivity is

$$R_{refl,s} = |r_s|^2 = \left| \frac{n_1 \cos\alpha - \frac{\mu_{r1}}{\mu_{r2}} n_2 \cos\beta}{n_1 \cos\alpha + \frac{\mu_{r1}}{\mu_{r2}} n_2 \cos\beta} \right|^2, \tag{2.26}$$

and if it oscillates parallel to the plane of incidence (p-polarization), it is

$$R_{refl,p} = |r_p|^2 = \left| \frac{n_2 \frac{\mu_{r1}}{\mu_{r2}} \cos\alpha - n_1 \cos\beta}{n_2 \frac{\mu_{r1}}{\mu_{r2}} \cos\alpha + n_1 \cos\beta} \right|^2 , \tag{2.27}$$

with the permeabilities μ_1 and μ_2 and the refractive indices n_1 and n_2 of material 1 and 2.
Another effect occurs if one of the material's absorption energies is met. This leads to a dramatic reduction of the reflectivity.

Distance from Source

Another important influential factor is that the photon density d_{ph} of light emitted by a point source is proportional to $1/R_1^2$, with the distance to the source R_1. This means that in any estimation of the overall efficiency of a larger RZP, different areas of the RZP receive different amounts of light and must hence be weighted with an appropriate factor. In the framework of this thesis, this method was used in combination with the efficiency calculation software Reflec as described in section 3.2 of the next chapter.

3 Design and Calculation

RZP spectrometers are wavelength-dispersive (WD). Similar to a conventional WD-spectrometer with a crystal as dispersive optical element, the incoming photons are separated spatially before entering the detector. Other than in the conventional systems (see section 4.1), the optical element is static. Instead of spreading the different photon energies angularily according to Bragg's law (see section 2.3) like the crystal, and hence being rotated during the scanning process, the RZP simultaneously focuses all photon energies of its spectral range onto a CCD.
Finding the best RZP spectrometer solution for a given scientific goal is a complicated process. The design of these spectrometers involves 4 basic steps:

- the choice of the type of RZP structure according to the main purpose of the spectrometer,
- the determination of the setup parameters depending on the one hand on the dimensions of the beamline, laboratory or scanning electron microscope within which the spectrometer is supposed to work, and on the other hand on their feasibility with today's fabrication techniques and other physical limits,
- the simulation and optimization of the efficiency, and
- the calculation of the RZP structure.

This chapter gives a detailed insight into the whole design process starting from setup dimensions and the desired function and ending with the ready-to-write RZP structure. As one of the key tasks of this thesis, a special focus is given on the development of a new calculation software.

3.1 Parameter Determination

Within the dimension limits of a laboratory, an SEM or a beamline, the key parameters of an RZP such as the arm lengths, the design energy and the angle of incidence, have to be optimized considering physical limits such as the critical angle or the fabricability of the structures. With the goals of a high resolution, low losses of photons and a sufficient fabricability, the parameter determination involves many (sometimes opposing) factors.

Generally, an approach via iteration starting with estimated values based on long-time experience has proven to be the fastest method. For this, a quantity table with all important input and output parameters has been created, with the parameters associated to each other via their mathematical connections as described in the following. The geometrical parameters are illustrated in figure 3.1 with the input shown in red and the output shown in black.

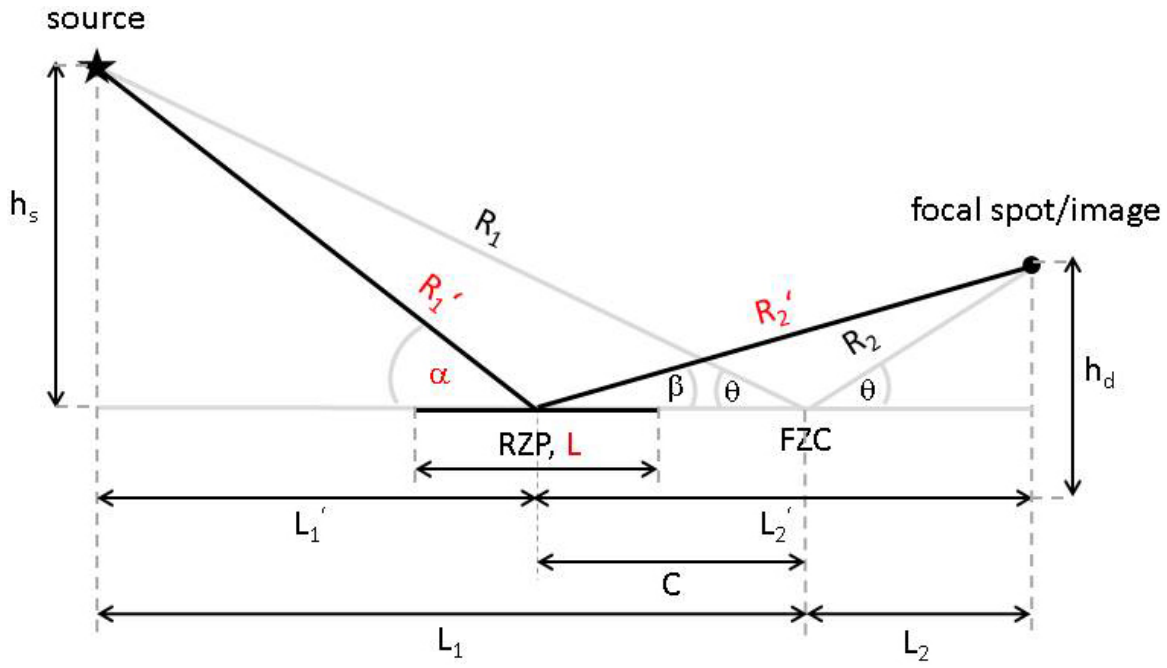

Figure 3.1: The geometry of a point-to-point reflection zone plate setup. The input parameters are labeled in red, the output parameters in black.

3.1.1 Input parameters

Photon energy

The photon energy E that the RZP will be designed for is relatively easy to determine. Depending on the purpose of the RZP spectrometer, this usually is either a specific energy corresponding to a chemical element or, as a part of quasi-continuous array of different zone plates covering a certain energy range as mentioned in section 3.8.1, one of the discrete energy steps in that range. Since the radii and widths of the Fresnel zones linearly increase with the design wavelength, lower energies cause larger zones. Or, in other words, if the photon energy is increased by a factor k, the zone sizes are decreased by k.

Angle of incidence

At a given photon energy, first of all, the angle of incidence α is limited by the condition for total external reflection. For X-rays, this leads to very small angles of only a few degrees or, for hard X-rays, even below one degree. The optimal angle of incidence (at a certain line density) depends on the reflectivity of the RZP's surface material (see figure 3.2a as an example) and the desired resolution and can be determined by simulations with simulation programs such as RAY© or REFLEC©.

Order of diffraction

The intensity of a diffraction spot varies with the diffraction order n by $\sim 1/n^2$. Therefore, in most RZP spectrometers, the RZPs are designed for either their 1^{st} or -1^{st} order. Positive order RZPs usually yield better energy resolutions, while negative order RZPs at the same setup geometry yield more photon throughput due to larger acceptance angles.

Distances to source and detector

The distance between the source and the detector plane is usually given by the setup requirements of the experiment. The position of the RZP between source and detector, determining the entrance and exit arm length R'_1 and R'_2 of the RZP, is mostly flexible within a certain range, but subject to other requirements like the desired photon throughput or magnifying/demagnifying factor. In X-ray fluorescence spectrometers for example, the fluorescent sample emits light with approximately spherical or hemispherical wave fronts, and the photon flux reaching the RZP area varies with $\sim 1/(R'_1)^2$.

Another fact to consider is the absorption of X-rays in air. Sometimes the light paths cannot be evacuated. For soft X-rays, even a cm of air causes photon losses of over 99%, mostly caused by photo absorption (see section 2.1). For hard X-rays, such as used in experiments within the framework of this thesis (see chapter 5), the attenuation is much lower. As shown in figure 3.2b for a path length of 10 cm, the change from complete absorption to almost no absorption roughly goes along with the transition between soft and hard X-rays. So in general, lower arm lengths facilitate a higher photon throughput.
On the other hand, shorter arm lengths mean a larger variation of the line density along the optical axis, resulting in smaller Fresnel zones further away from the FZC.

To maintain the desired resolution in the detector plane, shortening the exit arm will lead to smaller zones.

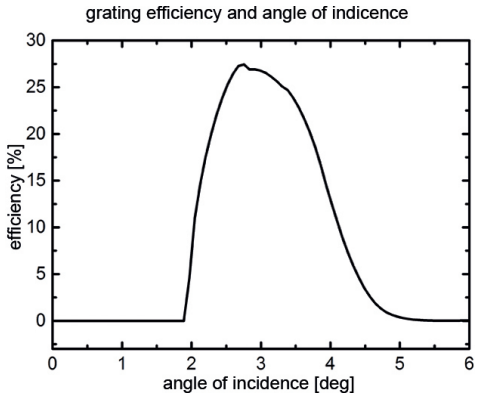

(a) Efficiency of the -1^{st} order of a laminar grating with a line density of 300 l/mm at a photon energy of 640 eV depending on the angle of incidence.

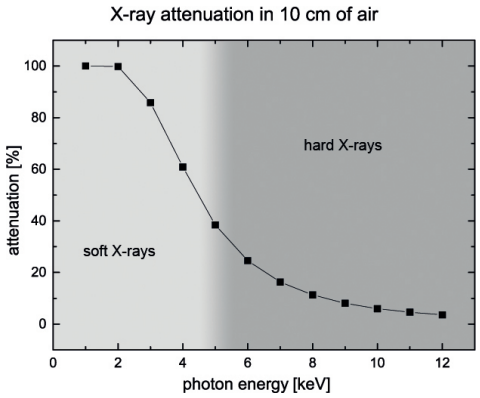

(b) Total attenuation as described in section 2.1 for X-rays between 1 and 12 keV after propagating though 10 cm of air.

Figure 3.2: a) the grating efficiency of a typical soft X-ray diffraction grating. The applicable angles of incidence are clearly limited to a range between 2° and 4°. b) Attenuation of X-rays in 10 cm of air. For lower energies below 2 keV the absorption is very high, almost 100%. At the transition to harder X-rays, the attenuation decreases to around 40% and then slowly continues droping to almost 0% for 10 keV.

Desired energy resolution and vertical focal size on the detector

Another important input quantity for the RZP parameter determination is the desired energy resolution $\lambda/\Delta\lambda = \Delta E/E$. Together with the desired vertical focal size Δh_d on the detector, it quantifies the vertical shift of the focal spot in the detector plane caused by a variation of the incoming photon energy, or in other words, the dispersive behavior of the RZP. Hence, the two quantities actually come down to a single input parameter $\Delta h_d/\Delta\lambda$, but for an easier imagination of the situation, it was split into two more illustrative quantities. In the parameter calculation, they contribute to the expression of the local grating period d (see equation 3.6) as shown in the next section.

Length of the working area

The length L of the working area of the RZP along the beam direction defines the vertical numerical aperture of the RZP and therefore influences its spatial resolution. The larger the aperture, the better the spatial resolution (see section 2.4.2). On the other hand, L also determines the vertical sizes of out-of-focus diffraction spots in the detector plane. Other energies than the design energy cause these “blurred” spots.

The larger L is, the larger the spots are vertically, and the lower the energy resolution of the RZP. Another reason for a blurred spot is a change in the entrance or exit arm length. Like with refractive lenses, this leads to another illustrative quantity, the depth of field (see end of next section).

Source size

Even though the expected source size S of an experiment does not directly influence the parameters of the RZP, it is very important during the parameter determination. Only by suggesting a realistic source of a finite size, the actual spatial resolution and the energy resolving power of the spectrometer can be calculated (see next section).

3.1.2 Output parameters

Local grating period (line density) at the center of the working area

The local grating period d or local line density $d_l = 1/d$ at the center of the working area is essential for calculations and simulations preliminary to the actual calculation of the Fresnel zone pattern such as efficiency simulations. Starting from the grating equation,

$$d\cos\alpha - \cos\beta = m\lambda, \tag{3.1}$$

which, with a fixed grating period d and incoming angle α, can be written as a function $\beta\,(\lambda)$:

$$\beta\,(\lambda) = \arccos\left(\cos\alpha - \frac{m\lambda}{d}\right), \tag{3.2}$$

its first derivative

$$\begin{aligned}\frac{d\beta}{d\lambda} &= -\frac{1}{\sqrt{1-\underbrace{(\cos\alpha - m\lambda/d\,)^2}_{=\cos^2\beta}}}\cdot\left(-\frac{m}{d}\right)\\ &= \frac{m}{d\underbrace{\sqrt{1-\cos^2\beta}}_{=\sin\beta}}\end{aligned}$$

$$\Leftrightarrow \frac{d\beta}{d\lambda} = \frac{\Delta\beta}{\Delta\lambda} = \frac{m}{d\sin\beta}, \text{ for small variations} \tag{3.3}$$

provides the angular dispersive behavior of the grating.

A change in β from β_1 to β_2 ($= \Delta\beta$) corresponds to a vertical shift from h_{d1} to h_{d2} ($= \Delta h_d$) in the detector plane by

$$\sin\beta_1 - \sin\beta_2 = \frac{h_{d1} - h_{d2}}{R_2'}.$$

With small-angle approximation this simplifies to

$$\Delta\beta = \frac{1}{R_2'} \cdot \Delta h_d. \tag{3.4}$$

Combining 3.3 with 3.4 results in

$$d = \frac{mR_2'\Delta\lambda}{\Delta h_d \sin\beta}, \tag{3.5}$$

which, with 3.2, leads to an expression for the grating period d depending only on input parameters:

$$d = \frac{\lambda|m|}{\sin\alpha}\left[-\frac{m}{|m|}\cot\alpha + \sqrt{1+\cot^2\alpha + \left(\frac{R_2'}{\Delta h_d}\frac{\Delta\lambda}{\lambda}\right)^2}\right]. \tag{3.6}$$

For the detailed equation transformation see annex (section 7.1).

Smallest zone width and total width of the RZP

With the definition of a line density vector field $\vec{d_l}\,(x,y)$ as derived in section 3.5, each local line density in an arbitrary point (x,y) in the RZP area can easily be calculated as the vector field norm. For the typical rectangular section around the axis of symmetry, no matter which diffraction order the RZP is designed for and for point-to-point RZPs, the laterally outermost region the farthest away from the FZC has the highest line density. The only exception are telescopic RZPs (see section 3.9.2). With their parabolic shape of the zones, here, the highest line density is located on the lateral outside corner as well, but the one facing the FZC. So, knowing which type of RZP is desired, for each case, the highest line density can directly be calculated by inserting the corresponding coordinates into $\vec{d_l}\,(x,y)$. Here, the total width of the RZP comes into play. It is either given in advance due to limited space on the substrate, or, as in most cases, the calculation works reversely: for a given limit of fabricable zone widths (and the resulting highest line density), the outermost lateral coordinate

x is derived from the norm of the vector field.

Angle of diffraction

For the design of any RZP spectrometer with a fixed RZP-detector system, it is very important to know the expected range of the angle of diffraction β. Mostly, with a known local line density in the center of the RZP, the grating equation (3.2) yields a sufficient estimation.

Angle of incidence at the Fresnel zone center

The incident angle θ at the FZC is one of the 6 parameters needed for the calculation of the Fresnel zone pattern as described in sections 3.6 and 3.7. From the parameters to the center of the RZP, θ can be derived via simple geometric relations:
The perpendiculars h_s and h_d of source and focal spot and the projections L_1' and L_2' of R_1' and R_2' onto the RZP plane are defined as

$$h_s = R_1' \sin\alpha \tag{3.7}$$
$$h_d = R_2' \sin\beta \tag{3.8}$$
$$L_1' = R_1' \cos\alpha \tag{3.9}$$
$$L_2' = R_2' \cos\beta. \tag{3.10}$$

At the FZC, the same applies for the incident angle *theta* and the arm lengths R_1 and R_2:

$$h_s = R_1 \sin\theta \tag{3.11}$$
$$h_d = R_2 \sin\theta \tag{3.12}$$
$$L_1 = R_1 \cos\theta \tag{3.13}$$
$$L_2 = R_2 \cos\theta \tag{3.14}$$

or, as a result,

$$\tan\theta = \frac{h_s}{L_1} = \frac{h_d}{L_2}.$$

Now, knowing that

$$L_1' + L_2' = L_1 + L_2,$$

this leads to

$$\begin{aligned} & L_1' + L_2' = \frac{1}{\tan\theta}\,(h_s + h_d) \\ \Leftrightarrow \quad & (R_1' \cos\alpha + R_2' \cos\beta) = \frac{1}{\tan\theta}\,(R_1' \sin\alpha + R_2' \sin\beta) \\ \Leftrightarrow \quad & \tan\theta = \frac{(R_1' \sin\alpha + R_2' \sin\beta)}{(R_1' \cos\alpha + R_2' \cos\beta)}, \end{aligned} \tag{3.15}$$

defined by input parameters only.

Distances between Fresnel zone center, source and detector

With a known θ, R_1 and R_2 are given by

$$R_1 = \frac{R_1' \sin\alpha}{\sin\theta} \tag{3.16}$$

and

$$R_2 = \frac{R_2' \sin\beta}{\sin\theta}, \tag{3.17}$$

resulting from 3.7, 3.8, 3.11 and 3.12.

Center and edges of working area

In the coordinate system of the full RZP with its origin in the FZC, for cutting the desired off-axis region out of the zone pattern, the center C of the RZP is given by

$$C = L_1' - L_1 = R_1' \cos\alpha - R_1 \cos\theta. \tag{3.18}$$

The edges of the working area y_1 and y_2 are determined by the length L of the RZP:

$$y_{min} = C - L/2 \tag{3.19}$$

and

$$y_{max} = C + L/2. \tag{3.20}$$

Magnification factor

The magnification factor is very important for an estimation of what focal sizes to expect with different source sizes. As described in section 2.4.2, the vertical and horizontal magnification factors differ. While in horizontal direction, the ratio between

source and focal size is given by the ratio between entrance and exit arm length (equation 2.11)

$$M_h = \frac{R'_2}{R'_1},$$

in vertical direction, the ratio is expanded by the asymmetry factor $\sin\alpha/\sin\beta$:

$$M_v = \frac{R'_2}{R'_1}\frac{\sin\alpha}{\sin\beta},$$

Real focal size

With a finite source size in both directions Δs_h and Δs_v, the realistic focal sizes Δf_h and Δf_v can be determined by 2.10 and 2.11:

$$\Delta f_h = M_h \cdot \Delta s_h \quad \text{and} \quad \Delta f_v = M_v \cdot \Delta s_v.$$

Real energy resolution

With the realistic vertical focal size Δf_v, the expected energy resolution on the detector can be derived from equations 3.5 with the focal size implemented as vertical shift $\Delta h_d = \Delta f_v$:

$$\begin{aligned} d &= \frac{mR'_2\Delta\lambda}{\Delta f_v \sin\beta} \\ \Leftrightarrow \qquad \frac{\lambda}{\Delta\lambda} &= \frac{mR'_2\lambda}{\Delta f_v d \sin\beta} \end{aligned} \tag{3.21}$$

3.2 Efficiency Simulation

An important step in the design process of RZPs is the efficiency optimization. This involves the adjustment of the variable parameters (profile depth, line density, coating material) by analyzing their exact influence on the overall efficiency of the RZP. Within this thesis, mainly the HZB's own simulation software was used for this purpose. The software Reflec© was developed by Dr. Franz Schäfers and combines complicated efficiency theories as mentioned in section 2.5 with data sets for material properties. Its actual function is, among other things, to yield the reflectivity or grating efficiency of diffraction gratings with a constant line density as a function of the incoming angle or the photon energy. The results can be graphically displayed by the program itself or extracted as ascii tables and processed further with analysis programs like OriginLab©

as shown in figure 3.3. Here, the behavior for different profile depths at a constant incident angle over a certain energy range was invesitagted. For RZPs though, this would mean just one step of a more complex analysis. Since RZPs have a varying line density, the total efficiency is a combination of a few local grating efficiencies, each for a different location within the RZP area. Hence, this analysis must be repeated with an sufficient number of points along the RZP area.

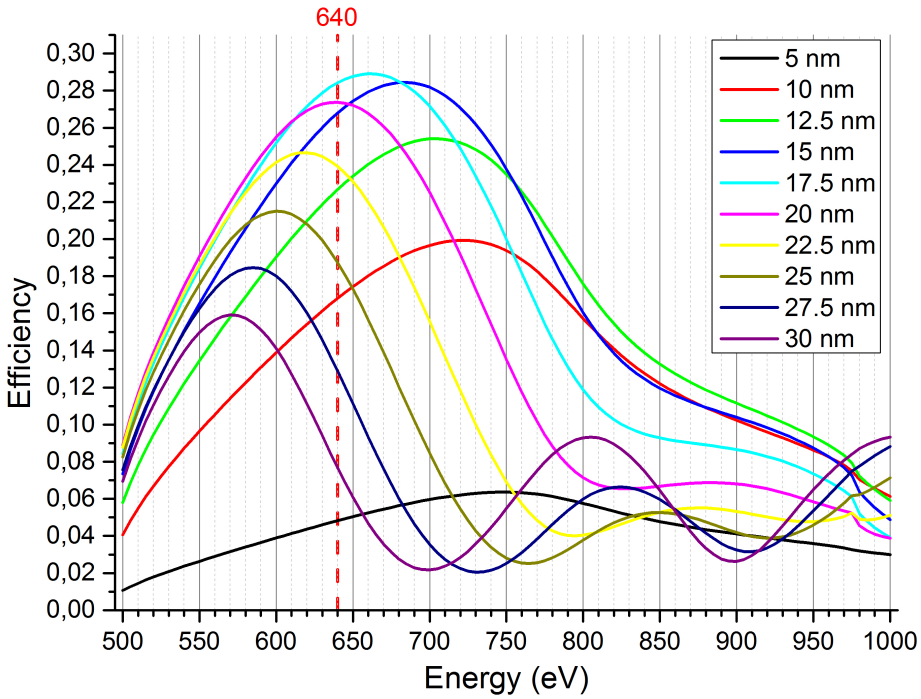

Figure 3.3: Simulated grating efficiency curves for different profile depths at constant line density (285 l/mm), depending on the photon energy.

The program is limited to an incidence perpendicular to the grating lines, though. This means that only points on the symmetry axis of the RZP can be simulated here. At the laterally outer parts of an RZP, perpendicular incidence does not meet the reality. With the support of another simulation software, a freeware called GSolver©, which has indeed a feature for a lateral angle of incidence, this problem could be solved. The simulation results connected with the behavior in outer parts of an RZP will be analyzed in detail in section **??**.

3.3 Simulation of Diffraction Image

Another powerful tool to simulate the properties of RZPs is the ray tracing program RAY©, which was also developed by Dr. Franz Schäfers at the Helmholtz-Zentrum Berlin, actually for simulating whole beamlines. The user can trace a light beam through a desired number of optical components like mirrors, crystals, gratings, etc. For the simulation of RZPs, RAY© uses a grating overlay technique, shown as a scheme in figure 3.4. The line density in each point of the RZP is parted into two vector coordinates, perpendicular to the incoming light, and parallel to it. An incoming light ray (provided with a random direction within a certain divergence of the source) is then deflected in both directions according to the laws of diffraction. The results of the ray tracing method are so called footprints, point diagrams of the light rays hitting a plane of interest. These footprints can be extracted for the source, the RZP plane itself, and an image plane at a desired distance to the RZP. A typical footprint in the image plane is shown in figure 3.5. Recently, a graphical user interface and the possibility of adding the specular reflection (zeroth order) to the image plane footprint were implemented, making the program a very versatile and useful tool within this thesis.

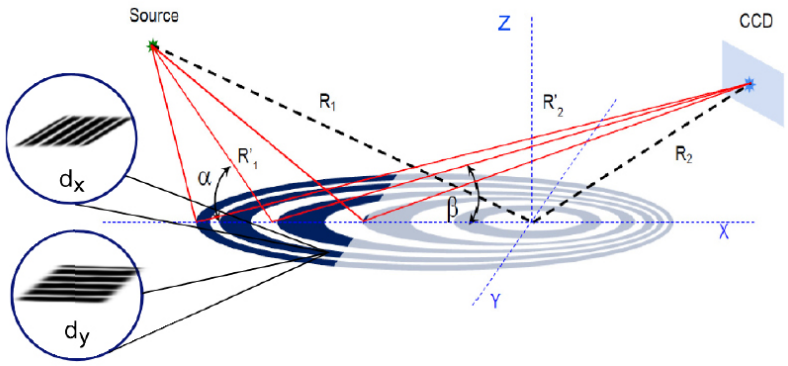

Figure 3.4: Technique for the calculation of RZP diffraction images of the simulation software RAY©. At each point on the RZP surface, two perpendicular gratings with a certain line density are superimposed.

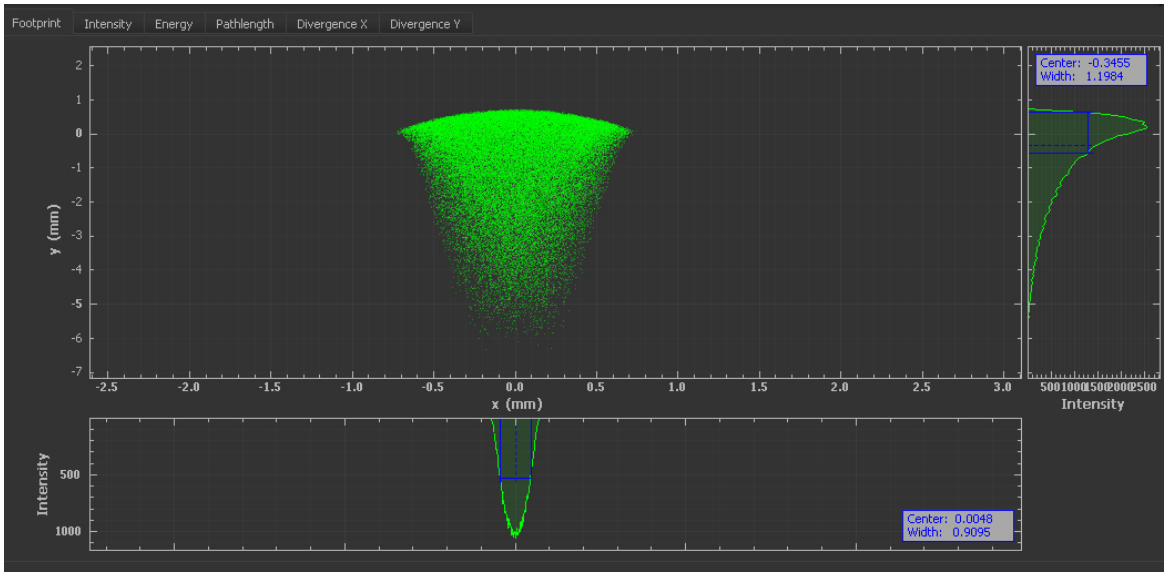

Figure 3.5: Typical footprint in the image plane of an RZP. The central point diagram features the distribution of light rays hitting the plane, and the line spectra below and on the right show the intensity distributions along the vertical and horizontal axis.

3.4 Phase Law of Zone Pattern and RZP Coordinate System

As mentioned above, the edges of the Fresnel zones in RZPs have an elliptical shape. To determine their exact shape and location for the structure visualization and realization, a two-dimensional Cartesian coordinate system is useful. It stands to reason to define the RZP plane itself as x-y-plane with the Fresnel zone center in the origin of the coordinate system. This can be embedded into a three-dimensional coordinate system with the optical axis of the RZP in the x-z-plane (see figure 3.6). The light source point A then has the coordinates (R_{1x}, R_{1y}, R_{1z}) and the detector point B is located at (R_{2x}, R_{2y}, R_{2z}). Any arbitrary point $P(x, y, 0)$ in the RZP plane defines a path difference Δp between two light paths from A to B: along the optical axis (blue) and via P (red), with $\overline{AP} = \vec{R_1'}$ and $\overline{PB} = \vec{R_2'}$:

$$\Delta p = |\vec{R_1'}| + |\vec{R_2'}| - \left(|\vec{R_1}| + |\vec{R_2}|\right). \tag{3.22}$$

Multiplied by π/λ this transfers into the corresponding phase shift Φ:

$$\Phi(x, y) = \frac{\pi}{\lambda}\left(|\vec{R_1'}| + |\vec{R_2'}| - \left(|\vec{R_1}| + |\vec{R_2}|\right)\right). \tag{3.23}$$

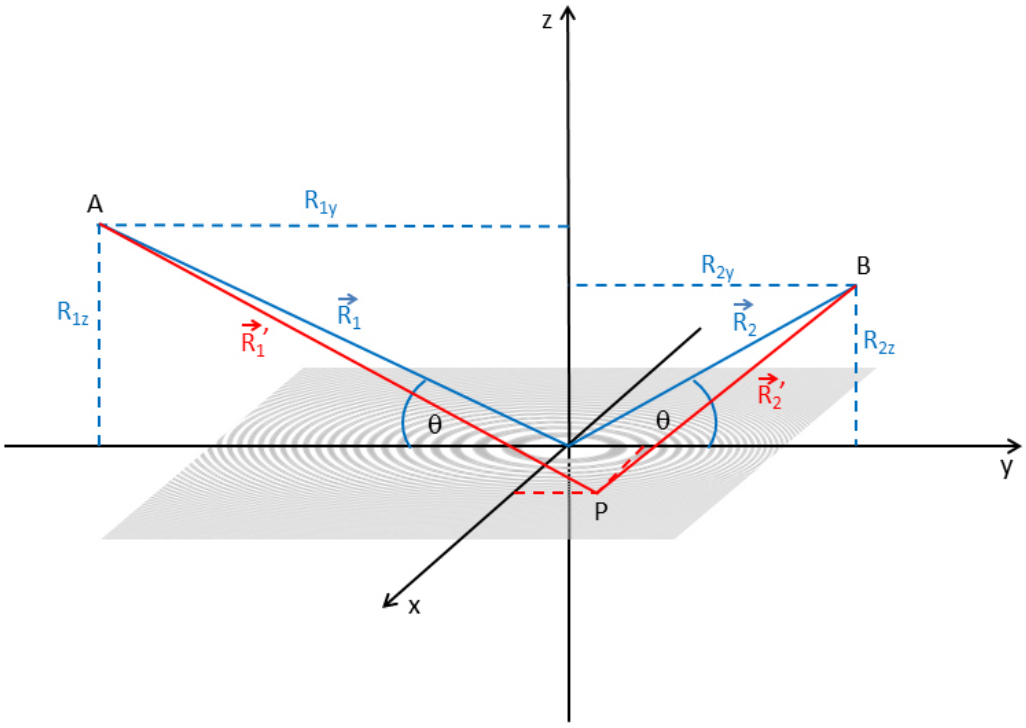

Figure 3.6: Point-to-point RZP zone structure geometry in a Cartesian coordinate system. The RZP plane is defined as x-y-plane and the optical path through the Fresnel zone center runs along the y-z-plane. The source is located in point A at a height of $h_s = R_{1z}$ above the RZP-plane, the detector point at a height of $h_d = R_{2z}$. The optical axis through the FZC is depicted in blue ($\vec{R_1} + \vec{R_2}$). The Cartesian coordinates x amd y of any point P on the RZP plane can be expressed by the RZP input parameters R_1, R_2, θ and λ. The phase shift between the two light paths along the optical axis and via P (depicted in red), is given by a function $\phi(x, y)$.

Geometrical conditions define the coordinates of $\vec{R_1}$ and $\vec{R_2}$ as

$$R_{1x} = 0, \tag{3.24}$$

$$R_{1y} = R_1 \cos\theta, \tag{3.25}$$

$$R_{1z} = R_1 \sin\theta, \tag{3.26}$$

$$R_{2x} = 0, \tag{3.27}$$

$$R_{2y} = R_2 \sin\theta \quad \text{and} \tag{3.28}$$

$$R_{2z} = R_2 \sin\theta, \tag{3.29}$$

with $|\vec{R_1}| = R_1$ and $|\vec{R_2}| = R_2$. The absolute values of the two parts of the red path $|\vec{R_1'}|$ and $|\vec{R_2'}|$ are then given by the Pythagorean conditions

$$|\vec{R_1'}| = \sqrt{(R_{1x} - x)^2 + (R_{1y} - y)^2 + (R_{1z} - 0)^2} = \sqrt{x^2 + (R_1\cos\theta - y)^2 + (R_1\sin\theta)^2} \tag{3.30}$$

and

$$|\vec{R_2'}| = \sqrt{(R_{2x} - x)^2 + (R_{2y} - y)^2 + (R_{2z} - 0)^2} = \sqrt{x^2 + (R_2 \cos\theta - y)^2 + (R_2 \sin\theta)^2}. \tag{3.31}$$

Implementing this into 3.23 results in

$$\Phi(x,y) = \frac{\pi}{\lambda}\left(\sqrt{x^2 + (R_1\cos\theta - y)^2 + (R_1\sin\theta)^2} + \sqrt{x^2 + (R_2\cos\theta - y)^2 + (R_2\sin\theta)^2} - (R_1 + R_2)\right), \tag{3.32}$$

the phase shift as a function of x and y depending only on the input parameters R_1, R_2, θ and λ. For the Fresnel zone edges, the phase shift to the optical axis must be an integer factor n multiplied by $\pi/2$, resulting in a path difference of $\Delta p = n\lambda/2$ and the equation

$$\sqrt{x^2 + (R_1\cos\theta - y)^2 + (R_1\sin\theta)^2} + \sqrt{x^2 + (R_2\cos\theta - y)^2 + (R_2\sin\theta)^2} - (R_1 + R_2) - n \cdot \frac{\lambda}{2} = 0, \tag{3.33}$$

which can be transferred (see annex, 7.2) into a clearer expression of the form

$$K_1 y^2 + K_2 y + K_3 x^2 + K_4 = 0. \tag{3.34}$$

With a simple transformation

$$\begin{aligned}
& K_1 y^2 + K_2 y + K_3 x^2 + K_4 && = 0 \\
\Leftrightarrow\quad & \tfrac{y^2}{K_3} + \tfrac{K_2}{K_1 K_3} y + \tfrac{x^2}{K_1} + \tfrac{K_4}{K_1 K_3} && = 0 \\
\Leftrightarrow\quad & \tfrac{(y+\frac{K_2}{K_1})^2 - (\frac{K_2}{K_1})^2}{K_3} + \tfrac{x^2}{K_1} + \tfrac{K_4}{K_1 K_3} && = 0 \\
\Leftrightarrow\quad & \tfrac{(y+\frac{K_2}{K_1})^2}{K_3} + \tfrac{x^2}{K_1} && = \frac{K_2^2}{K_1^2 K_3} - \frac{K_4}{K_1 K_3} = const,
\end{aligned} \tag{3.35}$$

it becomes clear that this is the equation of an ellipsis. The center of the ellipsis M has the coordinates $(0, -\frac{K_2}{K_1})$, which means that the ellipsis is symmetrical to the y-axis, but not to the x-axis. Each zone edge center is shifted along the y-axis depending on the zone edge number n. 3.35 can be transformed into surjective functions $x(y)$ and $y(x)$ with two solutions each.

3.5 Line Density Vector Field

The gradient of the scalar field 3.32 describing the phase shift between the path along the optical axis and the path via an arbitrary point $P(x, y)$ on the RZP,

$$\vec{\nabla}\Phi(x,y) = \frac{\partial\Phi}{\partial x}\vec{e_x} + \frac{\partial\Phi}{\partial y}\vec{e_y} \tag{3.36}$$

yields the local line density vector $\vec{d_l}$ in P:

$$\vec{d_l} = \vec{\nabla}\Phi(x,y) = \frac{\pi}{\lambda}\left(\frac{x}{\sqrt{C_1}} + \frac{x}{\sqrt{C_2}} - \frac{R_1\cos\theta - y}{\sqrt{C_1}} - \frac{R_2\cos\theta - y}{\sqrt{C_2}}\right), \tag{3.37}$$

with

$$C_1 = x^2 + (R_1\cos\theta - y)^2 + (R_1\sin\theta)^2$$

and

$$C_2 = x^2 + (R_2\cos\theta - y)^2 + (R_2\sin\theta)^2.$$

As shown in figure 3.7, the local line density vector points perpendicular to the Fresnel zones. The absolute value of the line density on an RZP generally varies between $|\vec{d_{l,min}}| = 0$ at the FZC and a limit value of $|\vec{d_{l,max}}| = 2/\lambda$. The line density is the reciprocal value of the local grating period d

$$d = \frac{1}{|\vec{d_l}|}, \tag{3.38}$$

meaning that the maximum line density correlates with the smallest possible period $d_{min} = \lambda/2$ or the smallest possible zone width $fz_{min} = d_{min}/2 = \lambda/4$, respectively.

3.6 Structure Calculation - State of the Art

For the realization of an RZP, the Fresnel zone structure must be calculated in a data format compatible with an e-beam or laser writing machine. These machines work with a set of two dimensional (x,y)-coordinate points at which the beam exposes the writing material with a certain dose. The internal software of the machines will generate these exposure points itself for any given structure composed of closed polygons. Thus, a writable Fresnel zone structure has to be calculated as such.
For any data calculation of Fresnel zones as closed polygons, mathematical functions

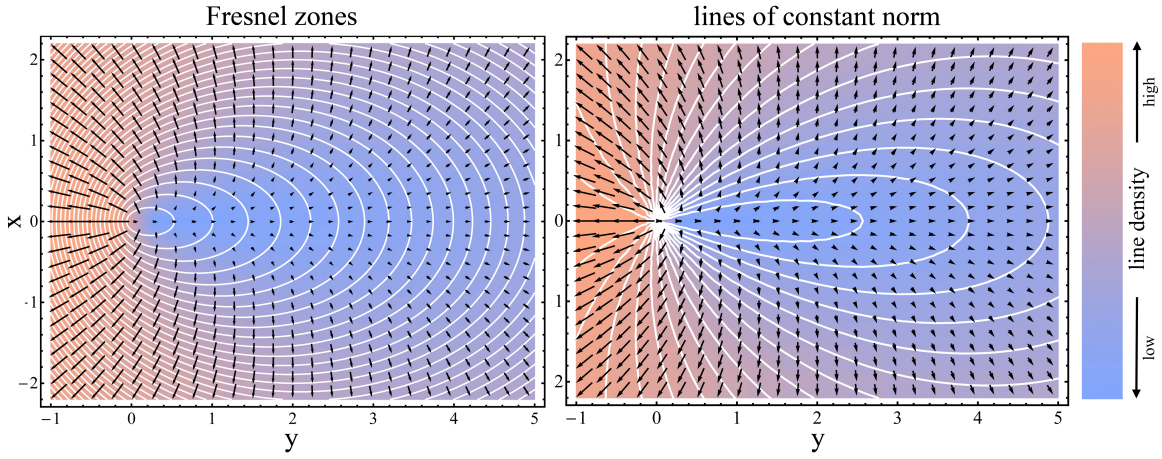

Figure 3.7: Schematic line density vector field for a point-to-point RZP with Fresnel zones (left graph) and drop-shaped curves of constant line density (right).

that follow the shape of the zone edges are needed. In the framework of the Diploma thesis [14] preceding this work, a basic calculation software for rectangular off-axis sections of RZPs was developed. The equation for the elliptical Fresnel zone edges (3.35) of a point-to-point RZP was used to derive surjective functions in the (x,y)-coordinate system. The two versions $x_{1,2}(y)$ and $y_{1,2}(x)$ are equivalently adaptable. To avoid inaccuracies at the edges of the structure though, both functions were incorporated into the calculation algorithm. The rectangular working area A of the RZP is defined by a given width B, as well as the edges y_1 and y_2 as found in the parameter determination above (section 3.1.2).

The basic principle of the algorithm is illustrated in figure 3.8: for a set of equidistant x-values from $-B/2$ to $B/2$, the corresponding y-values are determined with $y(x)$. Which one of the two possible solutions $y_{1,2}(x)$ the program must use is determined by the algorithmic sign of y_1 and y_2, or in other words, the diffraction order (for negative orders, the convex part and for positive orders the concave part of the ellipsis is used, figure 3.8 shows the $+1^{st}$ order). Every Fresnel zone contains two zone edges numbered with an index n. The Fresnel zones themselves are numbered with another index t. In an inner loop, the lower zone edge curve is calculated from left to right. Then, n is increased by 1, jumping to the next higher zone edge, and the upper edge is calculated backwards. The polygon

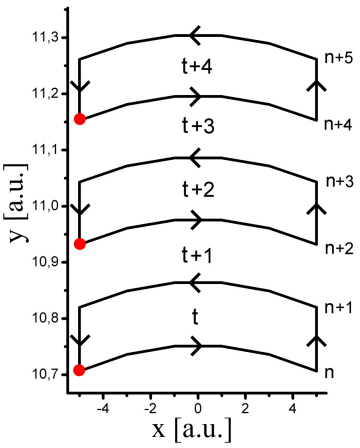

Figure 3.8: Calculation algorithm of zones as closed polygons.

is closed by copying the first value into the last entry in the data point set. In an outer loop, the zone number t is then increased by 2, obeying the condition for positive interference at alternatingly written and not written zones.

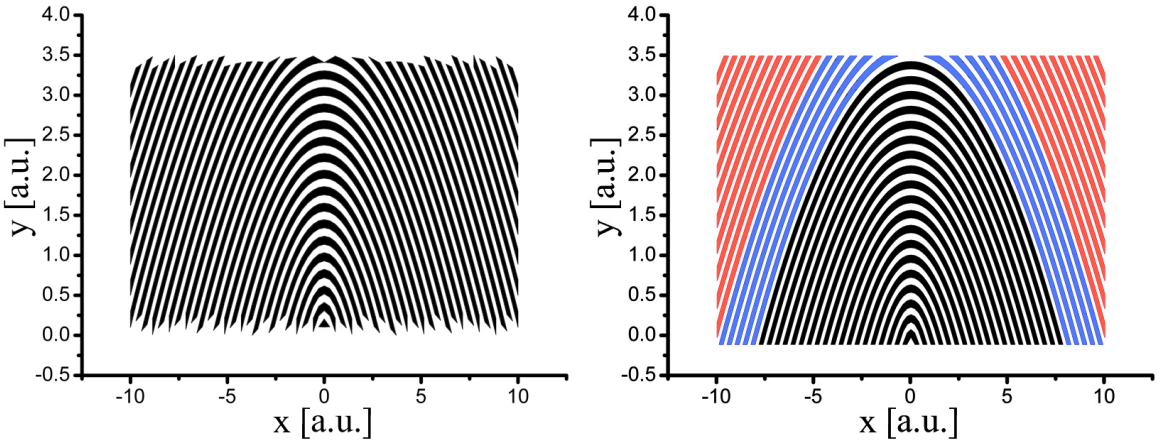

(a) Low resolution problem on edges

(b) Different types of zones

Figure 3.9: a) Schematic illustration of an RZP calculated via only one surjective function $y_{1,2}(x)$. At the upper and lower edges of the working area the finite number of equidistant given x-coordinates causes undesirable "spikes". b) The same zone structure with straight edges (inverse function $x(y)$ used as well) and differently colored zone types: uninterrupted and not crossing the lateral edges of the working area (black), parted and not crossing the lateral edges (blue), parted and crossing the lateral edges (red).

The algorithm becomes more complicated, if the zone does not exceed the lateral edges of the working area or if the upper edge at y_2 cuts off an inner part of the zone. In the first case, the first x-value of the calculation loop corresponds to a y-value larger than y_1. Especially for zones with a strong slope like in the outer regions of the RZP, this will result in a poor structure quality (see figure 3.9a). Here, the first and last (x, y)-pairs of each zone edge must be determined with $x(y)$. Figure 3.9b shows types of zones that differ from the common ones: those that start at a given y-value but still can be written in an uninterrupted loop (black), those that are written in two parts and start at a given y-value (blue) and those that are parted and start at a lateral edge (red). For all these types, the calculation algorithm is a little different, making the program complicated. Additionally, the functions $y(x)$ and $x(y)$ include many mathematical operations, slowing down the total calculation time for an RZP. Actually, in general, the intersection between an ellipsoid and a plane in a 3D space does not seem to be an easy-to-solve mathematical problem, since only recently, in 2012, a very helpful paper was published on this matter [15], laying the foundation for an advanced version of the RZP calculation program, as described in the next section.

3.7 Development of Advanced Software

To avoid large data volumes and complicated nested subroutines and to reduce the calculation time in general, a new RZP calculation program was developed in the framework of this thesis. On the basis of a mathematical paper describing a simple and fast determination of an ellipse as intersection between an ellipsoid and a plane in a 3D space, the new algorithm reproduces the actual physical principle of origin of the Fresnel zones. Now, the Fresnel zone edges on the RZP do not have to be described by surjective functions anymore and more versatile shapes of the RZP aperture are easily applied. The derivation of the calculation process from the ellipsoid/plane intersection and the RZP geometry will be described in the following.

3.7.1 Ellipsoid and Plane Intersection

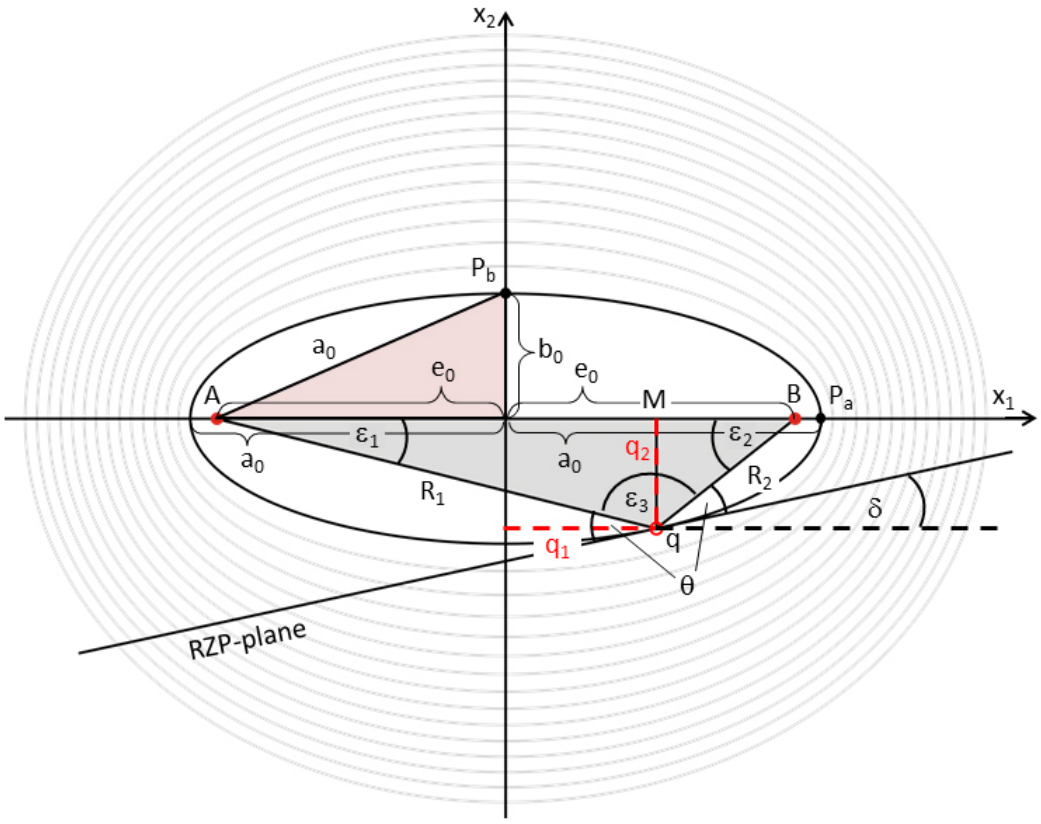

Figure 3.10: Geometry of the Fresnel zone ellipsoids and RZP-plane intersection

In the paper mentioned above with the title "On the Ellipsoid and Plane Intersection Equation" [15] published in the Journal of Applied Mathematics in 2012, the explicit

goal of the author was to find "simple formulas for the semi-axes and the center of the ellipse" as an intersection line between a 3D ellipsoid and a plane (see figure 3.10 for illustration). For the purpose of a fast and versatile RZP calculation, the basic part of the paper's derivations, described in the following, was used in the new program.

Starting with an ellipsoid around the two foci A and B with the semi-axes a,b and c in a 3D Cartesian coordinate system with the axes x_1, x_2 and x_3,

$$\frac{x_1^2}{a^2} + \frac{x_2^2}{b^2} + \frac{x_3^2}{c^2} = 1, \tag{3.39}$$

and a plane with the orthogonal spanning unit vectors $\vec{r}$ and $\vec{s}$ with

$$\vec{r} = \begin{pmatrix} r_1 \\ r_2 \\ r_3 \end{pmatrix} \quad \text{and} \quad \vec{s} = \begin{pmatrix} s_1 \\ s_2 \\ s_3 \end{pmatrix},$$

an intersection point q contained in both the plane and the ellipsoid volume is defined with the position vector

$$\vec{q} = \begin{pmatrix} q_1 \\ q_2 \\ q_3 \end{pmatrix}.$$

With the diagonal matrix

$$D = diag\left(\frac{1}{a}, \frac{1}{b}, \frac{1}{c}\right) = \begin{pmatrix} \frac{1}{a} & 0 & 0 \\ 0 & \frac{1}{b} & 0 \\ 0 & 0 & \frac{1}{c} \end{pmatrix},$$

the coordinates of the central point (u_0, v_0) and the semi-axes A and B of the intersection ellipse are then given as

$$u_0 = \frac{D\vec{q}, D\vec{r}}{D\vec{r}, D\vec{r}} \quad \text{and} \quad v_0 = \frac{D\vec{q}, D\vec{s}}{D\vec{s}, D\vec{s}} \tag{3.40}$$

and

$$A = \sqrt{\frac{1 - K_d}{D\vec{r}, D\vec{r}}} \quad \text{and} \quad B = \sqrt{\frac{1 - K_d}{D\vec{s}, D\vec{s}}}, \tag{3.41}$$

where

$$K_d = (D\vec{q}, D\vec{q}) - \frac{(D\vec{q}, D\vec{r})^2}{(D\vec{r}, D\vec{r})} - \frac{(D\vec{q}, D\vec{s})^2}{(D\vec{s}, D\vec{s})}.$$

So, the only input parameters here are the ellipsoid's semi-axes and the plane parameters. All conditions hold if the point q is just the contact point between the ellipsoid and the plane as shown in figure 3.10. If this is applied to the geometry of an RZP as the tangential plane of an ellipsoid with the semi-axes a_0, b_0 and c_0 and the source and detector point in the ellipsoid's foci, this point of contact q becomes the center of the Fresnel zones (FZC). The distance between focus A and q is now the entrance arm length of the RZP, R_1, and the distance between focus B and q is the exit arm length R_2. The incident angle θ of the RZP defines the obtuse angle of the gray triangle as $\gamma = 2\pi - 2\theta$.
Now, additional conditions specify the problem and yield the characteristic ellipsoid and plane parameters depending only on the input parameters (R_1, R_2, and θ) of the RZP:

1. **Lateral symmetry:** the lateral semi-axes b_0 and c_0 have the same length (therefore only two dimensions are shown in figure 3.10):

$$b_0 = c_0. \tag{3.42}$$

2. **Length of eccentricity:** the eccentricity e_0 (distance between a focal point and the center of the ellipsoid) is not a parameter needed for 3.40 or 3.41 itself, but it is vital in the calculation of many other parameters. It can be derived from the law of cosines for the gray triangle $\Delta(ABq)$:

$$(2e_0)^2 = R_1^2 + R_2^2 - 2R_1R_2\cos\epsilon_3,$$

where the obtuse angle ϵ_3 is given as $\epsilon_3 = \pi - 2\theta$. With $\cos\epsilon_3 = -\cos\pi - \epsilon_3 = -\cos 2\theta$ this yields

$$(2e_0)^2 = R_1^2 + R_2^2 + 2R_1R_2\cos 2\theta. \tag{3.43}$$

3. **Length of longitudinal semi-axis:** imagine the sum S of distances from point P_a (on the far right of the ellipsoid) to the two foci. According to the ellipsis condition, it must be the same as for point q with $S = R_1 + R_2$. From the figure it is clear, that the sum of distances for P_a is also $e_0 + a_0 + (a_0 - e_0) = 2a_0$, so

$$2a_0 = R_1 + R_2. \tag{3.44}$$

4. **Length of lateral semi-axes:** via the Pythagorean theorem in the light red triangle between A, P_b and the coordinate origin $(0,0)$ as well as equation 3.43, the lateral semi-axes of the ellipsoid is given as

$$b_0 = \sqrt{a_0^2 - e_0^2} = \sqrt{a_0^2 - (R_1^2 + R_2^2 + 2R_1R_2\cos 2\theta)^2}. \tag{3.45}$$

The fact that the hypothenuse must have the length a_0 comes from the sum of distances S of an arbitrary point of the ellipsoid to the two foci again: imagine this point in P_b. The segment $\overline{AP_b}$ is then exactly half of $S = 2a_0$ (3.44).

5. **Coordinates of q:** the intersection line between the ellipsoid and the plane of the optical path (x_1, x_2-plane) is an ellipsis with the semi-axes a_0 and b_0 as shown in figure 3.10. Its ellipsis equation is 3.39, reduced by the x_3-dimension:

$$\frac{x_1^2}{a_0^2} + \frac{x_2^2}{b_0^2} = 1. \tag{3.46}$$

The Pythagorean theorem in the triangle $\Delta(AMq)$ gives a condition for the coordinates of q:

$$\begin{aligned} R_1^2 &= (e_0 + q_1)^2 + q_2^2 \\ \Leftrightarrow \quad q_2^2 &= R_1^2 - (e_0 + q_1)^2. \end{aligned} \tag{3.47}$$

Inserting 3.47 into 3.46 gives

$$\begin{aligned} & \tfrac{q_1^2}{a_0^2} + \tfrac{R_1^2 - (e_0+q_1)^2}{b_0^2} && = 1 \\ \Leftrightarrow \quad & b_0^2 q_1^2 + a_0^2 R_1^2 - a_0^2 (e_0 + q_1)^2 && = a_0^2 b_0^2 \\ \Leftrightarrow \quad & b_0^2 q_1^2 - a_0^2 q_1^2 - 2a_0^2 e_0 q_1 && = a_0^2 b_0^2 - a_0^2 R_1^2 + a_0^2 e_0^2 \\ \Leftrightarrow \quad & \underbrace{(b_0^2 - a_0^2)}_{=-e_0^2} q_1^2 - 2a_0^2 e_0 q_1 && = a_0^2 (e_0^2 + b_0^2 - R_1^2) \\ \Leftrightarrow \quad & q_1^2 + \tfrac{2a_0^2}{e_0} q_1 + \tfrac{a_0^2 (a_0^2 - R_1^2)}{e_0^2} && = 0. \end{aligned}$$

The two solutions then are

$$\begin{aligned}(q_1)_{1,2} &= -\tfrac{a_0^2}{e_0} \pm \sqrt{\tfrac{a_0^4}{e_0^2} - \tfrac{a_0^2(a_0^2-R_1^2)}{e_0^2}} \\ &= -\tfrac{a_0^2}{e_0} \pm \tfrac{\sqrt{a_0^4-a_0^4+a_0^2R_1^2}}{e_0} \\ &= -\tfrac{a_0^2}{e_0} \pm \tfrac{a_0R_1}{e_0}.\end{aligned}$$

With the condition that q_1 must not exceed the ellipse's limits $-a_0$ or $+a_0$,

$$\begin{aligned}&-a_0 \leq q_1 \leq a_0, \\ \Leftrightarrow &-1 \leq -\frac{a_0}{e_0} \pm \frac{R_1}{e_0} \leq 1 \\ \Leftrightarrow &-e_0 \leq -a_0 \pm R_1 \leq e_0 \\ \Leftrightarrow &e_0 \geq a_0 \mp R_1 \geq -e_0,\end{aligned}$$

and the fact that $e_0 \leq a_0$, it is clear that only the second solution where $e_0 \geq a_0 - R_1$ makes sense. Thus, the first coordinate of q is

$$q_1 = -\frac{a_0^2}{e_0} + \frac{a_0R_1}{e_0}.$$

The second coordinate, q_2, is easily obtained from 3.47:

$$q_2 = \sqrt{R_1^2 - (e_0+q_1)^2}.$$

The third coordinate is zero, since q lies in the x_1, x_2-plane. Consequently, q is given as

$$\vec{q} = \begin{pmatrix} -\frac{a_0^2}{e_0} + \frac{a_0R_1}{e_0} \\ \sqrt{R_1^2 - (e_0+q_1)^2} \\ 0 \end{pmatrix}. \tag{3.48}$$

6. **Spanning vectors $\vec{r}$ and $\vec{s}$:** the spanning vectors must be orthogonal to the plane's normal vector and to each other. The first one can be chosen as parallel to the x_3-axis:

$$\vec{r} = \begin{pmatrix} 0 \\ 0 \\ 1 \end{pmatrix}. \tag{3.49}$$

The second one then must lie in the x_1, x_2-plane. The plane crosses the x_1-axis

at the angle δ. A unit vector in this direction is given as

$$\vec{s} = \begin{pmatrix} \cos\delta \\ -\sin\delta \\ 0 \end{pmatrix}.$$

The angle δ can be derived from known parameters as follows: In the triangle $\Delta(MBq)$, the sum of angles must be π, so the angle at point q must be $\pi - \frac{\pi}{2} - \epsilon_2$. From the right angle between the black dashed reference line parallel to the x_1-axis, δ can then be derived as

$$\delta = \frac{\pi}{2} - \theta - \left(\frac{\pi}{2} - \epsilon_2\right) = \epsilon_2 - \theta.$$

With the trigonometric condition

$$\sin\epsilon_2 = \frac{q_2}{R_2},$$

this results in

$$\delta = \arcsin\frac{q_2}{R_2} - \theta. \tag{3.50}$$

Hence, the second spanning vector is

$$\vec{s} = \begin{pmatrix} \cos\left(\arcsin\frac{q_2}{R_2} - \theta\right) \\ -\sin\left(\arcsin\frac{q_2}{R_2} - \theta\right) \\ 0 \end{pmatrix}. \tag{3.51}$$

Finally, all parameters needed for the calculation of the Fresnel zones in the RZP-plane as intersection ellipsoids via 3.40 and 3.41 are determined. How these determinations are embedded in the algorithm of the new software will be explained in the next section.

3.7.2 Calculation Algorithm

One of the time-saving advantages of the new program is that all the basic information about the RZP geometry is given by the parameter determination described in the previous section, independent of the actual calculation of the Fresnel zones. In other words, only once at the beginning of the calculation algorithm, these parameters (the semi-axes of the first ellipsoid touching the plane in the osculation point q, the

coordinates of q and the spanning vectors $\vec{r}$ and $\vec{s}$ of the plane) are calculated and then remain fixed during the production of the RZP data.

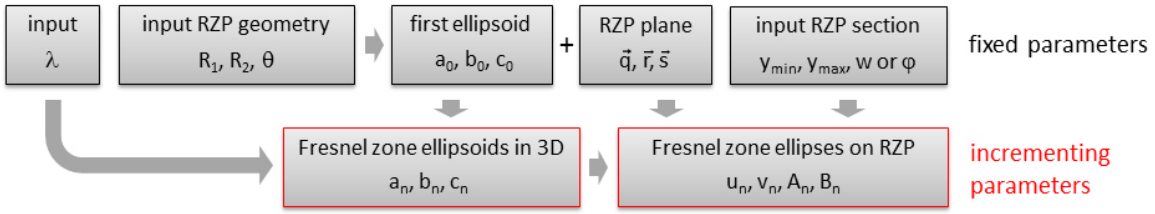

Figure 3.11: Scheme of the calculation algorithm for the determination of the Fresnel zone edges on the RZP plane. The first row shows the parameters that remain fixed during the RZP data production and the second row shows the incrementing parameters of different Fresnel zones.

Figure 3.11 shows a scheme of the calculation process. The input parameters are implemented in two packages, the basic RZP parameters (R_1, R_2 and θ), that determine the shape of the Fresnel zones, and the section parameters that define the section of the RZP used in the fabrication as well as the single input parameter λ, the wavelength corresponding to the design energy of the RZP. The section parameters are the off-axis limits in beam direction y_{min} and y_{max} and another parameter that gives the shape and location of the lateral limits. This can either be just the width w of the RZP or the opening angle ϕ of an RZP trapeze as shown in figure 3.13. With the first package of input values, the parameters of the first ellipsoid (semi-axes a_0, b_0 and c_0) and the RZP plane vectors ($\vec{q}$, $\vec{r}$ and $\vec{s}$) are calculated. On the basis of the first ellipsoid's parameters, the parameters of all subsequent Fresnel zone ellipsoids are determined. This determination is based on the phase shift law of Fresnel zones 3.33:

$$R_1' + R_2' = R_1 + R_2 + n\frac{\lambda}{2}. \tag{3.52}$$

With 3.44, the ellipsoid matching the path difference $n\frac{\lambda}{2}$ is given by its semi-axes

$$a_n = a_0 + n\frac{\lambda}{4} \tag{3.53}$$

and

$$b_n = c_n = \sqrt{a_n - e_0}. \tag{3.54}$$

The eccentricity e_0 remains the same for all Fresnel zone ellipsoids, as the distance between the two foci does not change.
The actual Fresnel zone edge ellipses on the RZP plane are then given as intersections with the incrementing ellipsoids, with the coordinates of the central point u_n and v_n

and their semi-axes A_n and B_n calculated via 3.40 and 3.41, inserting the different ellipsoid semi-axes for each integer n into the diagonal matrix

$$D_n = diag\left(\frac{1}{a_n}, \frac{1}{b_n}, \frac{1}{c_n}\right):$$

$$u_n = \frac{D_n\vec{q}, D_n\vec{r}}{D_n\vec{r}, D_n\vec{r}} = 0 \quad \text{and} \quad v_n = \frac{D_n\vec{q}, D_n\vec{s}}{D_n\vec{s}, D_n\vec{s}} \tag{3.55}$$

and

$$A_n = \sqrt{\frac{1 - K_d}{D_n\vec{r}, D_n\vec{r}}} \quad \text{and} \quad B_n = \sqrt{\frac{1 - K_d}{D_n\vec{s}, D_n\vec{s}}}. \tag{3.56}$$

with

$$K_d = (D_n\vec{q}, D_n\vec{q}) - \frac{(D_n\vec{q}, D_n\vec{r})^2}{(D_n\vec{r}, D_n\vec{r})} - \frac{(D_n\vec{q}, D_n\vec{s})^2}{(D_n\vec{s}, D_n\vec{s})}.$$

The increment n is the number of the zone edges intersecting with the RZP plane. It starts at $n = 0$ for the FZC in point q. Note that the actual path difference between light traveling in a direct line from A to B and the path via q is independent of this and is not considered in the calculations. The Fresnel condition only has to be fulfilled for the relative phase shifts within a diffracting optical element such as an RZP. Like the 3D ellipsoids, all intersection ellipses are symmetrical to the x_1-axis, meaning that the second coordinate v_n of the central point remains zero. The second input package with the section parameters defines the region in which the actual zone plate data as set of polygons is calculated as described in the next section.

3.7.3 RZP Coordinates, Angular Distribution Law and Aperture Shape

Any writing machine usable for RZP structures works with a set of tuples that compose closed polygons. As implemented in the preliminary version of the RZP program (see section 3.6), an (x, y)-coordinate system with the projection of the optical axis running along the y-axis is the most simple and intuitive solution. To transform the given Fresnel zone edge ellipses into polygons, the most convenient way is a parametric vector function

$$\vec{f_n} = \begin{pmatrix} x \\ y \end{pmatrix} = \begin{pmatrix} A_n \cos t \\ B_n \sin t + v_n \end{pmatrix}, \qquad (3.57)$$

that describes the ellipsis in polar coordinates with the angular parameter $0 \leq t \leq 2\pi$. As mentioned above, the central point of each ellipse is shifted along the y-axis only, which simplifies the problem even further. If t increases in equidistant steps, for a very narrow zone shape, where $B_n \ll A_n$, the strongly curved sections of the ellipsis around $t = \pi/2$ or $t = 3\pi/2$ have a lower quality than the less curved sections (see figure 3.12). To adapt the point density to the curvature of the ellipsis in a sensible way, the angular distribution law

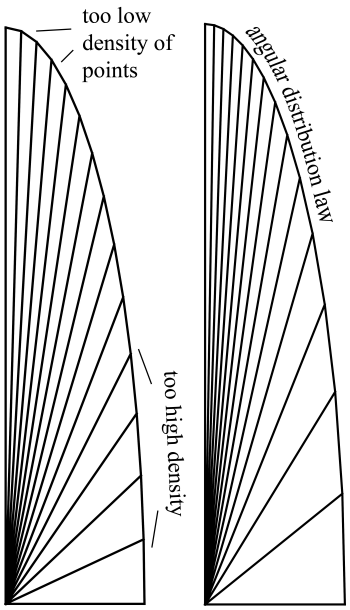

Figure 3.12: Zone edge calculation with polar coordinates at equidistant angles (left) and with the angular distribution law (right).

$$t = \arctan\left(\tan\varphi \left(\frac{B_n}{A_n}\right)^j\right) \qquad (3.58)$$

was used, with the inner variable φ now increasing in equidistant steps. The exponent was found to yield the smoothest curves at $j = 0.382$, equal to one of line segments in the golden ratio. This also minimizes the number of points needed for each polygon and saves data volume as well as calculation time. Another feature of the new program that reduces the calculation time even more dramatically, is the use of the symmetry. Only one side of the whole RZP is actually calculated with the parametric ellipsis function. The other half is then produced by copying and mirroring the first half. In the mirroring step, only the algebraic sign of first coordinate of the tuples is changed. Finally, compared to the previous program, the advanced version produces the same

RZP structure about 50 times faster, reducing the usual calculation time to a few minutes.

The shape of the RZP's aperture can be different depending on the purpose of the spectrometer. Along the y-axis, it is always limited by y_{min} and y_{max}, which were determined prior to the structure calculation, see section 3.1.2. These limits are mostly given by choosing applicable angles of incidence. A too long RZP would decrease the resolution as well, so it does not make any sense to exceed these limits. The lateral borders of the aperture are more flexible. As mentioned above, for a single RZP, the most simple shape is a rectangle. In lateral direction, the width w gives the coordinate limits: $-w/2 \leq x \leq w/2$. Prior to the data production, the lowest and highest number of zone edges included in the segment are determined. This list of n-values is then parted into tuples of two neighboring zone edges. With this list of n-value-tuples, a list of sextuples of ellipsis parameters (A_n, A_{n+1}, B_n, B_{n+1}, v_n and v_{n+1}) for each n-tuple is generated, with each entry representing one Fresnel zone. In the next step, all intersection points with the rectangle are identified and each zone edge segment is calculated by dividing the corresponding angular section according to the distribution law mentioned above. Depending on the diffraction order of use and the type of zones (parted, unparted, etc. as mentioned in section 3.6), a distinction of cases is needed to set the correct angular limits for each zone. Other than in the previous program, where this distinction was part of the calculation process of each zone, in the new version, all this is done prior to the actual polygon calculation, saving running time once again.

For trapeze-shaped apertures, the intersection points are simply determined mathematically as intersection between a straight line (with the slope given by the opening angle φ of the trapeze (see next section)) and the ellipsis.

Another aperture shape of interest is the maximum writable area between y_{min} and y_{max}, where the zone width does not fall below the fabrication limit. The curve that borders this area laterally can be derived from the line density vector field (see section 3.5). Half of the local grating period as defined in 3.38 gives the zone width fz:

$$fz = \frac{d}{2} = \frac{1}{2|\vec{d}_l|}.$$

For a minimum fabricable zone width fz_{fab}, the corresponding maximum line density $d_{l,max}$ is then given by

$$d_{l,max} = \frac{1}{2fz_{fab}}, \tag{3.59}$$

which leads to drop-shaped curves of constant line density on the RZP plane as shown schematically in the right graph of figure 3.7. Note that in the figure unrealistic RZP parameters were used for a better illustration. For an applicable RZP, these curves are much flatter, causing aperture shapes that are very similar to trapezes.

3.7.4 Array Calculation

In many RZP spectrometers, as described in detail the next section, several point-to point RZPs are implemented next to each other in a fanned-out array (see figure 3.13). These produce several individual focal points in one focal line at the same height on the detector plane. With a total opening angle ω of the fan, the foci are distributed according to the fan angle ω_i of each RZP "channel". Since most CCD detectors are not curved in any way, the entrance and exit arm lengths vary for each channel according to

$$R_{1i} = R_1 \cos\omega_i \quad \text{and} \quad R_{2i} = R_2 \cos\omega_i. \tag{3.60}$$

This way, the FZCs of all channels are located on one line parallel to the detector plane. The opening angle of the fan is limited by the detector width w_d to

$$\omega_{max} = \arctan\left(\frac{w_d/2}{L_{1,max} + L_{2,max}}\right), \tag{3.61}$$

with the projections of the entrance and exit arm of the outermost channel onto the RZP plane $L_{1,max} = R_{1,max}\cos\omega_{max}$ and $L_{2,max} = R_{2,max}\cos\omega_{max}$. To maintain the exact same height of the focal spots on the detector, the individual angle of incidence θ_i of each RZP channel must be readjusted to

$$\theta_i = \arcsin\frac{R_1}{R_{1i}\sin\theta}, \tag{3.62}$$

with the uncorrected entrance angle θ of a central channel.

Depending on the purpose of the spectrometer, many different designs of such an RZP array are possible. These will be described in detail in the next section.

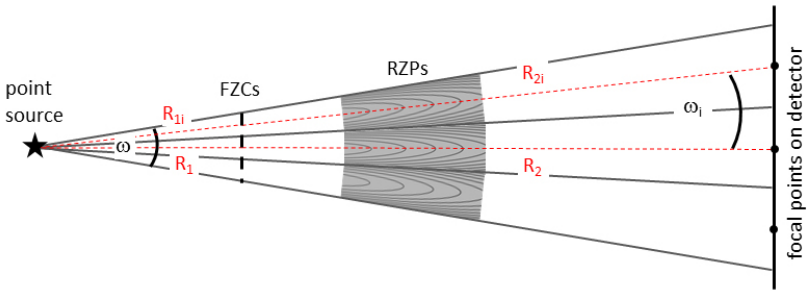

Figure 3.13: Scheme of optical path for a trapeze-shaped RZP. This is mostly used for RZP arrays (see section 3.8).

3.8 RZP Arrays (Multichannel Spectrometers)

3.8.1 Polychromatic RZP Arrays

A spectrometer with only one RZP usually has a very narrow full spectral range. To enlarge this range, there are several ways of combining RZPs to so-called multi-channel single shot spectrometers. Each channel then has an individual design energy. These design energies can either be adapted to the X-ray fluorescence energies of chemical elements of interest or they can be distributed quasi-continuously between a start and end energy of a certain range. The opening angle is adjusted to the width of the detector in the experimental setup, meaning mostly a CCD X-ray camera.

Element-specific Arrays

Multi-channel spectrometers with element-specific channels usually contain a small number of channels, such as 10 or 20. The RZPs focus at the fluorescence energies of a few chemical elements. The advantage of these spectrometers is that all element energies of interest can be recorded in one single CCD camera shot. This reduces the measuring time to usually a few seconds.
Figure 3.15 schematically shows a fanned-out RZP channel array structure with six channels and a measured X-ray camera image above. Each channel is made for a different photon energy, all of them focus in their first order and at the same height above the specular reflection, resulting in the same vertical position on the camera image. The set of focal points of design energies is called focal line. Around this focal line, other blurred spots from other energies appear in every channel. The blurred spots have a more or less rectangular shape as described in section 2.4.2. Each photon energy appears in several channels, but at a different vertical position and with a different spot width. The elements that the channels are designed for are

written into zero order shadows in the lower part of the image. The carbon signal for example appears in every channel. It is the first blurred spot below the focal line in the boron channel on the left, then shows in the focal line in the carbon channel itself, and then as blurred signal again in all the next channels, but above the focal line, at an increasing height. A small dashed white line through the carbon spots illustrates this behavior.
The analysis of the CCD image works in two dimensions: around the focal line, a vertically binned section with a height of a few pixel rows (shown as white rectangle) will yield a line spectrum with the peak heights revealing the element's concentrations in the sample. A horizontally binned section around the diffraction images of one single channel results in another line spectrum, featuring sharp and blurred peaks around the design energy.

For each channel, an energy scale can be calibrated, so that the vertical position of each peak can be assigned to a certain photon energy. This yields important information about energies other than the design energies, such as chemically shifted energy levels or different elements appearing in the sample. Both line spectrum types are shown in figure 3.14, with the information extracted from the CCD image in figure 3.15. While the peaks in the focal line spectrum are usually sharp and have fixed distances to each other, the peaks in the channel spectrum have different widths. The peak height and peak-to-noise-level depends on the number of pixel rows or columns, that are summed up for these spectra. Of course, there is a limit to both numbers. Since one channel fills a certain horizontal space above which the spots from other channels interfere in the channel spectrum, and the peaks in the focal line spectrum will be widened by energies close to the design energy with an increasing number of pixel rows. Here, the best compromise for clear peaks must be found individually for every RZP array spectrometer.

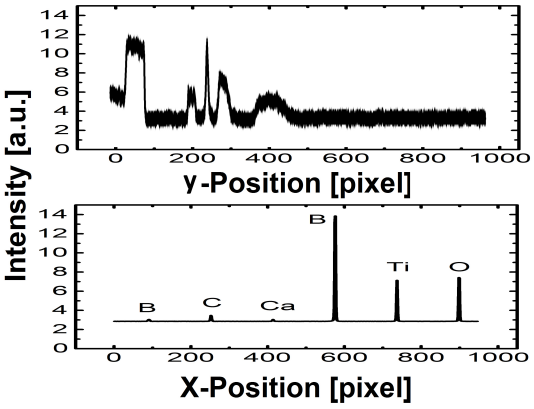

Figure 3.14: Two different types of line spectra that can be extracted from the diffraction images.

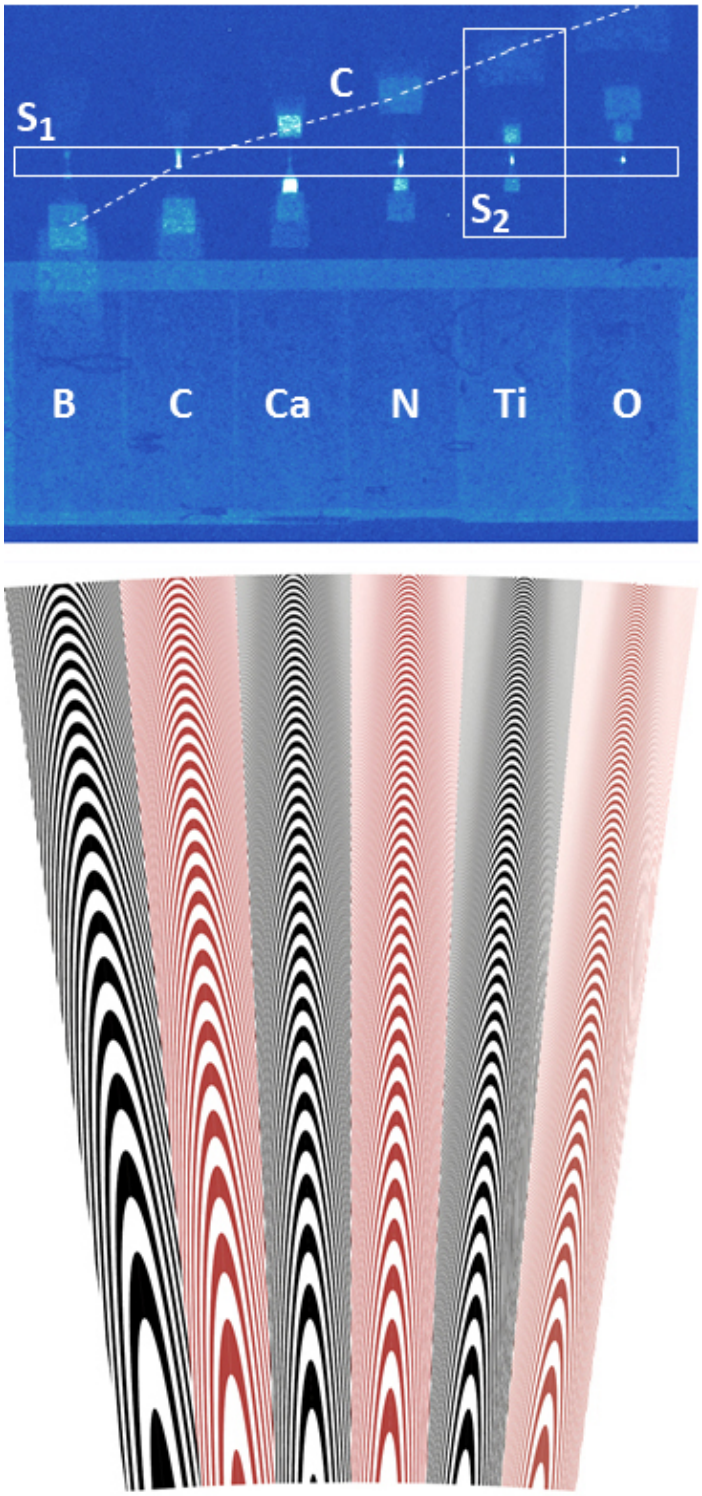

Figure 3.15: Schematic array of 6 RZPs with diffraction image.

Quasi-continuous Arrays

Another type of RZP array spectrometer is a quasi-continuous array. Here, the channels are very narrow and there is a large number of them (100, 200 for example). The design energies are no more fixed to specific element energies, but are distributed over a certain energy range. There are two different ways to distribute them. With equidistant energy steps or according to a distribution law such that every channel has the same energy resolution $E/\Delta E$ in the focal spot. At a total number of RZP channels N_c, for an energy range between E_{min} and E_{max}, with equidistant energy steps, the energy of the ith channel is

$$E_i = E_{min} + i \cdot \frac{E_{max} - E_{min}}{N_c}, \tag{3.63}$$

with $i \in \{0, 1, ..., N_c\}$. With an exponential disribution law,

$$E_i = E_{min} \left(\frac{E_{max}}{E_{min}} \right)^{\frac{i}{N_c}}, \tag{3.64}$$

with $i \in \{0, 1, ..., N_c - 1\}$, the energy resolution $E/\Delta E$ along the focal line is constant.

This law is derived as follows: The resolvable energy difference ΔE_i for the RZP array is given by the FWHM of the envelope function enclosing the channel peaks as shown in figure 3.16. The peak heights and hence the envelope depend on the number of pixel rows from the CCD image that are summed up for the line spectrum as described for the element specific arrays in the previous section. This number of rows is usually chosen in such a way that the FWHM of the envelope matches two channel widths. Therefore, the FWHM ($=\Delta E$) along the focal line energy scale of the spectrometer is given by two times the energy difference between two neighboring channels $i + 1$ and i:

$$\Delta E_i = 2 \cdot (E_{i+1} - E_i) .$$

With the energy of the i-th channel (3.64) this leads to

$$\begin{aligned}\Delta E_i &= 2 \cdot \left(E_{min} \left(\frac{E_{max}}{E_{min}}\right)^{\frac{i+1}{N_c}} - E_{min} \left(\frac{E_{max}}{E_{min}}\right)^{\frac{i}{N_c}} \right) \\ &= 2 \underbrace{E_{min} \left(\frac{E_{max}}{E_{min}}\right)^{\frac{i}{N_c}}}_{E_i} \left(\left(\frac{E_{max}}{E_{min}}\right)^{\frac{1}{N_c}} - 1 \right) \\ &= 2E_i \left(\left(\frac{E_{max}}{E_{min}}\right)^{\frac{1}{N_c}} - 1 \right),\end{aligned}$$

which then leads to an energy resolution of

$$\frac{E_i}{\Delta E_i} = \left(2 \left[\left(\frac{E_{max}}{E_{min}}\right)^{\frac{1}{N_c}} - 1 \right] \right)^{-1} = const. \tag{3.65}$$

Figure 3.17 shows an RZP array spectrometer with 200 channels. Here, the focal line appears below the specular reflection, meaning that the array was made for its -1^{st} order. The blurred energy spots are now narrow vertical lines, as their width is set by the channel width. Each photon energy signal now shows in an x-shaped form, with the center of the x at the channel with the design energy closest to this photon energy.

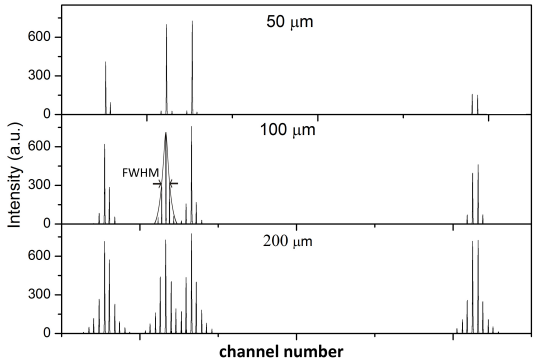

Figure 3.16: Simulated line spectrum exracted from a ray traced diffraction image, cut out around the focal line at different slit sizes.

In this specific spectrometer, the optimum profile depth varied a lot between the channels, so that they were etched in three groups, each with a different depth, indicated by different color tones in the schematic array structure below the camera image as well. This is why in the diffraction image there are three sections with different spot intensities and signal-to-noise-ratios. With this type of RZP array spectrometer, all necessary information can be found in the line spectrum binned around the focal line. The resolution now depends mainly on the number of pixel rows binned, as mentioned above and shown in figure 3.16 for three different "slit widths". The spectrum was extracted from simulated data (ray traced), where there was no camera

image to analyze, but a section of ray traced footprint, cut out by horizontal slits at different widths. The spectrum with the smallest slit, 50 μm, does not yield a smooth enough envelope function, while at the largest slit, 200 μm, the signals from two photon energies start to merge. The optimum slit size is 100 μm.

3.8.2 Monochromatic RZP Arrays

In some experiments, the goal is not to investigate the chemical composition of a sample, but to detect a very weak signal. For this purpose, as many photons as possible have to be brought into the focal line. One solution is to use an RZP array, where all channels have the same design energy, that meets the element signal of interest. The left side of figure 3.18 illustrates the discrete array and camera image equivalent to the previous sections. The RZPs work in -1^{st} order. For the analysis of the signal, now a region of interest can be selected around the focal line and for example the signal intensity in dependence of the incoming photon energy (absorption spectroscopy) can be detected. The channel width is limited in its maximum by the fabrication limit and in its minimum by a clear separation of the focal spots.
Another version, a continuous array, can be reached by decreasing the channel size to one data point per Fresnel zone edge. Now, all the data points from the same Fresnel zone edges of the neighboring channels can be connected to form new zones (see right part of figure 3.18). The curvature of the zones depends on the distance to the detector: the closer the detector, the stronger the curvature. The resulting camera image shows a continuous line as focus, which can be evaluated in the same way as the set of points. While the continuous structure is easier to fabricate due to the larger zone widths, the resulting camera image is very hard to align (see section 6.2.2).

3.9 Modified RZPs

3.9.1 Astigmatic RZPs

Another possibility to create a continuous horizontal focal line is an astigmatic RZP. The structure is calculated easily by multiplying all structure coordinates in one dimension with a certain stretching factor. This causes the sagittal and meridional focal plane to separate, equivalent to refractive lenses. If the data points on the horizontal structure axis are multiplied with a factor larger than one, the focal spot will be

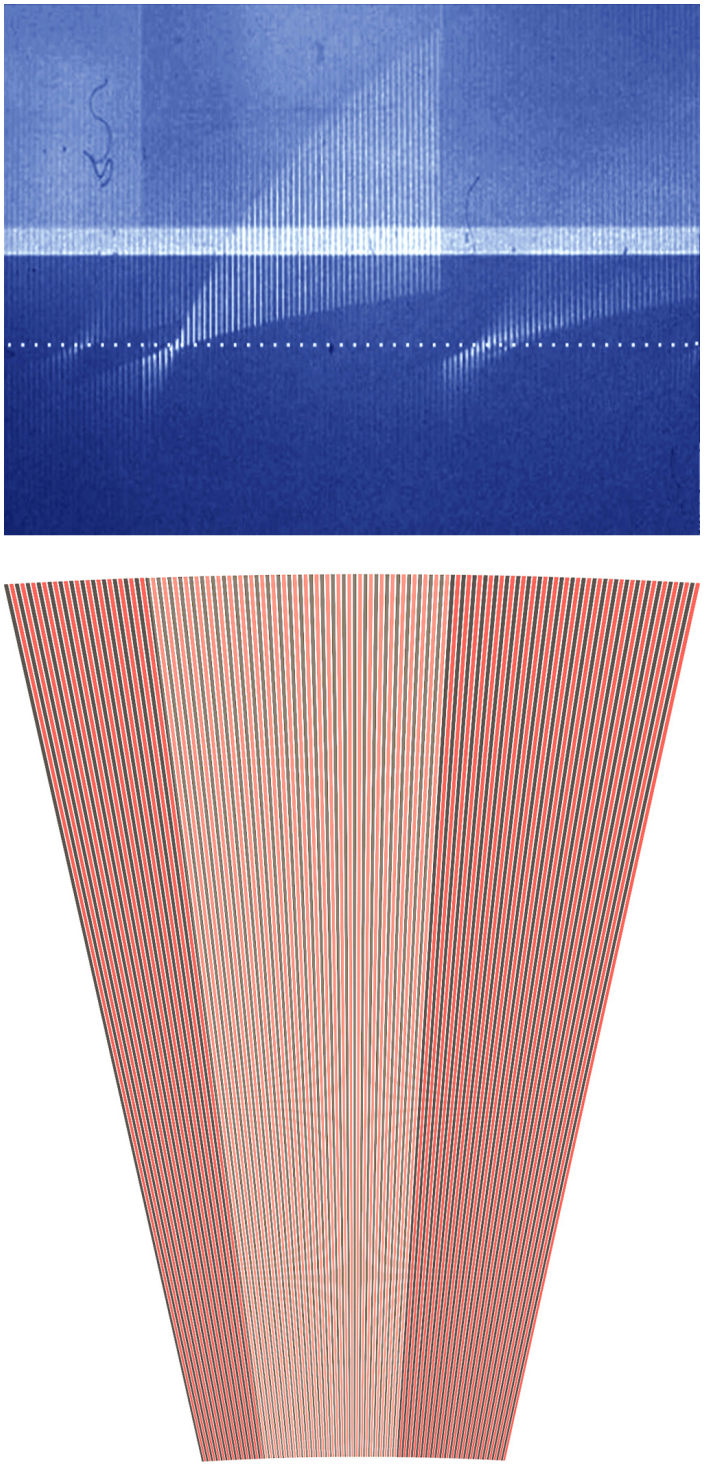

Figure 3.17: Schematic array of 200 RZPs with diffraction image.

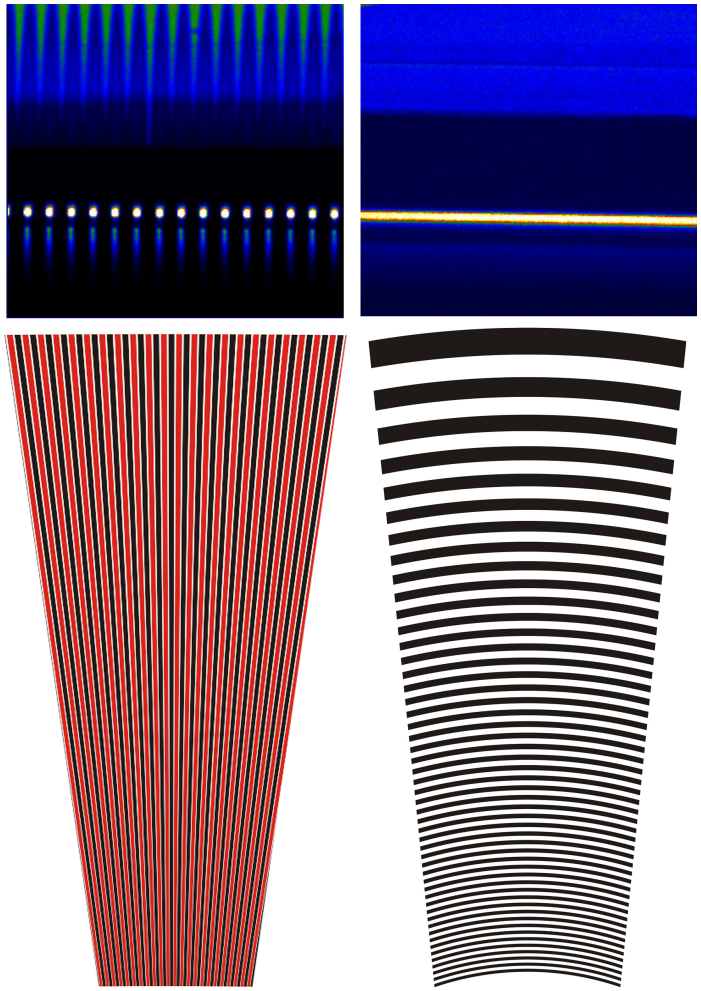

Figure 3.18: Schematic array of 40 RZPs (left) and a continuous array (right) with the same design energy and corresponding diffraction images.

stretched horizontally.
Figure 3.19 shows a single unstretched RZP (left) with the resulting camera image compared with an astigmatic RZP (on the right), stretched with a quite large factor, causing a continuous long focal line. Even though the zones of the astigmatic structure are curved upwards like the single RZP, and the zones of the continuous array is curved downwards, the resulting horizontal focal lines in the camera images are very similar. This is based on the fact that in this particular experiment, within which the camera images were recorded, only a small region of the structure was illuminated. For small opening angles, where just an inner part of the structure is illuminated, both structure types show more or less the same results as a VLS grating. For larger opening angles though, the different curvatures cause a significantly different behavior in the outer parts of the focal line. The results of theoretical considerations on this matter were published in detail in [16], showing that the abbreviations in the outer parts are the smallest with a continuous array as described in the previous section.
Like the continuous array structure, the zones of the astigmatic RZP are much wider than those of normal point-to-point RZPs, especially in the laterally outer parts, which makes them attractive for an easier fabrication.

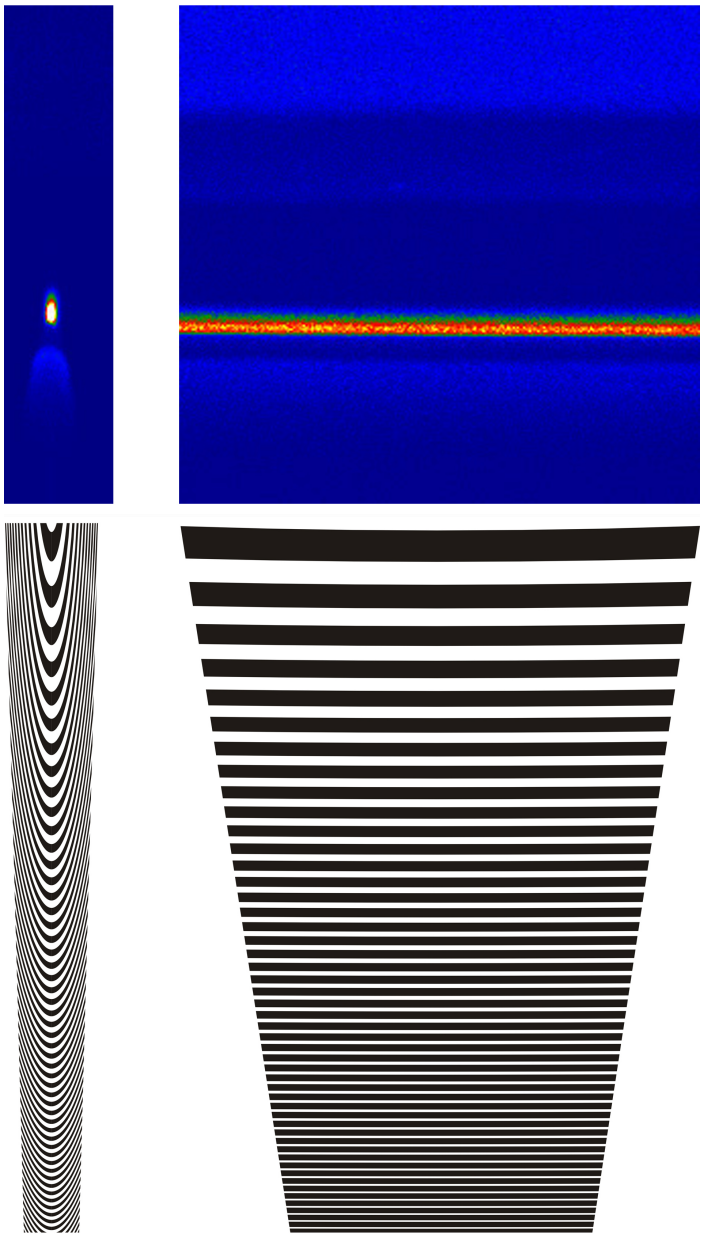

Figure 3.19: Single focusing RZP (left) and astigmatic RZP (right), with camera images above.

3.9.2 Telescopic RZPs

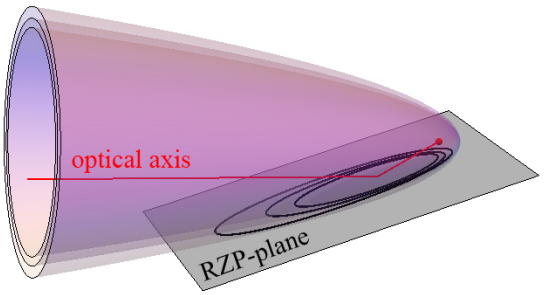

Figure 3.20: Telescopic RZP as intersection between 3D Fresnel paraboloids and a plane. Here, the entrance arm length is infinite and the exit arm length is exactly the focal length of the RZP.

Though not characterized within the framework of this thesis, for the sake of completeness and for a successive experiment, RZPs that produce a focus point from an incoming parallel beam should be mentioned. These so called telescopic RZPs have a wide range of use in astrophysics, where very far away light sources. Still, in synchrotrons and free electron lasers, it is possible to produce X-ray beams with a very low divergence that can be considered parallel (see APS experiment in section 5.3). The 3D Fresnel zones of a telescopic RZP are no more ellipsoids but paraboloids with the image point in their focus. The zones on the RZP are still shaped elliptically though, see figure 3.20. Mathematically, this means that the distance between the FZC on the RZP and the source is infinite ($R_1 = \infty$), leading to a phase shift function of:

$$\Phi(x,y) = \lim_{R_1\to\infty}\left(\frac{\pi}{\lambda}\left(\sqrt{x^2+(R_1\cos\theta-y)^2+(R_1\sin\theta)^2}\right.\right.$$
$$\left.\left.+\sqrt{x^2+(R_2\cos\theta-y)^2+(R_2\sin\theta)^2}-(R_1+R_2)\right)\right),$$

as a limit of the point-to-point version in equation 3.32. The root term with R_1 and the summand $-R_1$ converge to

$$\lim_{R_1\to\infty}\left(\sqrt{x^2+(R_1\cos\theta-y)^2+(R_1\sin\theta)^2}-R_1\right) = y\cos\theta,$$

leading to

$$\Phi(x,y) = y\cos\theta+\sqrt{x^2+(R_2\cos\theta-y)^2+(R_2\sin\theta)^2}-R_2, \tag{3.66}$$

with the RZP's focal length $f = R_2$.

4 Realization of RZP Spectrometers

Subsequent to the parameter optimization and the calculation of the Fresnel zone structures, the RZPs must be realized. To transfer the Fresnel zones from the digital data onto a solid substrate, a fine patterning technique is needed, although for some RZPs, especially if made for the lower soft X-ray range, UV-lithography is sufficient enough to ensure well-defined structures (down to 500 μm). The RZPs that were fabricated within the framework of this thesis have much smaller zone widths and were hence solely realized with e-beam lithography. The following sections provide an overview of their typical lateral dimensions, profile depths, inaccuracies, as well as a detailed description of their fabrication via e-beam lithography.

4.1 Conventional Fluorescence Detectors

For the analysis of the chemical composition and structure of sample materials in solid or sometimes liquid (see jet experiment, section 6.2) phase, the characteristic X-ray lines emitted by the sample are of crucial interest. Fluorescence emission in the X-ray range can be, as mentioned above, caused by X-rays themselves or high-energy electron beams. For many small scale laboratory uses, X-ray tubes or the electron beams from scanning electron microscopes (SEMs) serve as sources. On larger scales, synchrotron or even free electron laser facilities offer much higher photon fluxes.

Basically, there are two different methods of X-ray fluorescence spectroscopy: energy dispersive spectroscopy (EDS) and wavelength dispersive spectroscopy (WDS). EDS detectors offer faster overviews over large energy ranges, while WDS detectors produce better resolutions within only small detection ranges. Both analyze the sample emission as counts over photon energy and can be applied for X-ray or electron beam exitation sources, but work on a completely different principle.

The central component of an EDS system is a solid-state detector, consisting of a semiconductor crystal. As each X-ray photon hits the detector, a very small current is produced by knocking out electrons from the semi-conductor. Each electron ejected from a silicon electron shell consumes about 3.8 eV of energy from the X-ray. Therefore, an X-ray photon starting with an energy of for example 7471 eV (Ni K_α-line) will produce a current of about 1966 electrons [19]. By measuring the amount of current produced by each X-ray photon, the original energy of the X-ray can be calculated.

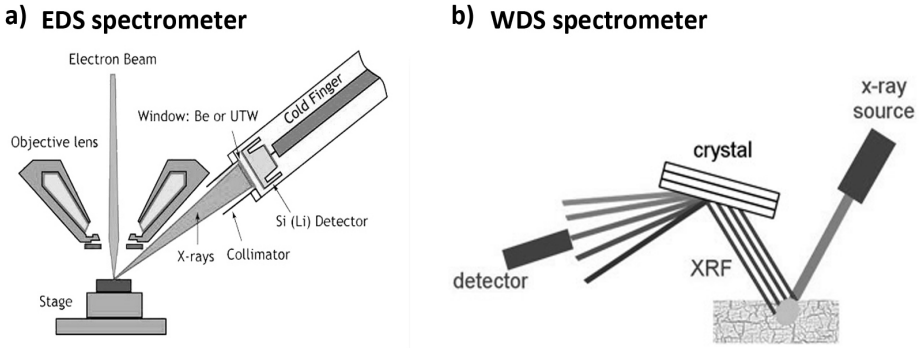

Figure 4.1: a) a typical ED-spectrometer, implemented in an electron microscope. The electron beam is focused by a lens onto the sample and exites fluorescent X-rays, that are collimated onto the Si crystal detector. The lithium drifted silicon crystal is mounted on a cold finger connected to a liquid nitrogen reservoir stored in a Dewar. Low temperature is essential for noise reduction and to limit the mobility of the lithium ions initially introduced in the silicon crystal [17]. b) a typical WD-spectrometer, used with an X-ray source. The X-rays excite X-ray fluorescence on the sample and are diffracted by a crystal according to Bragg's law (2.4, section 2.3). While scanning, the crystal is rotated so it deflects one energy at a time onto the detector, such as gas flow proportional counters [18].

An EDS spectrum is essentially a histogram of the number of X-rays measured at each energy.

WDS differs from EDS in that it uses special crystals to separate its raw data into spectral components (see figure 4.1). According to Bragg's law, different wavelengths are diffracted at different angles. In the scanning process, the crystal is rotated while the deflected photons are recorded. WDS has a much finer spectral resolution than EDS. In WDS, only one a small energy range can be analyzed at a time, though. Figure 4.2 shows two overlapping spectra, recorded with the two methods. The WD-spectrum clearly has a much higher resolution, whereas the ED-spectrum is shown for only a small section of the entire recorded range. EDS detectors typically have resolutions of about $\Delta E = 150$ to 600 eV, while WDS detectors offer $\Delta E = 5$ to 20 eV [20]. RZP spectrometers have the great advantage of combining the benefits of both methods. Large energy ranges can be measured simultaneously with a high resolution. The physical properties of RZPs that enable these spectroscopic features will be explained in the following.

4.2 Typical Structure Dimensions

In table 4.1, the typical dimensions of the RZPs fabricated at the HZB within the framework of this thesis, are shown. Generally, they can be split into two groups: soft

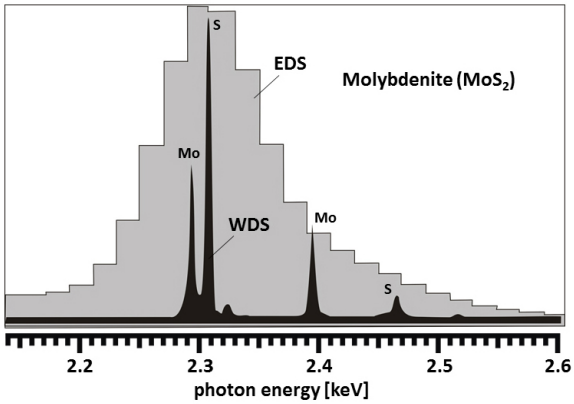

Figure 4.2: Comparison between a typical WD- and ED-fluorescence-spectrum. The EDS channel counts are shown in gray, the WDS counts in black. Due to the much lower resolution (typically $\Delta E = 150$ to 600 eV) of an EDS detector compared to a WDS detector ($\Delta E = 5$ to 20 eV) [20], the X-shell peaks of Molybdenum and Sulfur can not be resolved in the ED-spectrum [18].

X-ray and hard X-ray RZPs. The wavelengths for soft X-rays roughly lie in the range between 0.1 and 10 nm. The most prominent soft X-ray RZP spectrometers in this thesis were made for a photon energy of 640 eV or a wavelength of 2 nm, respectively. Other RZP arrays ranged down to photon energies of 180 eV (wavelengths of 7 nm). For hard X-rays, only one photon energy was focused upon: the Ni K_α edge at 8333 eV. This corresponds to a wavelength of 0.15 nm.

The angles of incidence are very low in both cases, due to the grazing incidence of total external reflection zone plates in the X-ray range. For the soft X-ray RZPs, the typical angles of incidence range around 2°, for hard X-rays, they are typically even one order of magnitude lower, around 0.3°.

The total width and length of the structured area as well as the width of the smallest zone depend on the fabrication limit. Of course generally, the Fresnel zones of soft X-ray RZPs are larger than those of hard X-ray RZPs. Therefore, soft X-ray RZP can be realized with more Fresnel zones, up to a cm in width. Along the optical axis (lengthwise), the variation on zone width is often rather low, so they could be written to lengths larger than 10 cm. Here, the size of the substrates that can be handled by the e-beam writer comes into play and sets another limit. With some safety distance to the substrate edges or some space left on the substrate for adjustment RZPs, this leaves a typical length of about 8 cm on typically 10 cm substrates. In the hard X-ray range, these values are again decreased by one order of magnitude approximately. They are only 0.3 mm wide and around 10 mm long. Here, smaller substrates were used. The smallest zone width was set as 40 nm for hard X-ray RZP and a little higher, 70 nm, for soft X-ray RZPs. The fabrication limit was found as the best

compromise between usable RZP area and structure quality (meaning efficiency). For the hard X-ray RZPs this limit was set a little lower because otherwise the functioning area would have been too small to operate the RZP sufficiently.
The ideal profile depth of an RZP can vary significantly with the incoming angle. For soft X-ray RZPs, the value can vary between 10 and 25 nm. Due to the lower angles of incidence on the one hand and the shorter wavelength on the other hand, the typical profile depths of hard X-ray RZPs are roughly equal; the typical value for the 8333 eV is 10 nm.

	typical wavelengths	**incident angles**	**length**	**width**	**smallest zone size**	**profile depth**
soft X-rays	2 - 7 nm	~2°	~8 cm	~1 cm	~70 nm	~17 nm
hard X-rays	0.15 nm	~0.3°	~10 mm	~0.3 mm	~40 nm	~10 nm

Table 4.1: typical dimensions of RZPs fabricted at the HZB within the framework of this thesis

Figure 4.3 illustrates the zone pattern (upper part of the image) in the RZP's coordinate system as described in section 3.6 and line density (graph in lower part) of a typical soft X-ray RZP on a larger scale. Here, the full range including the source and detector point (as projections onto the RZP plane) is shown. To indicate the shape Fresnel zones, the zone edges are shown as black lines. For simplification and visibility, they are shown in three packs: every 10^{4th} zone in the inner pack of ten, every $(10^5)^{th}$ zone in the next pack of ten and every $(10^6)^{th}$ zone in the outermost pack up to the $(5 \cdot 10^7)^{th}$ zone. The red rectangle marks the part of the RZP that was actually used. The source and detector point projections are shown as red dots. The black lines clearly reveal the elliptical shape of the zones and the large gradient of the zone width, especially in the lateral dimension (here vertical).
The lower part of 4.3 shows the local line density of the same RZP along different lines parallel to the y-axis for 11 different x-values ($x = 0mm, x = 1mm, x = 2mm, ...x = 10mm$). At $x = 0mm$, meaning along the projection of the optical axis, the line graph includes the singularity of the FZC, where the line density is zero. Within the range of fabricable sections of RZPs (marked as red area), the line density varies almost perfectly linear along the y-axis (note the logarithmic scale). At very large distances from the FZC however (larger than the maximum of R_1 and R_2), this nearly linear gradient changes to a logarithmic one, running towards the limit of $d_l = \frac{2}{\lambda}$. This absolute limit depends only on the photon energy, not on any geometrical parameter.

It is exactly the distance between two zone edges that cause a phase shift of π at a perpendicular incidence on the zone edges. In x-direction the nature of the variation of the local line density is similar. Due to the very short radius of the Fresnel zone ellipsoids in this direction, the local line density quickly reaches much higher values than in y-direction. In the far outer regions (at much larger distances than the maximum of R_1 and R_2), the line density approaches the absolute limit as well. This limit results in a zone width limit of half the wavelength, for this particular example of a soft X-ray RZP this corresponds to around 1 nm, which is about the size of a single Carbon atom (reference). For hard X-rays (8.3 keV), this limit is one order of magnitude smaller: 74 pm. This is approximately the size of a single carbon atom.

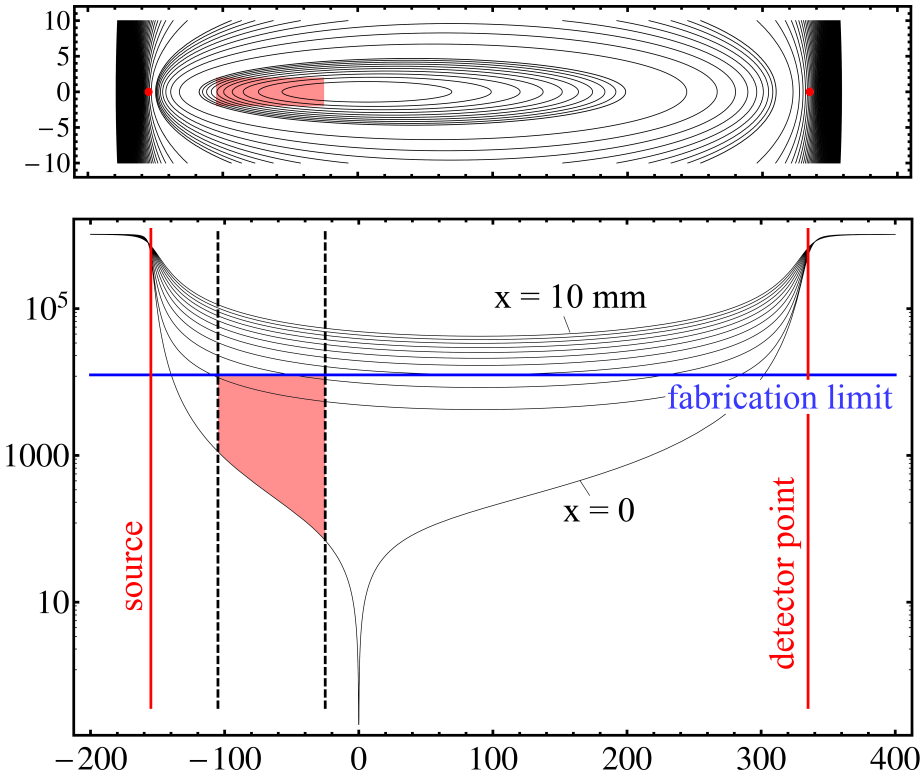

Figure 4.3: Schematic line density vector field for a point-to-point RZP.

4.3 Fabrication Technique

The RZPs that were fabricated to be used within the projects of this thesis were all realized with e-beam lithography. As described in detail in the Diploma thesis prior to this work, there are 6 basic steps in the fabrication process (see figure 4.4).

1. The first step is the coating of a silicon substrate with an e-beam sensitive photo resist, which is usually a solution of long-chain polymers that are split into smaller pieces by the electron beam, making them soluble in the developer. The substrate has to have a super-polished surface with no more than 1 nm roughness (rms). In addition, the substrates must have a certain thickness (in our case 1 cm) to ensure that any surface slope errors are kept to a minimum. Common Si-wafers do not fulfill this criterion.
   The resist is spin coated onto the substrate to ensure an evenly thick resist layer. After the coating, the resist must be baked at around 130°C to evaporate the remaining solvent. Usually, for RZPs, the resulting resist thicknesses lie in the range between 100 and 200 nm, depending on the desired smallest zone size and the e-beam dose rate.

2. In the second step, the resist is exposed to the electron beam. The e-beam writing used at the HZB to pattern RZPs is a high-voltage machine (Vistec EBPG 5000+) for high precision patterning down to 1 nm. The actual resolution of the written pattern is limited by scattering effects though. The zone pattern file of the format "Graphic Data System" (GDS) consisting of filled polygon areas in an xy-coordinate plane, calculated as described above is transferred into a pattern of exposure shots by the machine's internal software. For each shot, the ideal dose rate is calculated and assigned to the shot. At the edges of the exposed areas and within very narrow areas, the dose has to be lower to reduce the scattering.

3. After the e-beam exposure, the resist can be developed. In this wet chemical process, the solvent of the developer solution bloats the exposed short chain polymers so they disentangle and diffuse into the developer.

4. With the zone pattern now formed by the unexposed resist, after cleaning any remaining solvent from the free surface areas, the pattern is now transferred into the silicon substrate via reactive ion etching. The etching machine used is a Plasmalab80+ from Oxford Instruments and works via ionizing reactive gases such as SF_6, O_2, CHF_3, H_2 or C_4F_8 with a high frequency alternating field. The etching process is a combination of chemical reactions and mechanical removal of surface material as a high voltage additionally accelerates the reactive ions onto the substrate. For the cleaning, oxygen has the best effects, as it does not react with the silicon. For etching into the silicon, mostly CHF_3 is used.

5. In the next step, the unexposed resist is removed from the substrate. This process is called lift-off. Mostly, simple acetone can be used as solvent of the resist. After the wet chemical relief, again, any remaining rests of solvent of resist have to be cleaned off the surface with reactive oxygen.

6. In the final step, the RZP surface is coated with a highly reflective material such as nickel or gold. The material is sputtered onto the substrate in a high-voltage sputtering machine (Bestec HV 8A). Compared with coating via evaporation, sputtering causes more smooth and even layers.

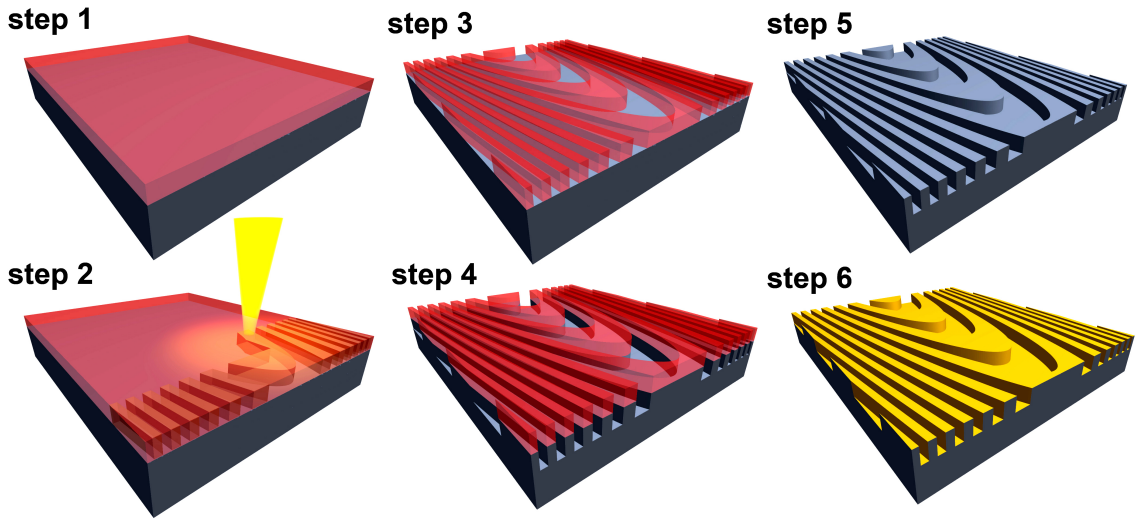

Figure 4.4: The 6 basic steps of RZP fabrication via e-beam lithography

5 Characterization in Hard X-rays

5.1 State of the Art

The work on focusing total external reflection zone plates in the hard X-ray range started in 2012 with a prototype fabricated on a simple wafer piece. This prototype was made for the Ni-K-edge as a typical fluorescence line in the hard X-ray range and the geometerical parameters were optimized to fit one of the hard X-ray beamlines at BESSY II, the KMC-2. As shown as an overview in table 5.1, the entrance arm length is very long (10 m) compared to the exit arm length (500 mm). This ensures a strong demagnification. To define a source at the exact 10 m distance to the RZP, a pinhole was inserted into the beam. To reach total external reflection, a very low angle of incidence (0.3°) was chosen. The diffraction image was then recorded with a CCD camera at the distance of the exit arm (see detailed setup description in next section). The prototype was designed for first order use. The size of the demaginfied image (focal point) could be optimised to 16.4 μm (v) x 42 μm (h). Compared with simulated ideal values of 12.8 μm (v) x 16.4 μm (h), this result was unsatisfactory. The main reason was the surface quality of the substrate which lead to the appearance of several maxima in the focal area (see image 5.2).

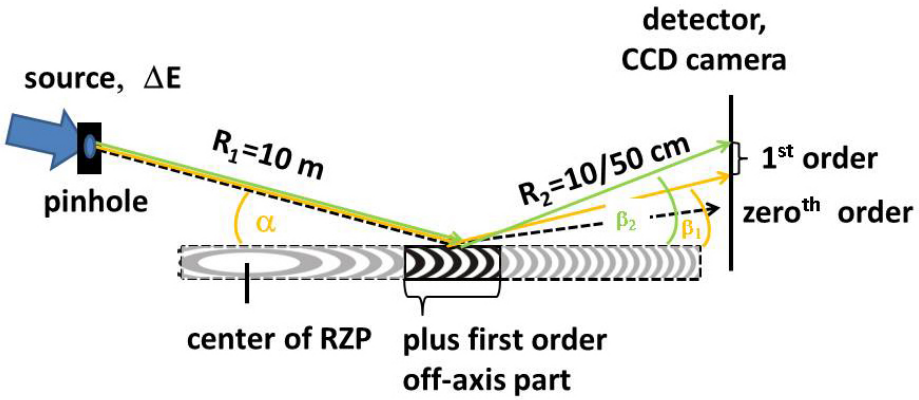

Figure 5.1: Schematic setup of the first prototype test of a hard X-ray RZP at the beamline KMC-2 at BESSY II.

More promising results were reached with a subsequent set of two RZPs on a super polished substrate. One RZP was made for point-to-point focusing like the prototype,

but in on-axis mode, meaning that the focal spot appears in the 0^{th} order. The other RZP was a one-dimensional varied line spacing grating (VLS grating), focusing in only one dimension (in this case in sagittal direction). Figure 5.3 shows the resulting diffraction images. On the left side (image of the two-dimensional RZP), the image is a spot and on the right side (VLS grating), it appears as vertical line. Both are surrounded by the specular reflection. The VLS grating served only as a proof-of-principle of the focusing properties of RZPs and VLS gratings in this energy range, while the size of the focal spot of the RZP could be minimized to 2.9 μm (v) x 3.7 μm (h), close to the expected values. Moreover, the shorter exit arm length comes into play here, causing an even stronger demagnification. In addition to the focal spot size,

	E [eV]	R_1 [m]	R_2 [mm]	α [°]	β [°]	θ [°]	Δy [mm]	L [mm]	order
prototype	8333	10	500	0.3	0.4	0.35	54	10	1
on-axis	8333	10	100	0.35	0.35	0.35	0	10	/

Table 5.1: Parameters of the first two total external RZP in hard X-rays, the prototype and an on-axis RZP. With the photon energy E, the entrance and exit arm lengths R_1 and R_2, the angle of incidence α, the exit angle β, the incident angle at the FZC θ and the distance between the FZC and the central point on the RZP Δy

.

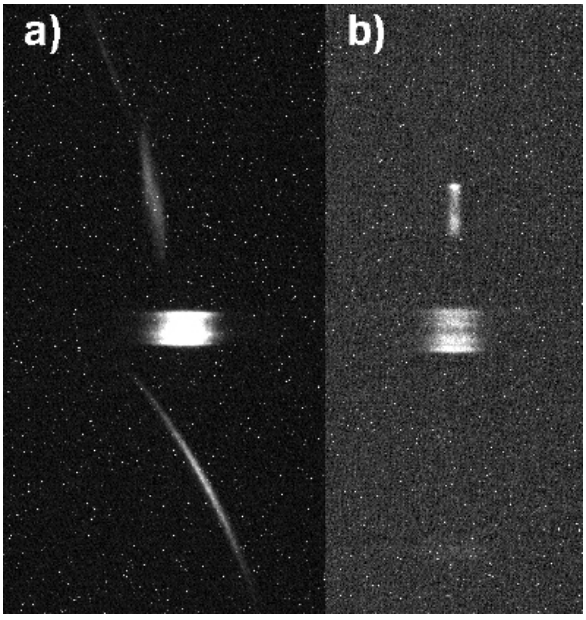

Figure 5.2: Diffraction image of prototype RZP

the dispersive properties of the prototype RZP were investigated. For three different incoming photon energies, 8000 eV, 8333 eV and 9000 eV, the vertical position of

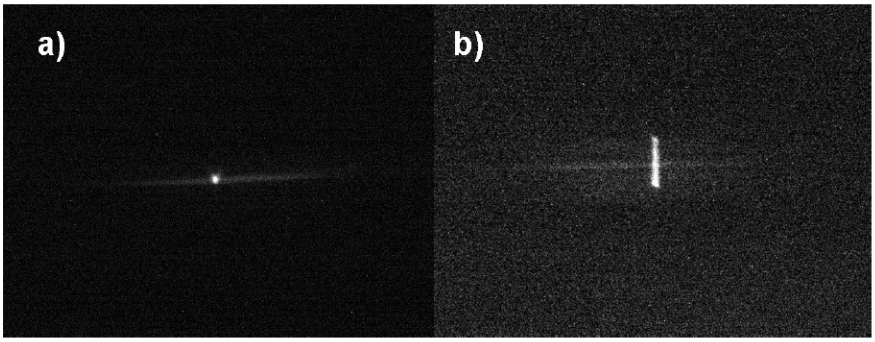

Figure 5.3: Diffraction image of on-axis RZP and VLS grating

the focal spot was recorded (see figure 5.4. The behaviour confirms the nearly linear connection between photon energy and vertical shift. Within 1000 eV, the spot is shifted by 41 $\pm$ 2 μm, which, with the vertical FWHM of the focal spot (16.4 $\pm$ 2.6 μm), results in an a weak energy resolving power lower than $E/\Delta E = 20$. In

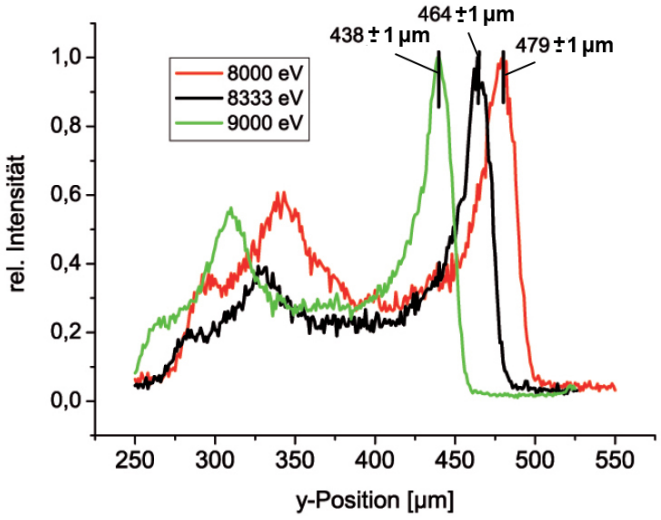

Figure 5.4: vertical shift of focal spot with incoming photon energy

summary, it was proven that the imaging and dispersive properties of total external reflection zone plates showed as expected. The biggest problem was the distortion of the focal spot of the off-axis prototype, due to a minor substrate quality. On the other hand, the on-axis point-to-point RZP on a better quality substrate worked well and paved the way to well-focusing off-axis RZPs in the hard X-ray range. All subsequent designs and measurements on this matter were done within the framework of this thesis, starting with a row of experiments at the same beamline at BESSY II, as described in the next section.

5.2 Characterization at BESSY II

5.2.1 New RZP Design

The first measurements done for this thesis were conducted at the KMC-2 at BESSY II. The hard X-ray beamline offers a manipulator stage at 10 m distance to the experimental hutch. Therefore, the RZPs used at this beamline are optimized for an entrance arm length of 10 m, as done for the prototype. The new RZP was chosen to operate in -1^{st} order, for the advantage of a larger acceptance angle, meaning more light in the focal spot (see parameters in table 5.2). The exit arm length was kept at 100 mm like the on-axis RZP, for a strong demagnification. The new RZP was fabricated onto a super polished substrate to ensure that no surface irregularities could distort the focal spot.

E	R_1	R_2	α	β	θ	Δy	L	**order**
8333 eV	10 m	100 mm	0.3°	0.15°	0.3°	-50.3 mm	10 mm	-1

Table 5.2: Parameters of the -1^{st} order off-axis RZP for characterization at BESSY II.

5.2.2 Setup of the Experiment

Downstream of the refocusing mirror of the KMC-2, at 10 m distance to the RZP, a pinhole of 200 μm diameter was inserted into the beam to define a secondary source (see figure 5.5). The beam was focused onto the pinhole with the mirror to ensure a high flux coming through. At the same grazing incidence angle (0.3°), the RZP was illuminated and the diffraction image was recorded with a CCD camera at the exit arm length of 10 cm. A new camera type was used (Rigaku XSight Micron), with an effective pixel size of 0.65 μm, about a twentieth of the 13.5 μm used in the previous experiments. The RZP was controlled and adjusted to its best position by a 6 degrees of freedom goniometer. Due to these many variable coordinates, the adjustment procedure can be time consuming. To avoid this, a repeatable procedure was developed, as described in the next section.

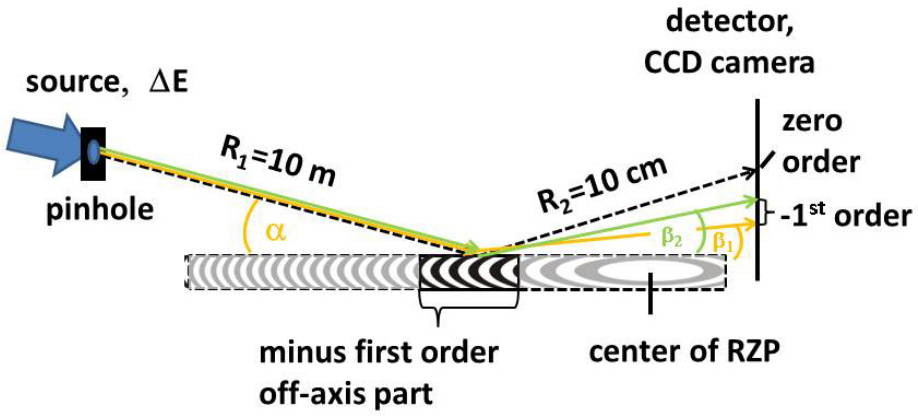

Figure 5.5: Schematic setup of the RZP characterization at the beamline KMC-2 at BESSY II.

5.2.3 Alignment Procedure

In an RZP spectrometer setup, the substrate with the RZP structures is mounted on a goniometer with up to 6 degrees of freedom (see figure 5.6: the translations along and rotations around all three spacial axes. Usually (and within this thesis), the axis parallel to the RZP's optical axis is labeled "z", the axis orthogonal to the RZP plane is labeled "y" and the lateral axis is labeled "x". In analogy to aviation and space technology, the rotation around z is called "roll", the rotation around y "yaw" and the rotation around x "pitch". All changes in any degree of freedom affect the size or shape of the diffraction image of the RZP. In the CCD image, the dispersion direction (within one channel or RZP) is set as "vertical" and the lateral direction as "horizontal".

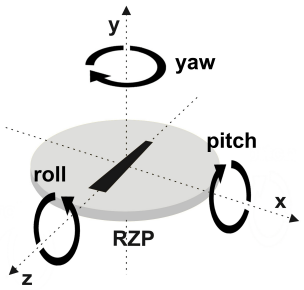

Figure 5.6: The 6 possible degrees of freedom on an RZP goniometer.

1. It is advisable to start with the direct beam in the CCD image. So in the beginning, the RZP must be low enough in y not to block any direct light. The direct light should be centered in the CCD or cover the whole range.

2. The RZP can then be moved upwards until half of the direct beam is cut off. So y is the first axis to (roughly) adjust.

3. "Pitch" changes the incoming angle. Now, at very low angles close to zero, the reflection of the substrate will appear. If the CCD is large enough to cover both the reflection (0^{th} order) and the direct beam, by the distance between the two signals the ideal incoming angle can be roughly adjusted. But, in most

cases, due to the limited range of the CCD, the position of the camera has to be changed vertically to follow the reflection.

4. If x is misaligned, the 0^{th} order surrounded by the substrate reflection will not be in the center of the CCD. So, if necessary, with x, the RZP can be moved into the beam. By now, the diffraction order of interest (DOI, in most cases 1^{st} or -1^{st}) should have appeared above or below the 0^{th} order. Especially in vertical direction, changing the incoming angle significantly distorts the focal point. Thus, the ideal pitch position is found by minimizing the vertical size of the DOI.

5. Now, the edges of the RZP (or any alignment feature, see next subsection (6.2.2)) are visible in the 0^{th} order. They should be exactly vertical in the CCD image. Any tilt indicates a wrong yaw angle. This way, yaw is adjusted roughly.

6. At this point, the DOI of a single RZP should have a point-like shape. A misalignment in roll will result in a mostly vertical distortion as well, so now, if necessary, roll can be adjusted by minimizing the vertical spot size again.

7. For a finer adjustment of the very sensitive yaw angle, now the shape of the focal spot serves as indicator. If yaw is slightly wrong, the focal spot will be distorted in both directions and have a tilted banana-like shape.

8. Since often the depth of field of the RZPs is quite large, adjusting z is not so critical. However, z is optimized by finding the smallest possible focal size in both directions. In practice, unfortunately the z axis is often not exactly in the beam plane. Consequently, pitch and yaw have to be permanently re-adjusted in the process.

9. For fine focusing, now a three dimensional, fine-stepped cube of yaw, pitch and z can be recorded any analyzed by the size of the focus in both dimensions to find the best possible focusing with the given accuracy of the goniometer.

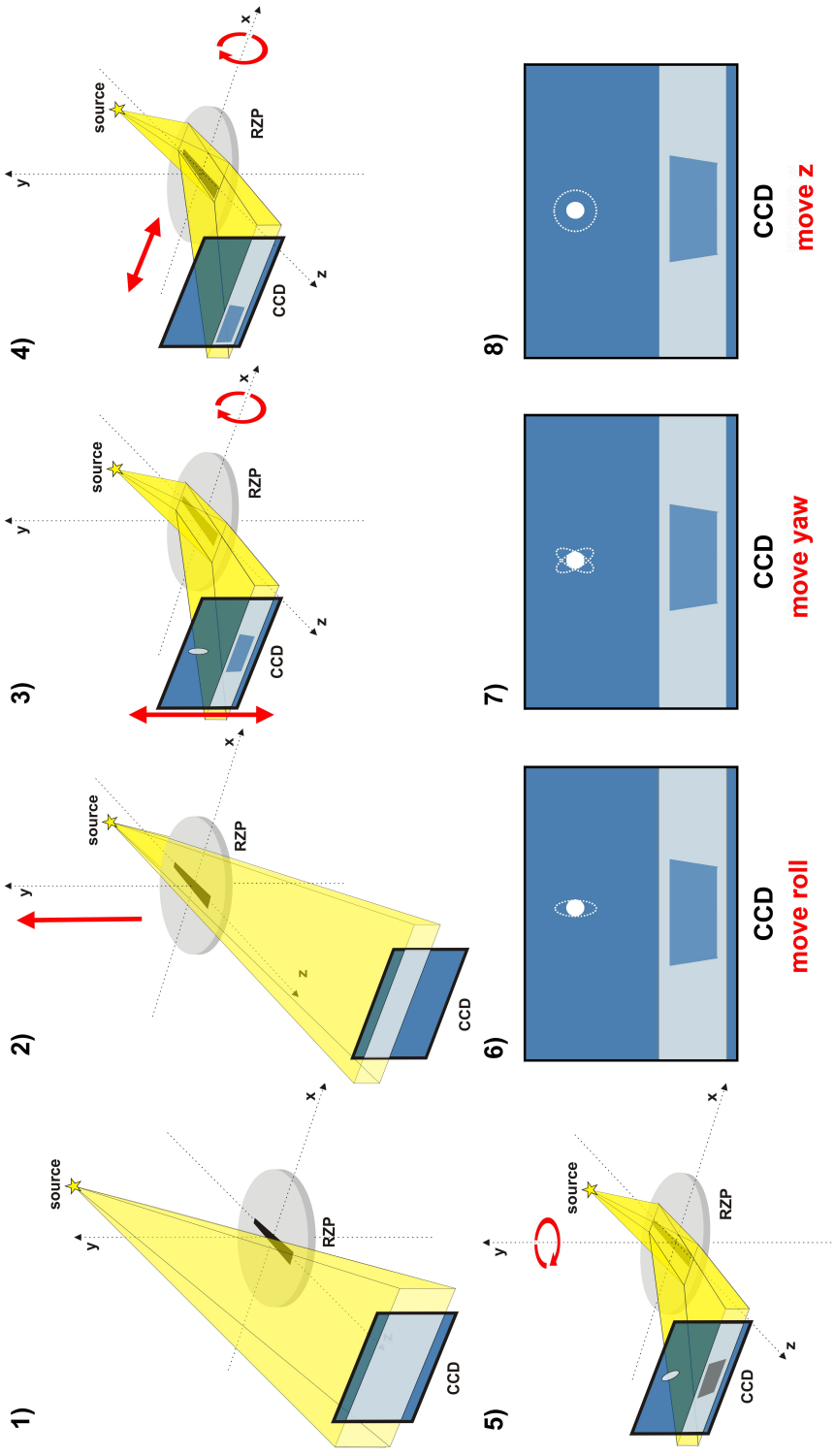

Figure 5.7: Steps of the alignment process of a typical RZP. Steps 1 to 5 show the whole setup: source, RZP and CCD, while in steps 6 to 8 only the CCD images are shown. The beam (incoming as well as reflected) is illustrated in yellow, the coordinate movements corresponding to each step are indicated by red arrows or red text, respectively. On the CCD screen, light appears as white or brighter blue tones. In steps 6 to 8, the shapes of the focal spot changed by the coordinate in question is depicted by dashed white contours. Please rotate by 90° clockwise.

5.2.4 Quality of the Focus

Figure 5.8 shows focal spot recordings at the ideal alignment for 17 different photon energies from 7.8 to 9 keV. Besides the typical vertical shift, the most obvious characteristic of the focal spot is its change in shape with the photon energy. While at lower photon energies the spot appears almost circular, there is a horizontal broadening towards higher energies as well as a small lateral "tail" on its right side in the lower-energy-half of the image series. This distortion is not caused by the RZP itself, but is a result of the source being distorted in the same manner. The secondary source created by the pinhole behind a focusing mirror is subdued to the inevitable mechanical tolerance of the beamline's double crystal monochromator. Unfortunately, during an energy scan, the beam that exits the monochromator moves in its lateral position, hitting the focusing mirror at different lateral positions.
Apart from the horizontal distortion, in vertical direction, the focal spot size varied from its smallest value, 3.4 ± 0.1 μm, at 8.4 keV, to 6.1 ± 0.1 μm at 9.0 keV and 8.8 ± 0.2 μm at 7.8 keV.

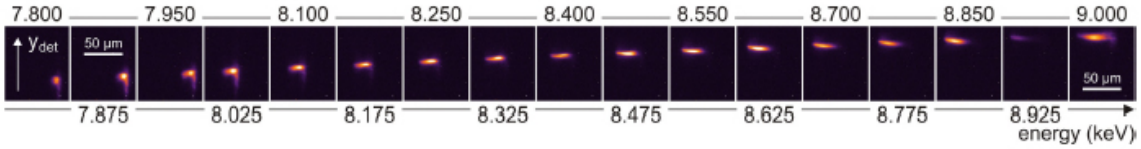

Figure 5.8: 131 (H) x 151 (V) pixel sections from the CCD images of the focal spot for different photon energies from 7.8 to 9 keV, showing the vertical shift as well as the changing shape of the focal spot [21].

5.2.5 Dispersive Properties

The 17 recorded CCD camera images were binned horizontally around the region of interest (0^{th} order and focal spot) and the resulting intensity curves were normalized (see figure 5.9). The graphs show a clear shift of the focal spot. As a quantity for the dispersive properties of the RZP, the resolving power $E/\Delta E$, with ΔE derived from the FWHM of the focal spot was calculated for each of the 17 CCD images and plotted as shown in figure 5.10. The resolving power follows a near-Lorentzian shape, with a full spectral range of 1.24 keV. The full spectral range is hereby calculated as the energy range, within which the resolving power is reduced by less than 20%.

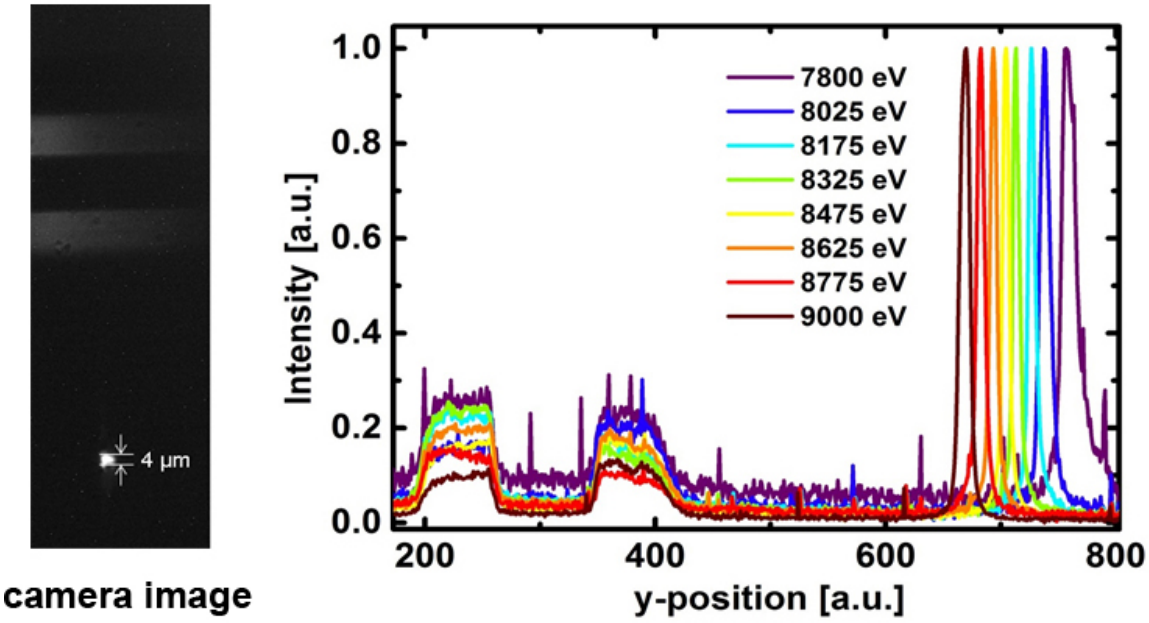

Figure 5.9: Vertical shift of the -1^{st} order focal spot with respect to the 0^{th} order: on the left, the camera image at the design energy is shown. The 0^{th} order shows as two wide horizontal stripes with the focal spot below. The 8 graphs on the right are normalised intensity distributions (horizontally binned pixel lines) at different photon energies.

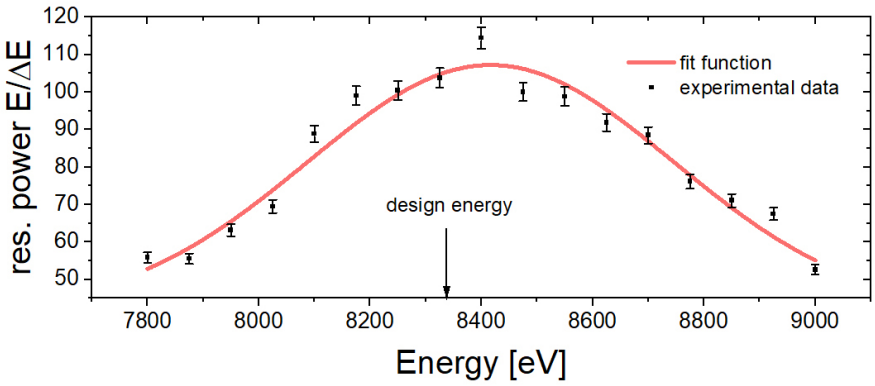

Figure 5.10: The resolving power of the RZP between 7.8 and 9.0 keV as derived from the vertical FWHM and position of the focal spot in the CCD images. Adapted from [21].

5.3 Characterization at APS

In a new experiment in 2014, at another experimental station at the Advanced Photon Source (APS) in Argonne, Illinois, the same RZP was characterized a second time. With a much higher photon flux, no focusing mirror was needed and the beamline offered the chance of illuminating the RZP with an almost parallel beam, undistorted by any other optical elements.

5.3.1 Setup of the Experiment

The setup at the 1-BM-beamline of the APS, a dipole beamline for the hard X-ray range, was composed very similar to the previous experiments at BESSY II, see figure 5.11. Due to the absence of any focusing mirror in the beamline, the RZP was illuminated with undistorted light coming directly from the dipole source. The RZP was set at 34 m distance to this source. As shown in a short calculation in the next section, this large distance, together with the very small size of the RZP itself, lead to the fact that the RZP was illuminated with a quasi parallel X-ray beam. To form a secondary source though, closer to the actual design parameters of the RZP, a slit prior to the monochromator, the so called white beam slit (WBS) was used. Unlike the BESSY II experiments, this WBS was located one meter further away from the RZP, at 11 m distance. The RZP was again mounted on a goniometer with 6 degrees

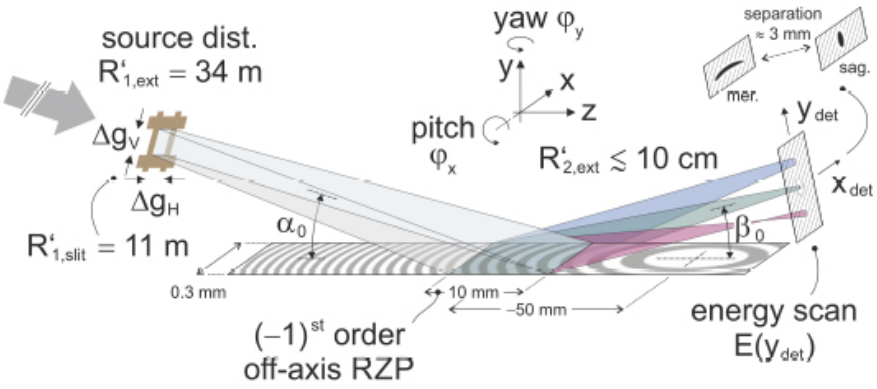

Figure 5.11: Schematic beamline setup at the APS [22]

of freedom so that the alignment procedure followed the same scheme as described above. To record the shape of the focal spot, two different apertures were installed at the RZP's exit arm length of 10 cm. At first, for a rough alignment, a CCD camera with a changeable optical magnification lens and hence a flexible effective pixel size, and secondly, for finer measurements, a knife-edge scan stage (see figure 5.12). Onto this stage, a round pinhole of about 30 μm diameter was mounted with beam blocking material surrounding it.

5.3.2 Beam Divergence

As mentioned above, the beam generated by the dipole source of the 1-BM beamline at the APS illuminated the RZP almost in a parallel beam. To actually estimate

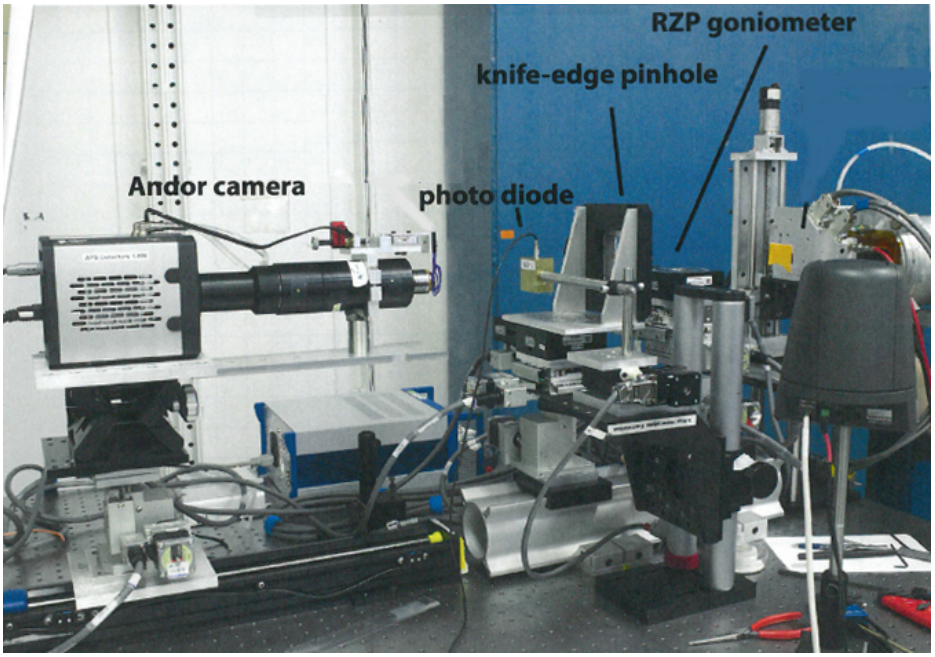

Figure 5.12: End station with RZP goniometer, CCD camera and knife-edge scanning stage

the beam divergence horizontally and vertically, the beam was cut by the WBS to illuminate only the RZP area. This cut was controlled by recoding an overview CCD-camera video featuring the focal spot as well as the specular reflection. As shown in figure 5.13, the beam was cut so that only a very small bright edge around the 0^{th} order shadow appeared. The white beam slit then had a size of 120 μm (H) and 50 μm (V). With the most recent measurements of a source size of 200 μm (H) and 80 μm (V), and the size of the RZP (in vertical direction projected onto a plane perpendicular to the incoming beam due to the angle of incidence), 300 μm (H) and 52 μm (V), as well as the known distances between source and WBS (24 m) and WBS and RZP (11 m), the paths of the most divergent rays can be found as follows (illustrated in figure 5.14):

In horizontal direction, there are two possibilities. If the exact source size is taken into account (green rays), this leads to a slightly wrong RZP size (273 μm), which is actually impossible since its layout was set to 300 μm and the e-beam writing liability was proven many times. Alternatively (orange rays), the source actually had a slightly larger horizontal size of 256 μm, which lies within the tolerance of their measurements. In the latter case, the horizontal beam divergence could be calculated as

$$\Theta_H = 2 \cdot \arctan \frac{256\mu m + 120\mu m}{2 \cdot 23m} = 16.35\mu rad.$$

In vertical direction though, this calculation formula with the most divergent beams

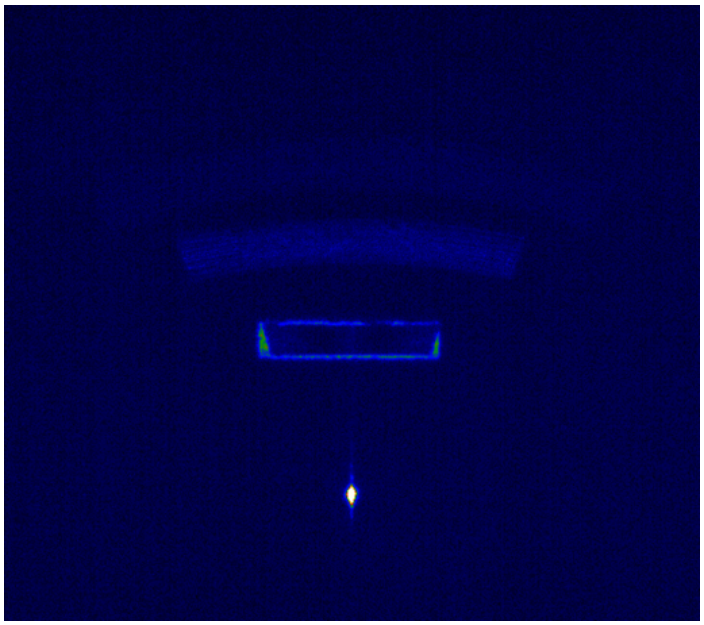

Figure 5.13: Focal spot (-1^{st} order), 0^{th} order and blurred positive orders with the incoming beam cut to the exact size of the RZP

crossing each other between the source and the WBS, poses a problem. The RZP projection size of 52 μm is only very slightly larger than the WBS size of 50 μm. So, with a source size of 80 μm, and the fact that the beam size has to be influenced by the WBS, the maximum divergence as calculated above, shown by orange rays in the figure, would result in a much too large RZP size of 112 μm. Therefore, the beam divergence in vertical direction must be very low, with the most divergent rays following the blue ray paths. With the given WBS and RZP sizes, this results in

$$\Theta_H = 2 \cdot \arctan \frac{52\mu m - 50\mu m}{2 \cdot 11m} = 0.2\mu rad.$$

In both directions, the results correspond well with the expectations, since dipole sources have a much higher divergence in horizontal than in vertical direction and the RZP's are is so very small compared to its distance to the source and WBS. According to [23], a hard X-ray beam is quasi parallel below a divergence of 1 $mrad$, so that within this experiment, the incoming beam can be seen as parallel.

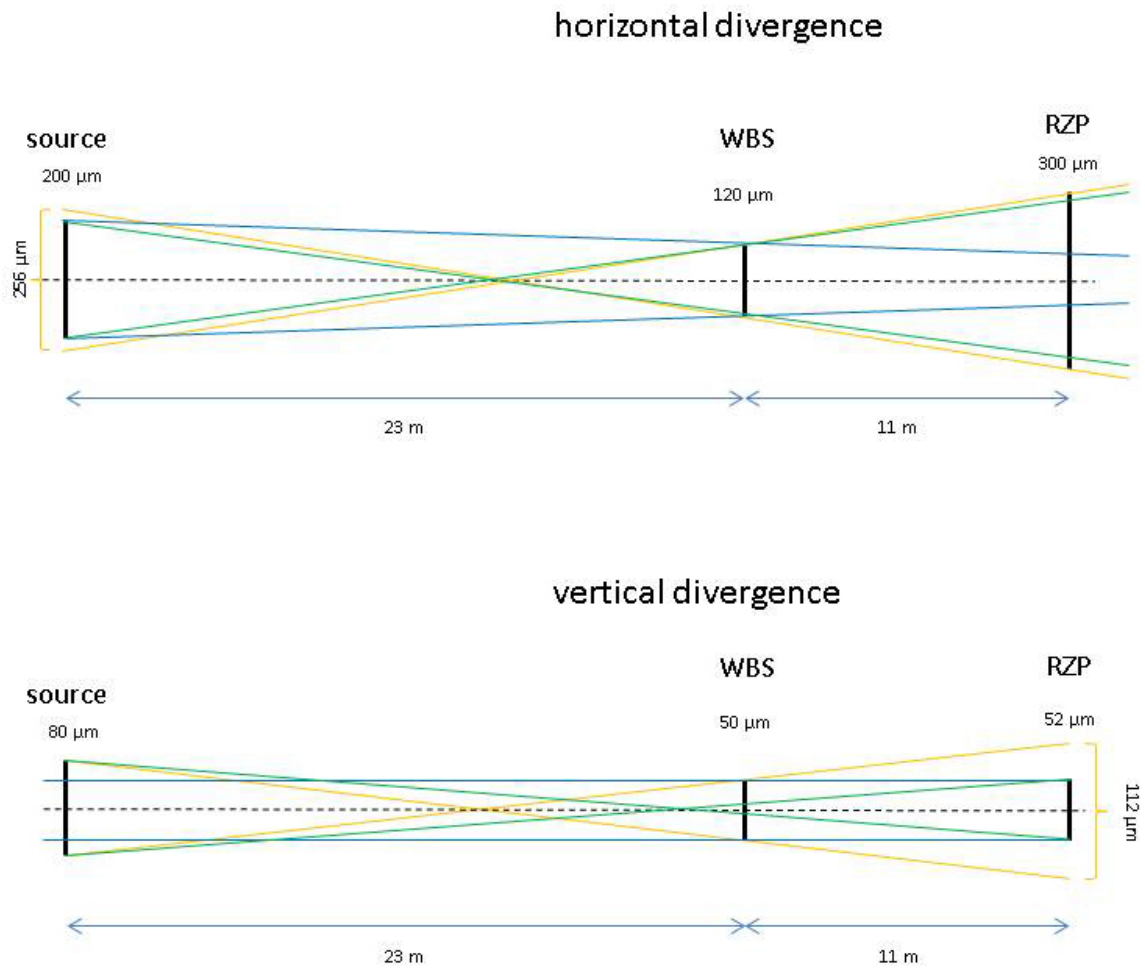

Figure 5.14: Scheme for the calculation of the beam divergence at the 1-BM beamline of the APS illuminating the RZP

5.3.3 Dispersive Properties

To analyse the dispersive properties of the RZP and compare the results with our previous experiments, a series of focal spots at different energies was recorded again and their FWHM as well as their vertical shift was determined. Unlike the BESSY II experiments though, the focal spots were measured with a more precise method, a knife-edge technique with a 30 μm pinhole mounted on a piezo stage. With a diode behind the stage, the amount of light coming through the pinhole was recorded. Due to inevitable slight shifts in the beam position in horizontal as well as in vertical direction caused by the monochromator, after each energy change, the horizontal position of the pinhole had to be readjusted. The diode current was then plotted over the vertical position of the pinhole and the resulting curve was derived. Figure 5.15 shows five selected derivatives of these scan measurements of a series of 15 vertical scans at

equidistant energy steps in an interval from 7.6 eV to 9.0 eV. The averaged FWHM of both peaks in these derivatives give the values of the corresponding vertical focal size. The focal sizes combined with the vertical position yield the next figure (5.16), the graph for the resolving power as described above in the previous experiment analysis.

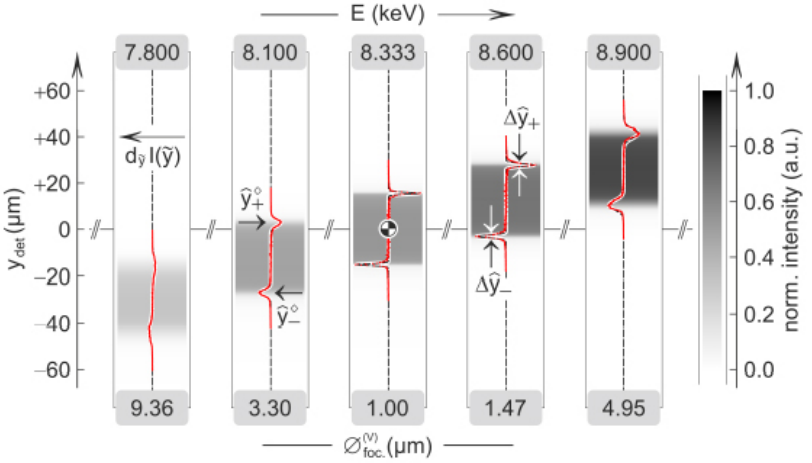

Figure 5.15: Selected vertical pinhole edge scan measurements of the full series between 7.6 keV and 9.0 keV. The 1D intensity distribution is normalized and displayed on a gray scale and its numerical derivative is shown in red. The spatial resolution is listed below [22].

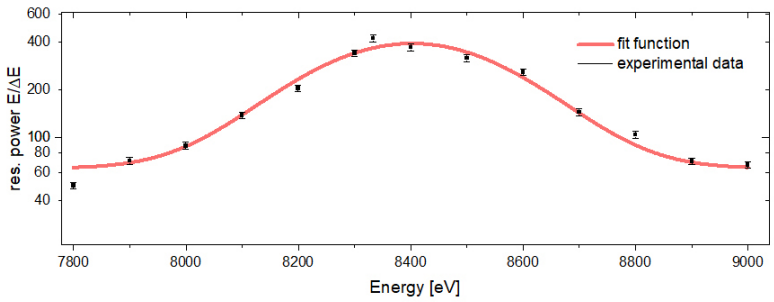

Figure 5.16: Resolving power as evaluated from the pinhole edge scans. The experimental results are compared with the fit function. Adapted from [22].

5.3.4 Size of the Focus

Due to the parallel incidence, the RZP's design parameters are not exactly fulfilled. Even though the beam quality was excellent, this caused a slight astigmatism, meaning a separation between the sagittal and meridional focal plane. Consequently, it was impossible to minimize the focal size in both directions at the same time. After finding the best compromise in the focal size for both directions with the beam cut to the

RZP size, the beam size was further reduced. In four steps, independently for each direction, the slit was closed down to an opening size of 10 μm, while leaving the other direction open. The focal size was then determined via the pinhole-knife-edge scan technique mentioned above. Figure 5.17 shows the results for both directions including ray tracing simulations for comparison. The tendency of a smaller focal size with a smaller source size is clear, even though the fitting curve as well as the simulated curves do not show a linear behavior. The focal spot size decreasing also confirms the fact that now the WBS must be seen as secondary source, even though the beam is nearly parallel. Starting with a focal size of 1.45 $\pm$ 0.73 μm (H) and 1.50 $\pm$ 0.75 μm (V), finally, at slit sizes of 10 μm, the focal spot could be reduced to 0.85 $\pm$ 0.42 μm (H) and 1.29 $\pm$ 0.64 μm (V).

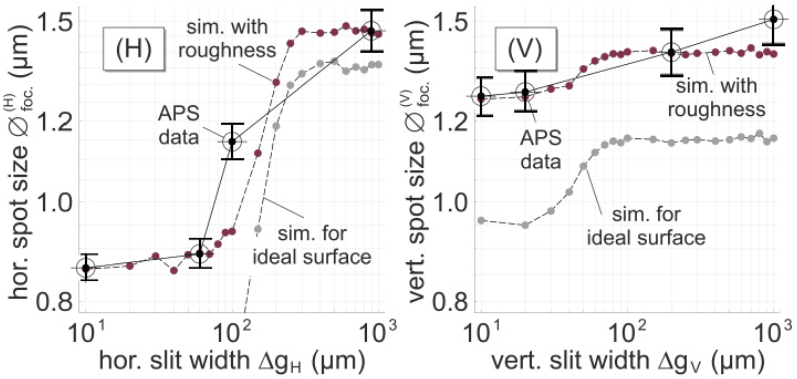

Figure 5.17: Decreasing of the white beam slit size and its influence on the focal spot size; in vertical direction (left) and horizontal direction (right) [22].

5.4 Errors of the Resolving Power and Focal Sizes

The resolving power $E/\Delta E$ at a photon energy E is calculated from the dispersion (Energy interval over the vertical shift in μm multiplied by the focal size at that energy. By error propagation the error of the result is the square root of the sum of the squares of each contributing parameter. The focal sizes are derived from the FWHM of the focal peaks in the line projections of the CCD images (count values in each pixel of the focal spot). At the HZB, the monochromator's mechanical error was determined as around 0.1%. The error of the vertical shift was estimated as around 2% and the error of the FWHM of the spots around 2% as well. This results in an overall error of roughly 3% for the resolving power at the HZB as shown in figure 5.10. At the APS, the asymmetrical properties of the focal spot due to the slight

astigmatism of the RZP played a larger role, so that the resolving power was given an estimated error of 5% (see figure 5.16). For the focal sizes, the calculation was done with the software Origin again, yielding an error of 2% at the HZB and 5% at the APS.

5.5 Time Elongation

A big technical advantage of a hard X-ray RZP is the very small elongation of any beam pulse that passes it. Due to its small size, the time difference between the first and the last ray hitting the surface of the RZP is smaller than a femtosecond. It can be estimated by the number of Fresnel periods that are included in the RZP area. Each of those periods causes a time elongation of

$$\Delta\tau = \frac{\lambda}{c} = \frac{1.5 \cdot 10^{-10} m}{3 \cdot 10^{8} \frac{m}{s}} = 5 \cdot 10^{-19} s. \tag{5.1}$$

With 700 periods along the optical axis of the RZP, this sums up to a total time elongation of

$$700 \cdot 5 \cdot 10^{-19} s = 0.35 fs.$$

6 Characterization in Soft X-rays

In addition to the hard X-ray RZP spectrometer, a soft X-ray spectrometer was designed and tested within the framework of this thesis. Its experimental purpose is different from the hard X-ray spectrometer. While for the hard X-rays the goal was to focus the beam to a minimum size while dispersing the incoming photon energies with a high resolution, the main function of the soft X-ray spectrometer is to yield a very high photon throughput. In the chemical experiment for which this spectrometer was developed, different metallo-enzyme complexes related to the photo system II (PSII) complex were studied. The PSII complex is a part of the natural photo synthesis process as found in plants and contains four manganese atoms that are oxidized in four different states throughout the photo synthesis. As the complex molecule is diluted in a water environment, the Manganese L-edge X-ray fluorescence signal of interest at 640 eV is usually overlayed by the close-by Oxygen K-alpha contribution at 525 eV. To separate these two signals while yielding a high photon throughput for Mn, the RZP spectrometer structure was optimized for a high-resolution spectral region around the Mn-signal and a maximum photon yield for Mn.

6.1 Experimental Setup and Spectrometer Design

The experiment was set at the Linac Coherent Light Source (LCLS), a free electron laser facility located at the Stanford Linear Accelerator Center (SLAC) in Menlo Park, USA. The free electron laser's soft X-ray materials science (SXR) beamline provides a very intense soft X-ray beam that excites the fluorescence signals. The sample substances are dissolved in water at very low concentrations and injected from above into a vacuum chamber at the beamline's end station. The liquid entering the vacuum from a capillary forms a thin jet (see figure 6.1) which is hit perpendicularly by the horizontal X-ray beam. The fluorescence is then emitted in all directions, so some part of it is collected by the RZP and focused onto a CCD sensor chip. The RZP's entrance arm was kept short (90 mm), to collect as much of the signal as possible. The exit arm is longer (400 mm), to ensure a large separation between the two close-by signals of Mn and O. The resulting fact that here the source is slightly magnified does not restrain the goal of the experiment, since the X-ray beam (and with it the source point of the fluorescence) is kept at a very small size anyway.

The arm lengths were optimized for the best compromise between a good separation of the two signals and a large meridional acceptance angle. The RZP is held in a fixed case constructed to keep its position fixed with respect to the CCD camera at the right exit arm length (see figure 6.2). At the front end of the case, which faces the liquid jet, a small aperture hole of around 3 (H) x 2 (V) mm^2 ensures that in the right adjustment. Only the RZP area is illuminated, avoiding unnecessary light scatter. The distance between the front edge of the RZP (which is 80 mm long) and the liquid jet is just 50 mm, so a thin aluminum filter in front of the aperture shields away any visible light from the chamber and any spraying material from the jet. A vacuum valve protects the sensitive CCD sensor from damage during venting.

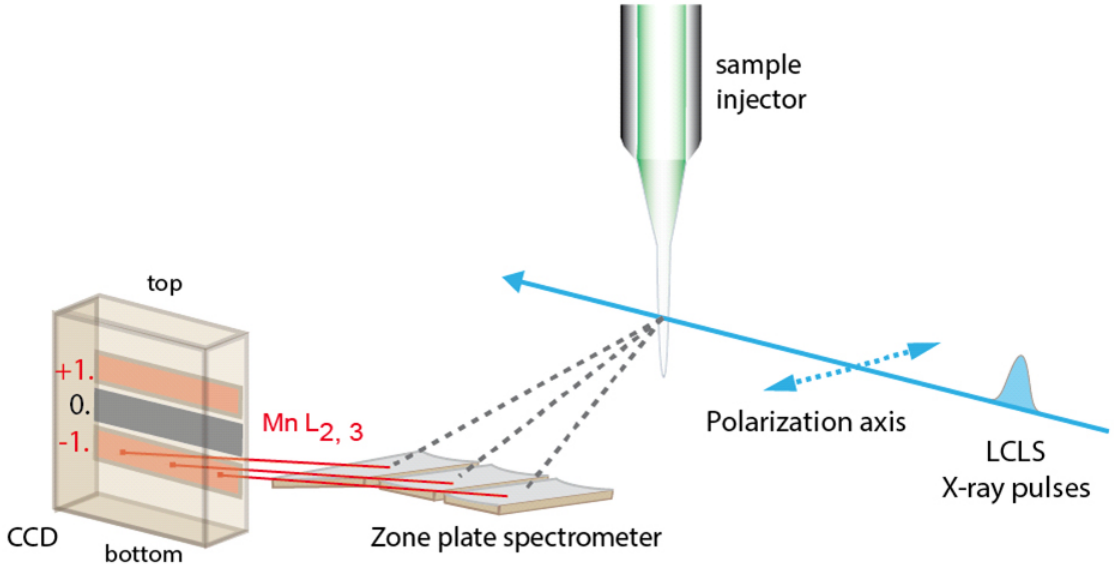

Figure 6.1: Scheme of the spectrometer setup: the incoming X-ray laser beam is shot onto the liquid jet sample which then emits the X-ray fluorescence. The fluorescence X-rays hitting the area of the RZP structures are then focused onto the CCD camera chip [24].

6.2 Structure Optimization

To find the ideal RZP structure that would best fit this experiment, five different structure types were designed and tested in a separate row of experiments at BESSY II beamlines, prior to the actual experiment.

The spectrometer layout as described above was designed with fixed entrance and exit arm lengths. Together with the angle of incidence, the design energy and the distance between the Fresnel zone center (FZC) and the center of the written RZP area, these

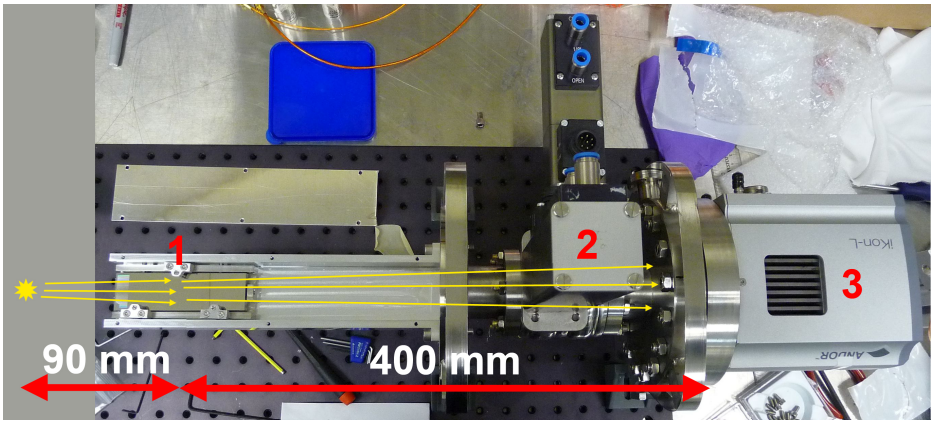

Figure 6.2: Top view of the spectrometer. At 90 mm from the source (yellow spot on the left), the RZP (1) collects the fluorescence light and focuses it onto the CCD camera chip (3) at 400 mm distance. Between RZP and CCD there is a valve (2) to protect the CCD from contaminations during venting.

parameters were optimized in the typical procedure as described in section 5.2.3. So, for the maximum meridional acceptance angle and the highest grating efficiency along the optical axis of the RZP, these parameters were unchangeable. The simplest structure, a normal elliptical single RZP (see type 1 in figure 6.4), is limited in its width due to the fabrication limit. This width is just about a third of the useable total opening angle matching the width of the CCD detector. So in sagittal direction, there was a certain degree of freedom to fill more of the substrate with RZP structures and collect more light onto the CCD.

The first approach to fill the side parts was to simply duplicate the structure two times and create a three-channel RZP array. Here of course, the parameters of the outer two RZPs must be changed a little according to their position to ensure that their focal point appears exactly in the CCD plane (see section 3.7.4). The structure and its resulting camera image are shown as type 2 in figure 6.4.

In a second approach, shown as type 3, the whole opening angle was filled with 40 smaller channels. The smaller channels have the advantage that the smallest structures are larger. The result is an array of focal points along the focal line in the CCD image.

The third and fourth layout (type 4 and 5) both result in focal lines instead of focal points. The first layout was a continuous array and the second one an astigmatic RZP, as both are described in section 3.8.

All in all, these five structures were compared with respect to two main aspects: the duration of the adjustment procedure (in the actual experiment every second counts) and their efficiency (photon throughput) as described in the following.

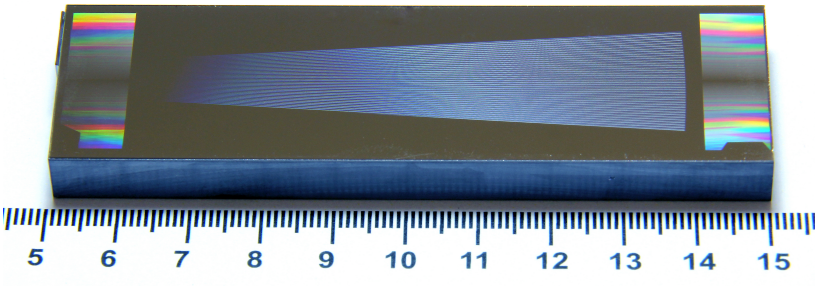

Figure 6.3: One of the RZP arrays, with 40 channels and adjustment RZPs in the front and back for adjustment with visible light.

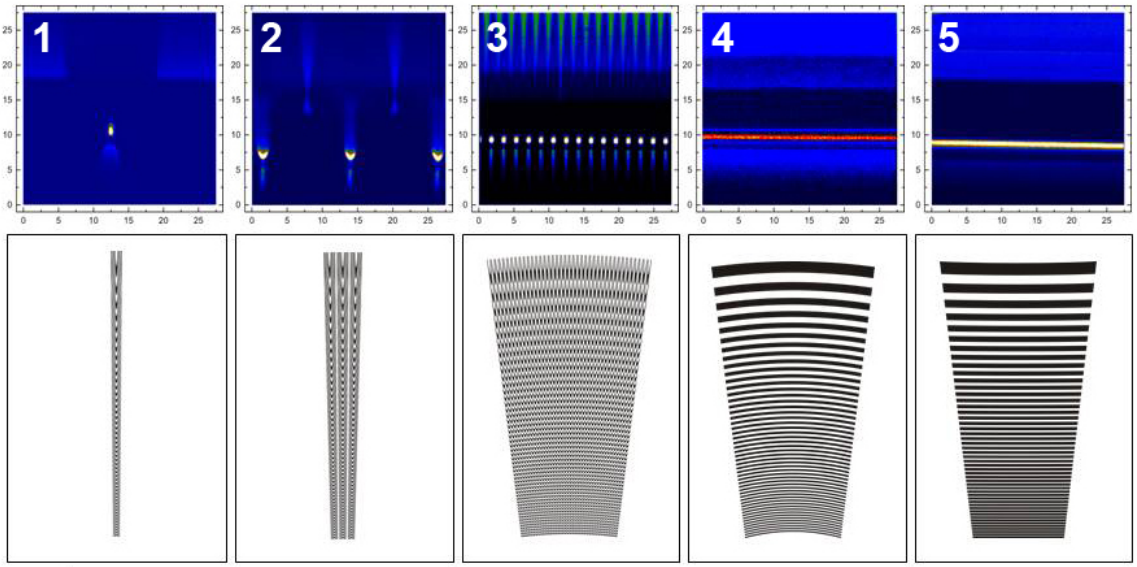

Figure 6.4: 5 different structure types for a low-signal RZP spectrometer: 1) the prototype, a single elliptical RZP, 2) 3 elliptical RZPs, 3) array of 40 elliptical RZPs, 4) continuous array, 5) astigmatic RZP

6.2.1 Alignment procedures

As described above in the general alignment procedure, there are two features in the CCD image which can be used for the alignment: the 0^{th} order and the focal spot. Due to the grazing incidence, the 0^{th} order of diffraction is usually detected together with the focal image (see figure 2.9). In single RZP spectrometers which are limited to small lateral dimensions, the 0^{th} order is (at least laterally) surrounded by the reflection of the plain substrate. Therefore, the lateral edges of the RZP are visible. This helps adjust the very sensitive yaw angle. However, RZP arrays have much larger lateral dimensions with several RZPs side by side. If the array's structure is written with small gaps of unstructured substrate between the channels, these gaps appear as

vertical stripes in the 0^{th} order. These can easily be used to determine yaw and z. If all stripes are tilted in the same direction (see figure 6.5), this means that yaw is wrong. If they are tilted in a tapered way, z is wrong. Of course, these two misalignments can coincide and the effects will superimpose.

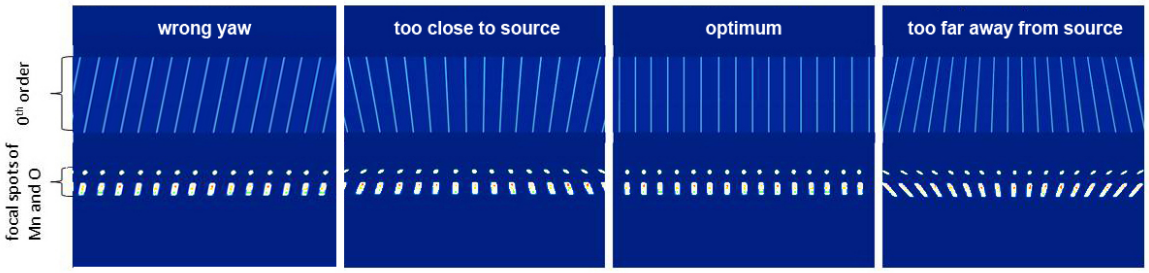

Figure 6.5: Scheme of shape and slope of focal spots and gap lines in the 0^{th} order of a monochromatic RZP array depending on the distance between source and RZP (z).

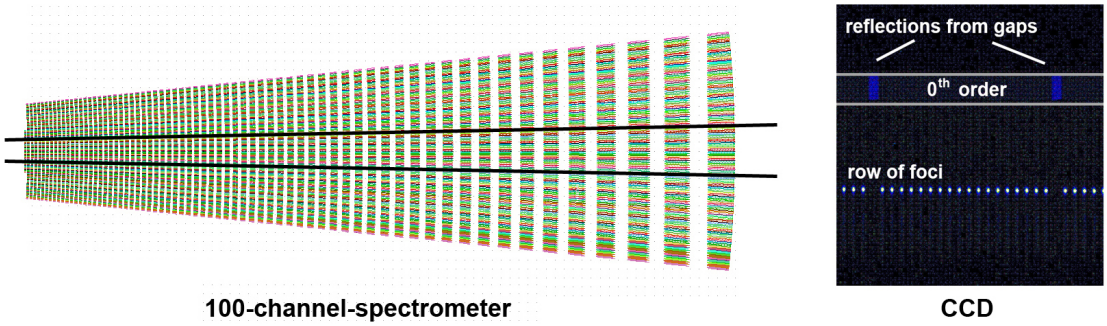

Figure 6.6: On the left: scheme of monochromatic RZP array with 100 channels working in -1^{st} order. Note that for illustration, the Fresnel zones are much larger than in reality. Around the lateral center of the structure, two channels are left out (black lines) as alignment indication feature. On the right: the corresponding CCD image (see soft X-ray characterization, section 6.2). The two gaps in the structure cause two brighter (here blue) vertical stripes in the otherwise continuously dark 0^{th} order. Consequently, two focal spots in the -1^{st} order below are missing. The CCD covers only 25 of the 98 focal spots because the full spectrometer was made for a maximum detector width of 10 cm, while this CCD is 2.7 only cm wide.

If the array structure is written without any gaps between the channels, the RZP edges will be invisible. On the other hand, the smaller the channels are, the smaller the photon throughput will be. A gap of 10% the lateral size of the channels means a photon loss of 10%. Whereas in multi-channel spectrometers at least the shape of the focal points can still yield enough information about the yaw-angle, the problem worsens for continuous structures. Here, the focus is for example line-shaped and any change in yaw will only blur the line.

To solve these problems, practical experience shows that the best compromise between a large illuminated area and sufficient alignment properties is to leave out only two small gaps along the optical axis of the structure as shown in figure 6.6. In the resulting CCD image, the gaps appear as two brighter vertical stripes in the 0^{th} order area (see figure 6.6, right side).
The orientation of these two stripes can be used to adjust the yaw angle as well as z in the same manner as for the array of 40 channels. In the ideal RZP position, they appear parallel to each other and orthogonal to the focal line (row of focal spots). If yaw is misaligned, they will both be tilted in the same direction (see figure 6.6, lower part). If z is misaligned, they will be tilted in opposite directions.

6.2.2 Efficiency Measurements

The efficiencies of the different RZP types were measured over the time of their development with two different reflectometer types at BESSY II beamlines. Since the first reflectometer, which was available until 2015, had no possibility of adjusting the RZP's azimuthal angle (rotation around the surface normal), the first row of measurements was limited to points along the optical axis of the RZP structures. As the efficiency of an RZP changes with the angle of incidence and the local grating period though, a row of three points along this axis, one in the center of the RZP structure, and two at ± 2 cm from the center were measured. Figure 6.7 shows the changes in the incident angles that were necessary to keep the focal spot of the RZP at the same detector position for all measurements. In each point, the photon throughput of the RZP (with respect to the direct beam) was measured for 11 different photon energies around the design energy of 640 eV. In figure 6.8, two of these energy scans are shown for different RZP types. The first one is the prototype, the single RZP, focusing in a point and the second one a continuous array focusing in a line. To get an idea of the overall distribution of the light into the different diffraction orders, there are three curves in each graph, one for the -1^{st} order (the focus, shown in black), one for the specular reflection (0^{th} order, shown in red) and the unfocused 1^{st} order, shown in blue. The two graphs look similar, but the maximum efficiency of the single RZP structure is higher (up to roughly 24 % at 700 eV) than the one for the continuous array (roughly 20 % at 640 eV). The energy of the maximum is connected to the profile depth of the RZP. The ideal profile depth was calculated as a compromise for the whole RZP area, though actually it is slightly different depending on the local grating

period. The height of the maximum is connected to the surface roughness, so it can be concluded that the surface of the single RZP has a lower roughness than the one of the continuous array. But, as these two measurement points are just examples out of three for each RZP, for the final calculation of the whole efficiency, all of them have to be considered. They must be weighted with an intensity factor for the incoming light, since the distance to the source in the actual experiment at the SLAC is different in all three points. The results of this calculation for all 3 points of all RZP types and the total efficiency are summarized in figure 6.9. The total efficiencies vary between 13.3 ± 0.2 % and 20.3 ± 0.2 %. Unlike the exemplary measurement points mentioned above, in the overall efficiency, the continuous array yields better results than the single RZP. It also seems that the line focusing RZPs both are more efficient than the elliptical RZPs, which would support the theory that larger structures are more efficient and are less influenced by fabrication irregularities.
Measurements at the second type of reflectometer yielded contradictory results. Since the reflectometer has a tripod stage for samples which can be moved in many degrees of freedom including the azimuthal angle, a more realistic analysis of the lateral parts of the elliptical RZP could be done. In these lateral parts, the local grating period is small, but the incoming beam does not hit the Fresnel zones perpendicularly. In the outer parts of an elliptical RZP, the grating lines run almost parallel to the incoming beam, so that the actual effective grating period is much larger than the groove and line period. The results of efficiency simulations as done with REFLEC, which has no possibility of conical incidence, are no more accurate enough. Figure 6.10 shows the efficiency curves for different points along a line across the RZP's center, perpendicular to the optical axis (here coordinate x). The thin curves were measured without correcting the azimuthal angle and the thick curves were measured with this correction. It is clear that the further outside the measurement point, the lower the efficiency seems without the correction. With the correction, there is even a slight increase to the outer parts.

6.2.3 The Errors of the Efficiency Measurements

Over many years, the beam slit size and all geometrical parameters (that have fully automatic fine motor controls) of reflectometer at the HZB, such as angles and x-, y- an z-positions, were optimized to generate errors less than 0.1 %. With a precision like that, each efficiency measurement is done by first collecting the light (with a diode) from the incident beam directly and then collecting the light that is reflected

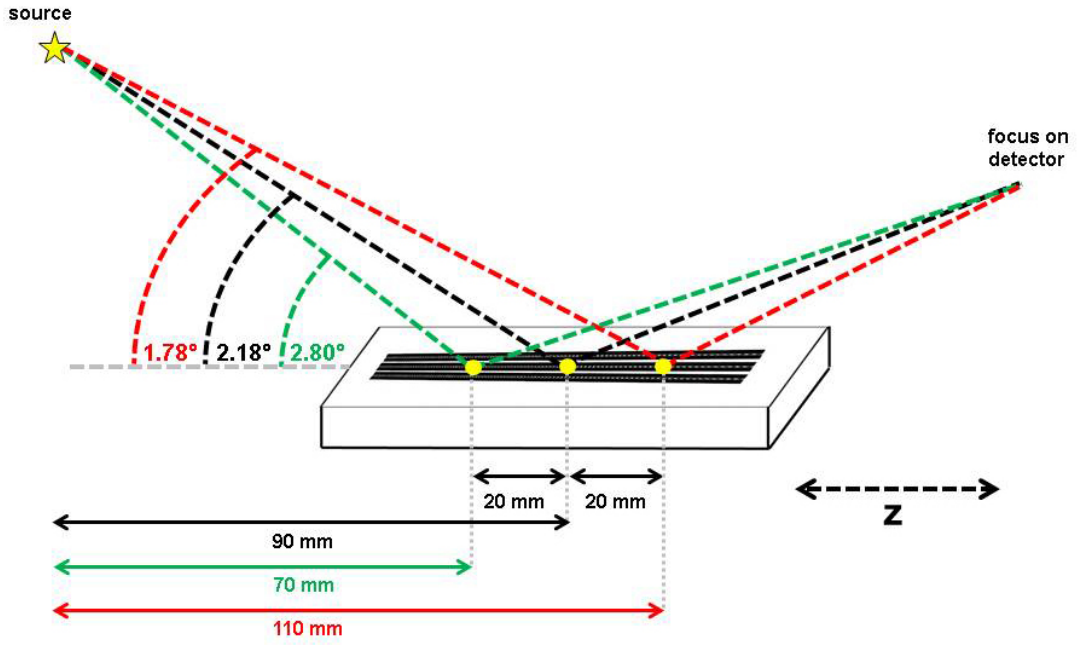

Figure 6.7: Efficiency measurement technique with 3 measurement points and adjusted incident angles

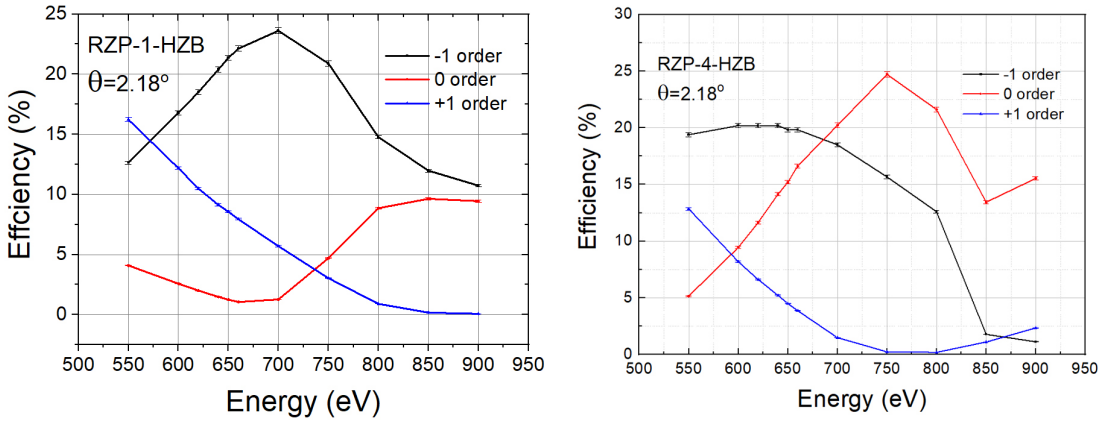

Figure 6.8: Efficiency energy scan on a) the prototype and b) the continuous array

by the RZP in its different orders at different photon energies while the collecting diode is moved along a range of exit angles (theta). The resulting curves usually have sharp peaks that are then integrated in the software Origin. This integration process includes a manual determination of the points between which the peak is integrated. For the measurements with the measuring points along the central axis of the RZP, the error that results from the uncertainty of determining these integration borders has to

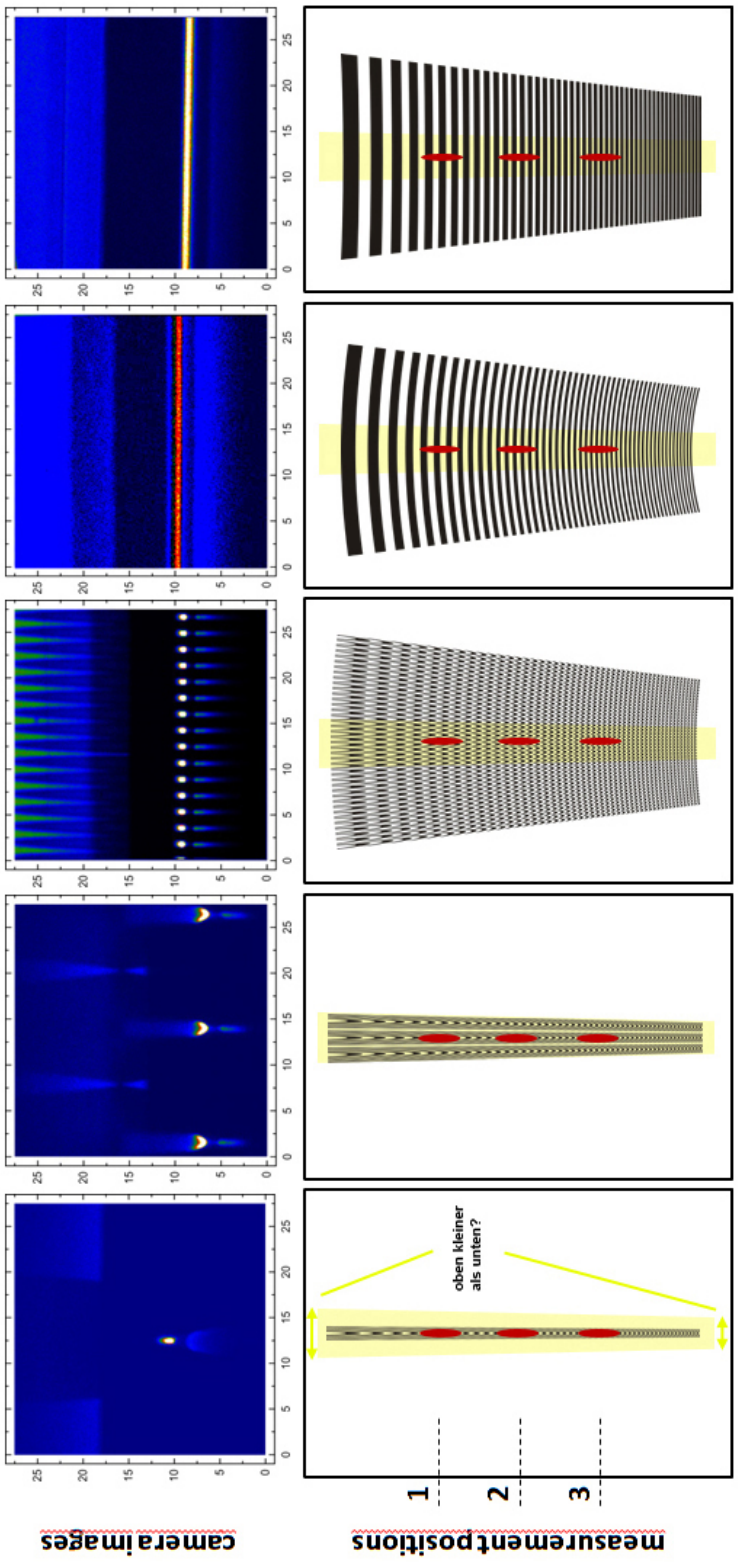

position/ substrate	1 RZP	3 RZPs	40 RZPs	continuous	astigmatic
1	22.8±0.2	21.3±0.2	25.2±0.3	28.8±0.3	22.5±0.2
2	20.4±0.2	17.9±0.2	17.6±0.2	20.2±0.2	21.5±0.2
3	6.3±0.1	4.6±0.1	7.6±0.1	13.0±0.1	10.65±0.1
total	15.4±0.2	13.3±0.2	15.4±0.2	20.3±0.2	18.0±0.2

Figure 6.9: Efficiency measurement results for the 5 different types of RZPs.

be estimated as a much higher and more significant contribution to the resulting error for each measurement value. With these assumptions, the error of the measurements of the central axis were estimated as no higher than 1% (see figure 6.8 and table in figure 6.9 and the measurements on the lateral areas no higher than 3% (see figure 6.10).

6.2.4 Final Choice

With all factors influencing the overall performance of the different types of RZPs, the easiness of the alignment of RZP arrays compared to line focusing structures, the higher efficiency of the larger zone widths and the fact that there is no loss of intensity in the outer parts of the elliptical RZPs, the final decision for an optimized RZP structure was a compromise between elliptical and continuous structures. An array with very small channels, overall 100, with two empty channels for a faster adjustment as described above was designed, fabricated and tested in the latest experiments at the SLAC. Due to the fact that there are many challenges during the experiment which need to be met at the same time, like making sure that the liquid jet runs smoothly or that the X-ray beam is stable, the need for a very fast adjustment slightly over weighted the need for the highest efficiency.

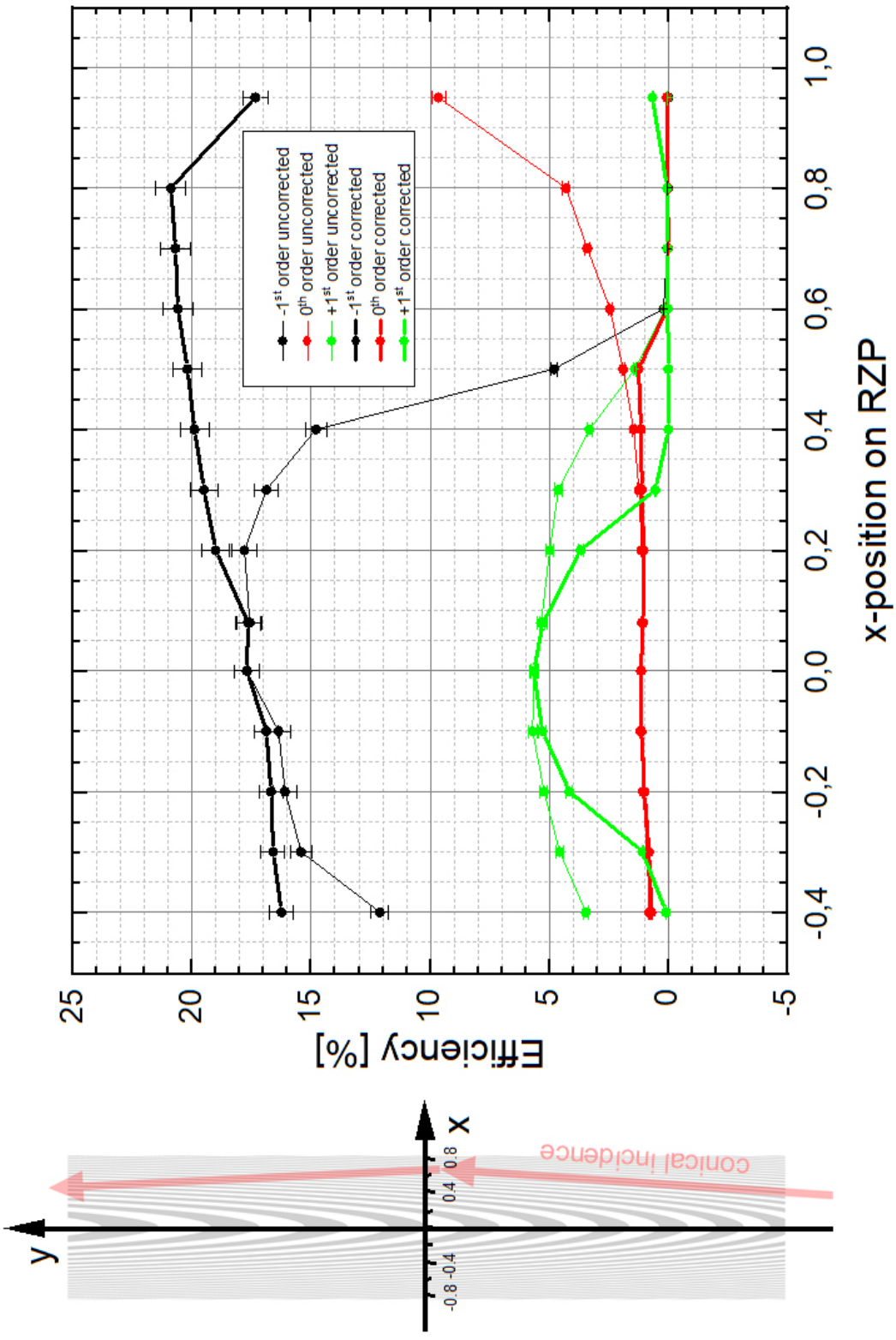

Figure 6.10: Efficiency measured in the lateral areas of a single RZP with adjusted azimuthal angle

Summary

In this thesis, two main application fields for off-axis reflection zone plates (RZPs) in X-ray optics were analyzed: as element for the monochromatization of soft and hard X-ray beams and as spectroscopy element for X-ray spectrometers with synchrotron radiation, free electron lasers, as well as laboratory sources such as laser plasma sources and high harmonic generators.

As a big step forward in the design process, a new calculation software was developed, using a modern mathematical description of an ellipse-plane intersection. This new approach reduces the data volume and calculation time to a minimum, while ensuring a high accuracy of the structures and opens many possibilities for the design of multi-channel parallel spectrometers for monochromatic and polychromatic radiation.

The spectroscopic properties of off-axis RZPs were systematically investigated in the hard X-ray range. The spatial resolution was found to be better than 2 μm at 8.3 keV with a diffraction efficiency of 17.5 %. The experimentally tested spectroscopic arrangement showed a resolving power ($\lambda/\Delta\lambda$) up to 400 in an energy range of 1000 eV around the central energy. This experiment indicates a possibility of absorption spectroscopy on transition metals in the energy range below 10 keV. Simultaneously, a time elongation in the optical element was estimated as 0.35 fs, which would allow ultra-fast time resolved spectroscopy methods.

For the first time in the soft X-ray range, within the framework of this thesis, multi-channel RZPs for an ultra-sensitive parallel X-ray spectrometer were realized. Through this development, the spectrometer could be applied at the free electron laser source LCLS in Stanford (outside of this dissertation). The spectroscopy of highly diluted materials, metallo-enzyme complexes that contain manganese oxides, was performed. The new spectrometer has one order of magnitude better acceptance than conventional grating spectrometers. The results of these measurements are not mentioned in this thesis.

The developed design model was applied for the realization of two types of new laboratory source spectrometers based on RZPs: a parallel spectrometer for a scanning electron microscope and a single-channel spectrometer for a laser-plasma X-ray source.

Kurzzusammenfassung

In dieser Arbeit werden die zwei Haupt-Anwendungsgebiete von Reflektionszonenplatten (RZPs) in der Röntgenoptik analysiert: als optisches Element zur Monochromatisierung von weicher und harter Röntgenstrahlung und als Element von Röntgenspektrometern wie Laser-Plasma-Quellen und High Harmonic Generators.

Der wichtigste Aspekt der Weiterentwicklung bestand darin, den Design-Prozess von RZPs durch eine neue Software, die auf einem modernen mathematischen Modell des Schnitts zwischen einem Ellipsoiden und einer Ebene basiert, zu erleichtern und zu beschleunigen. Dies reduziert die Datenmenge und die Rechenzeit auf ein Minimum, während gleichzeitig eine sehr hohe Strukturgenauigkeit erzielt werden kann. Somit wurden neue Möglichkeiten für die Realisierung von Multi-Channel Spektrometern geschaffen, sowohl für monochromatische als auch für polychromatische Strahlung.

Die spektroskopischen Eigenschaften von Off-Axis RZPs wurden im Bereich der harten Röntgenstrahlung systematisch untersucht. Dabei wurde eine örtliche Auflösung von unter 2 μm bei 8.3 keV mit einer Effizienz von 17.5 % erreicht. Der experimentelle Aufbau ermöglichte eine Energieauflöung von ($\lambda/\Delta\lambda$) bis zu 400 in einem Energiebereich von 1000 eV um die Designenergie der RZP. Dadurch wurde eine neue Möglichkeit für Absorptionsspektroskopie an Übergangsmetallen unterhalb von 10 keV geschaffen. Ein weiterer Vorteil von RZPs in diesem Bereich ist die geringe zeitliche Streckung ultra-kurzer Lichtimpulse. Sie liegt in diesem Fall unterhalb von 0.35 fs und ermöglicht zeitlich hochaufgelöste Röntgenspektroskopie.

Darüber hinaus wurden im Rahmen der vorliegenden Doktorarbeit zum ersten Mal im Bereich der weichen Röntgenstrahlung Multi-Channel RZPs für ein ultra-sensitives Parallelspektrometer entwickelt. Durch diese Entwicklung konnte das Spektrometer am Freie-Elektronen-Laser (außerhalb dieser Dissertation) in Stanford getestet werden. Metallo-Enzym-Komplexe in einer sehr verdünnten Lösung, die Mangan-Oxide enthalten, wurden mit dieser Methode untersucht. Durch das neue Spektrometer konnte die Akzeptanz um eine Größenordnung erhöht werden. Die Ergebnisse dieser Messungen sind nicht Gegenstand der vorliegenden Dissertation.

Nach dem in dieser Arbeit entwickelten Design-Prozess wurden zwei Typen von Röntgenspektrometern realisiert: zum einen Parallel-Spektrometer zur Anwendung an Rasterelektronenmikroskopen und ein Ein-Kanal-Spektrometer für eine Laser-Plasma-Quelle.

Publication List

The results of the research done within the framework of this thesis are published in:

journal papers

1. C. Braig, H. Loechel, A. Firsov, M. Brzhezinskaya, A. Hafner, J. Rehanek, M. Wojcik, A. Macrander, L. Assoufid and A. Erko, *Hard x-ray spectroscopy and imaging by a reflection zone plate in the presence of astigmatism*, Optics Letters (2016), **vol. 41**, 29- 32

2. H. Löchel, C. Braig, M. Brzhezinskaya, F. Siewert, P. Baumgaertel, A. Firsov and A. Erko, *Femtosecond high-resolution hard X-ray spectroscopy using reflection zone plates*, Optics Express (2015), **vol. 23**, 8788-8799

3. C. Braig, H. Löchel, R. Mitzner, W. Quevedo, P. Loukas, M. Kubin, C. Weniger, A. Firsov, J. Rehanek, M. Brzhezinskaya, Ph. Wernet, A. Foehlisch, A. Erko, *Design and optimization of a parallel spectrometer for ultra-fast X-ray science*, Optics Express (2014), **vol. 22**, 12583-12602

4. I. Mantouvalou, K. Witte, W. Martyanov, A. Jonas, D. Groetzsch, C. Streeck, H. Loechel, I. Rudolph, A. Erko, H. Stiel and B. Kanngiesser, *Single shot near edge x-ray absorption fine structure spectroscopy in the laboratory*, Applied Physics Letters (2016), **vol. 108(20)**, 201106

5. A. Hafner, L. Anklamm, A. Firsov, A. Firsov, H. Loechel, A. Sokolov, R. Gubzhokov, and A. Erko, *Reflection zone plate wavelength-dispersive spectrometer for ultra-light elements measurements*, Optics Express (2015), **vol. 23(23)**, 29476-29483

conference contributions

1. A. Firsov, M. Brzhezinskaya, H. Loechel, F. Siewert and A. Erko, *The impact of novel 3D diffraction optics development*, Proc. of SPIE (2013), **vol. 8777**, 877713-1

2. J. Rehanek, F. Schaefers, H. Loechel, A. Firsov, J. Grünert, W. Freund, C. Ozkan, S. Molodtsov and A. Erko, *A case study of novel X-ray Optics for FEL sources*, Journal of Physics: Conference Series (2013), **vol. 425**, 052013

3. H Loechel, M Brzhezinskaya, A Firsov, J Rehanek and A Erko, *Reflection zone plates for 2D focusing and spectroscopy of hard X-rays*, Journal of Physics: Conference Series (2013), **vol. 425**, 052025

With the developed software and optimization methods as well as the alignment procedures and the knowledge gained from the experiments conducted in this work, RZP structures can be applied in spectrometers for scanning electron microscopes, plasma sources or any synchrotron source.

Acknowledgement

I would like to express my deeply felt gratitude to my supervisor, Professor Dr. Alexei Erko, Director of the Institute for Nanometer Optics and Technology (INT) at the Helmholtz-Zentrum for Materials and Energy in Berlin for the opportunity to conduct research on this exciting field and for all his constructive and friendly advice and support.

I gratefully acknowledge my second supervisor, Professor Dr. Wolfgang Kuch, head of the working group "Spektroskopie and Spektromikroskopie an neuen magnetischen Materialien" at the "Institut fuer Experimentalphysik" of the Free University of Berlin for all his constructive and friendly advice and support during the genesis of my thesis.

My deep thanks go to Juergern Probst, PhD student at the INT for his incredible support in developing the RZP calculation software and introducing me to very advanced programming techniques and for the hours spent together in front of the pc.

My deep thanks go to Dr. Alexander Firsov, Senior Researcher at the INT for introducing me into the skills of electron beam lithography and fabrication technology for Reflection Zone Plates (RZP).

Another deep thank goes to Dr. Christoph Braig, Senior Researcher at the INT and member of the beam line design and raytracing group for very fruitful discussions and his valuable advice along the diffractive optics and RZP characteristics.

Outstanding thanks belong also to Frank Siewert, head of the measurement Group at INT for introducing me in the secrets of optical measurements for surfaces and for RZP.

I also want to acknowledge the work of the diploma students Analia Fernendez Herrero, Panagiotis Loukas, Aljosa Hafner and Simone Vadilongs for helping me to optimize RZP designs and for conducting some of the initial measurements.

Also, thanks to the entire RZP group of the INT for creating an almost familiar milieu, which was extremely comfortable and fruitful to work in. Namely, I would like to thank the following people:

Dr. Jens Rehanek, Dr. Friedmar Senf, Christian Weniger, Dr. Franz Schaefers, Andrey Sokolov, Peter Baumgaertel, Dr. Stefan Hendel, Ivo Rudolph, Dr. Ivo Zizak, Max Schoengen, Jana Buchheim, Silvio Künstner, Christoph Waberski and Johannes Wolf

Finally, I would like to say ”thank you” to all my family and friends, wherever they are, particularly my mom Tina and my dad Bernd, who supported me through my entire study, especially in the initial times. It is to them I dedicate this work.
Special thanks also to my partner Frank Merkel who presented me comfort, strength, and confidence for my work.

Bibliography

[1] V.V. Aristov, S.V. Gaponov, V.M. Genkin, Yu.A. Gorbatov, A.I. Erko, V.V. Martynov, L.A. Matveeva, N.N. Salashenko, and A.A. Fraerman. *Focusing Properties of Shaped Multilayer Mirrors. JETP Lett.*, 44(4):265–266, 1986.

[2] V.V. Aristov, A.A. Snigirev, Yu.A. Basov, and A.Yu. Nikulin. *X-ray Bragg optics. AIP Conf. Proc.*, 147:253, 1986.

[3] P. Chevallier, P. Dhez, A. Erko, A. Firsov, F. Legrand, and P. Populus. *X-Ray Microprobes. Nuclear Instruments and Methods in Physics Research*, B113:122–127, 1996.

[4] P. Chevallier, P. Dhez, F. Legrand, M. Idir, G. Soullie, A. Mirone, A. Erko, A. Snigirev, I. Snigireva, A. Suvorov, A. Freund, P. Engstroem, J. Als Nielsen, and G. Grübel. *First Test of the scanning X-Ray microprobe with Bragg-Fresnel multilayer lens at ESRF beamline. Nuclear Instruments and Methods in Physics Research*, A354:584–587, 1995.

[5] Ya. Faenov, S.A. Pikuz, A.I. Erko, B.A. Bryunetkin, V.M. Dyakin, G.V. Ivanenkov, A.R. Mingaleev, T.A. Pikuz, V.M. Romanova, and T.A. Shelkovenko. *High-Performance X-Ray Spectroscopic Devices for Plasma Micro-sources Investigations. Physica Scripta*, 50:333–338, 1994.

[6] T.Wilhein, D. Hambach, B. Niemann, M. Berglund, L. Rymell, and H. M. Hertz. *Off-axis reflection zone plate for quantitative soft x-ray source characterization. Appl. Phys. Lett.*, 71:190–192, 1997.

[7] A Erko, A Firsov, R Gubzhokov, A Bjeoumikhov, A Günther, N Langhoff, M. Bretschneider, Y. Höhn, and R. Wedell. *New parallel wavelength-dispersive spectrometer based on scanning electron microscope. Optics Express*, 22 (14):16897–16902, 2014.

[8] K. Holldack, J. Bahrdt, A. Balzer, U. Bovensiepen, M. Brzhezinskaya, A. Erko, A. Eschenlohr, R. Follath, A. Firsov, W. Frentrup, L. Le Guyader, T. Kachel, P. Kuske, R. Mitzner, R. Müller, N. Pontius, T. Quast, I. Radu, J.-S. Schmidt, C. Schüssler-Langeheine, M. Sperling, C. Stamm, C. Trabant, and A. Föhlisch.

FemtoSpeX: a versatile optical pump-soft X-ray probe facility with 100 fs X-ray pulses of variable polarization. J. Synchrotron Rad., 21:1090–1104, 2014.

[9] A.I. Erko, V.V.Aristov, and B.Vidal. *Diffraction X-Ray Optics.* IOP Publishing Ltd, 1996.

[10] P. Baumgärtel, M. Witt, J. Baensch, M. Fabariu, A. Erko, F. Schäfers, and H. Schirmacher. *RAY-UI: A Powerful and Extensible User Interface for RAY.* presentation at SRI, 2015.

[11] G. Weber. *X-Ray attenuation & absorption calculator.* http://web-docs.gsi.de/~stoe_exp/web_programs/x_ray_absorption/index.php. letzter Aufruf am 11.07.2015.

[12] A. Erko and Alexander Firsov. *Investigation of the properties of Bragg-Fresnel gratings. Proc. SPIE*, 5539:148–159, 2004.

[13] A.G. Michette and C.J. Buckley. *X-ray sience and Technology.* IOP Publishing Ltd, 1993.

[14] H. Löchel. *Reflektionszonenplatten für harte Röntgenstrahlung.* Diploma thesis, 2012.

[15] P. P. Klein. *On the Ellipsoid and Plane Intersection Equation. Applied Mathematics*, 3:1634–1640, 2004.

[16] Christoph Braig, Heike Löchel, Rolf Mitzner, Wilson Quevedo, Panagiotis Loukas, Markus Kubin, Christian Weniger, Alexander Firsov, Jens Rehanek, Maria Brzhezinskaya, Philippe Wernet, Alexander Föhlisch, and Alexei Erko. *Design and optimization of a parallel spectrometer for ultra-fast X-ray science. Optics Express*, 22:12583–12602, 2014.

[17] Jun Jiao. *Chapter 32 X-Ray Spectrometry: X-Ray Energy Dispersive Spectrometer (XEDS).* http://web.pdx.edu/~jiaoj/phy452/lect9_ph452-552%20-%202012.pdf. letzter Aufruf am 16.04.2015.

[18] Darrell Henry et al. *Wavelength-Dispersive X-Ray Spectroscopy (WDS).* http://serc.carleton.edu/research_education/geochemsheets/wds.html. letzter Aufruf am 16.04.2015.

[19] Bob Hafner. *Energy Dispersive Spectroscopy on the SEM: A Primer*. http://www.charfac.umn.edu/instruments/eds_on_sem_primer.pdf. letzter Aufruf am 16.04.2015.

[20] Inc. X-Ray Optical Systems. *X-ray Fluorescence (XRF)*. http://www.xos.com/technologies/xrf/. letzter Aufruf am 16.04.2015.

[21] Heike Loechel, Christoph Braig, Maria Brzhezinskaya, Frank Siewert, Peter Baumgaertel, Alexander Firsov, and Alexei Erko. *Femtosecond high-resolution hard X-ray spectroscopy using reflection zone plates*. *Optics Express*, 23:8788–8799, 2015.

[22] Christoph Braig, Heike Loechel, Alexander Firsov, Maria Brzhezinskaya, Aljosa Hafner, Jens Rehanek, Michael Wojcik, Albert Macrander, Lahsen Assoufid, and Alexei Erko. *Hard x-ray spectroscopy and imaging by a reflection zone plate in the presence of astigmatism*. *Optics Letters*, 41:29–32, 2016.

[23] M. Sanchez del Rio, A. Ya. Faenov, T.A. Pikuz, A. Souvorov, and A.K. Freund. *Hard X-Ray Reflectivity Of Spherically Bent Mica Crystals*. *AIP Conf. Proc.*, 521:287, 2000.

[24] Rolf Mitzner et al. *L-edge X-ray absorption spectroscopy of dilute systems relevant to metalloproteins using an X-ray free-electron laser*. *The Journal of Physical Chemistry Letters*, 4(21):3641–3647, 2013.

7 Annex

7.1 Local Grating Period

Starting from

$$d = \frac{mR_2'\Delta\lambda}{\Delta h_d \sin\beta}, \tag{7.1}$$

implementing the grating equation

$$d\cos\alpha - \cos\beta = m\lambda \tag{7.2}$$

leads to a quadratic equation for the local grating period d by

$$d = \frac{mR_2'\Delta\lambda}{\Delta h_d\sqrt{1-\cos^2\beta}} \tag{7.3}$$

$$\Leftrightarrow \quad d = \frac{mR_2'\Delta\lambda}{\Delta h_d\sqrt{1-\left(\cos\alpha - \frac{m\lambda}{d}\right)^2}} \tag{7.4}$$

$$\Leftrightarrow \quad d\sqrt{1-\left(\cos\alpha - \frac{m\lambda}{d}\right)^2} = \frac{mR_2'\Delta\lambda}{\Delta h_d} \tag{7.5}$$

$$\Leftrightarrow \quad d^2\cdot\left(1-\left(\cos\alpha - \frac{m\lambda}{d}\right)^2\right) = \left(\frac{mR_2'\Delta\lambda}{\Delta h_d}\right)^2 \tag{7.6}$$

$$\Leftrightarrow \quad d^2 - d^2\cos^2\alpha + 2\cos\alpha m\lambda d - m^2\lambda^2 = \left(\frac{mR_2'\Delta\lambda}{\Delta h_d}\right)^2 \tag{7.7}$$

$$\Leftrightarrow \quad d^2\left(1-\cos^2\alpha\right) + 2\cos\alpha m\lambda d - m^2\lambda^2 = \left(\frac{mR_2'\Delta\lambda}{\Delta h_d}\right)^2 \tag{7.8}$$

$$\Leftrightarrow \quad d^2\sin^2\alpha + 2\cos\alpha m\lambda d - m^2\lambda^2 = \left(\frac{mR_2'\Delta\lambda}{\Delta h_d}\right)^2 \tag{7.9}$$

$$\Leftrightarrow \quad d^2 + 2\frac{\cos\alpha}{\sin^2\alpha}m\lambda\cdot d - \frac{m^2\lambda^2 + \left(\frac{mR_2'\Delta\lambda}{\Delta h_d}\right)^2}{\sin^2\alpha} = 0. \tag{7.10}$$

Solved with the p,q-formula this results in

$$\Rightarrow \qquad d_{1,2} = -\frac{\cos\alpha}{\sin^2\alpha} m\lambda \pm \sqrt{\left(\frac{\cos\alpha}{\sin^2\alpha} m\lambda\right)^2 + \frac{m^2\lambda^2 + \left(\frac{mR_2'\Delta\lambda}{\Delta h_d}\right)^2}{\sin^2\alpha}} \tag{7.11}$$

$$= -\frac{\cot\alpha}{\sin\alpha} m\lambda \pm \frac{\lambda|m|}{\sin\alpha}\sqrt{\cot^2\alpha + \left(1 + \left(\frac{R_2'}{\Delta h_d}\frac{\Delta\lambda}{\lambda}\right)^2\right)} \tag{7.12}$$

$$= -\frac{\lambda|m|}{\sin\alpha}\left(\frac{m}{|m|}\cot\alpha \pm \sqrt{1 + \cot^2\alpha + \left(\frac{R_2'}{\Delta h_d}\frac{\Delta\lambda}{\lambda}\right)^2}\right) \tag{7.13}$$

$$\Leftrightarrow \qquad d_{1,2} = \frac{\lambda|m|}{\sin\alpha}\left(-\frac{m}{|m|}\cot\alpha \mp \sqrt{1 + \cot^2\alpha + \left(\frac{R_2'}{\Delta h_d}\frac{\Delta\lambda}{\lambda}\right)^2}\right). \tag{7.14}$$

There are two solutions to this problem, which correspond to the two cases of negative and positive diffraction orders. In the input of equation 7.1 the diffration order m is clearly defined including its algebraic sign, but in the transformation from 7.1 to 7.3 there is a squaring step, where this uniqueness is lost. By defining the local grating period as a positive value though, 7.3 reduces to

$$d = \frac{\lambda|m|}{\sin\alpha}\left[-\frac{m}{|m|}\cot\alpha + \sqrt{1 + \cot^2\alpha + \left(\frac{R_2'}{\Delta h_d}\frac{\Delta\lambda}{\lambda}\right)^2}\right], \tag{7.15}$$

with a positive root term.

7.2 Fresnel Zone Edge Equation

By inserting equations 3.30 and 3.31 into 3.22 and the fact that $\Delta p = n\lambda/2$, a rather long euqation can be derived:

$$\sqrt{x^2 + (R_1 \cdot cos(\theta) - y)^2 + (R_1 \cdot sin(\theta))^2} + \sqrt{x^2 + (R_2 \cdot cos(\theta) - y)^2 + (R_2 \cdot sin(\theta))^2}$$
$$= R_1 + R_2 + n \cdot \frac{\lambda}{2},$$

which can be transformed as follows:

Squaring the equation and expanding it gives

$$\begin{aligned}
&2x^2 + 2y^2 + R_1^2 + R_2^2 - 2ycos(\theta) \cdot (R_1 + R_2) \\
&+ 2 \cdot \sqrt{(x^2 + y^2 + R_1^2 - 2yR_1 \cdot cos(\theta)) \cdot \ (x^2 + y^2 + R_2^2 - 2yR_2 \cdot cos(\theta))} \\
&= (R_1 + R_2 + n \cdot \frac{\lambda}{2})^2.
\end{aligned}$$

By isolating the root term and another squaring this transforms to

$$\begin{aligned}
&4 \cdot (R_1^2 + x^2 + y^2 - 2R_1ycos(\theta)) \cdot (R_2^2 + x^2 + y^2 - 2R_2ycos(\theta)) \\
&= (n \cdot \frac{\lambda}{2} + R_1 + R_2 + 2(R_1 + R_2) \cdot ycos(\theta) - (R_1^2 + R_2^2 + 2 \cdot (x^2 + y^2)))^2.
\end{aligned}$$

When all brackets are fully expanded there will be terms with x and y up to a power of 4,

$$\begin{aligned}
&4R_1^2R_2^2 + 4R_1^2x^2 + 4R_2^2x^2 + 4x^4 + 4R_1^2y^2 + 4R_2^2y^2 + 8x^2y^2 + 4y^4 \\
&- 8R_1^2R_2ycos(\theta) - 8R_1R_2^2ycos(\theta) - 8R_1x^2ycos(\theta) - 8R_2x^2ycos(\theta) - 8R_1y^3cos(\theta) \\
&- 8R_2y^3cos(\theta) + 16R_1R_2y^2(cos(\theta))^2 \\
&= (n \cdot \frac{\lambda}{2})^2n^2 + 2n \cdot \frac{\lambda}{2}R_1 + R_1^2 - 2n \cdot \frac{\lambda}{2}R_1^2 - 2R_1^3 \\
&+ R_1^4 + 2n \cdot \frac{\lambda}{2}R_2 + 2R_1R_2 - 2R_1^2R_2 + R_2^2 - 2n \cdot \frac{\lambda}{2}R_2^2 \\
&- 2R_1R_2^2 + 2R_1^2R_2^2 - 2R_2^3 + R_2^4 - 4n \cdot \frac{\lambda}{2}x^2 - 4R_1x^2
\end{aligned}$$

$$\begin{aligned}
&+ 4R_1^2x^2 - 4R_2x^2 + 4R_2^2x^2 + 4x^4 - 4n \cdot \frac{\lambda}{2}y^2 - \\
&4R_1y^2 + 4R_1^2y^2 - 4R_2y^2 + 4R_2^2y^2 + 8x^2y^2 + 4y^4 + 4n \cdot \frac{\lambda}{2}R_1ycos(\theta) + 4R_1^2ycos(\theta) - \\
&4R_1^3ycos(\theta) + 4n \cdot \frac{\lambda}{2}R_2ycos(\theta) + 8R_1R_2ycos(\theta) - 4R_1^2R_2ycos(\theta) + 4R_2^2ycos(\theta) \\
&- 4R_1R_2^2ycos(\theta) - 4R_2^3ycos(\theta) - 8R_1x^2ycos(\theta) - 8R_2x^2ycos(\theta) - 8R_1y^3cos(\theta) \\
&- 8R_2y^3cos(\theta) + 4R_1^2y^2(cos(\theta))^2 + 8R_1R_2y^2(cos(\theta))^2 + 4R_2^2y^2(cos(\theta))^2,
\end{aligned}$$

which all cancel out exept the quadratic terms.

$$
\begin{aligned}
&-(n\cdot\frac{\lambda}{2})^4-4(n\cdot\frac{\lambda}{2})^3R_1-4(n\cdot\frac{\lambda}{2})^2R_1^2-4(n\cdot\frac{\lambda}{2})^3R_2-12(n\cdot\frac{\lambda}{2})^2R_1R_2-8n\cdot\frac{\lambda}{2}R_1^2R_2\\
&-4(n\cdot\frac{\lambda}{2})^2R_2^2-8n\cdot\frac{\lambda}{2}R_1R_2^2+4(n\cdot\frac{\lambda}{2})^2x^2+8n\cdot\frac{\lambda}{2}R_1x^2+4R_1^2x^2+8n\cdot\frac{\lambda}{2}R_2x^2\\
&+8R_1R_2x^2+4R_2^2x^2+4(n\cdot\frac{\lambda}{2})^2y^2+8n\cdot\frac{\lambda}{2}R_1y^2+4R_1^2y^2+8n\cdot\frac{\lambda}{2}R_2y^2+8R_1R_2y^2\\
&+4R_2^2y^2-4(n\cdot\frac{\lambda}{2})^2R_1ycos(\theta)-8n\cdot\frac{\lambda}{2}R_1^2ycos(\theta)-4(n\cdot\frac{\lambda}{2})^2R_2ycos(\theta)\\
&-16n\cdot\frac{\lambda}{2}R_1R_2cos(\theta)-16R_1^2R_2ycos(\theta)-8n\cdot\frac{\lambda}{2}R_2^2ycos(\theta)-16R_1R_2^2ycos(\theta)\\
&-4R_1^2y^2(cos(\theta))^2+8R_1R_2y^2(cos(\theta))^2-4R_2^2y^2(cos(\theta))^2=0
\end{aligned}
$$

Now, the y^2, x^2 and y terms can be summed up:

$$
\begin{aligned}
4y^2\cdot(R_1+R_2+n\cdot\frac{\lambda}{2}+(R_1-R_2)(cos(\theta)))(R_1+R_2+n\cdot\frac{\lambda}{2}+(R_2-R_1)(cos(\theta)))&\\
+4x^2\cdot(R_1+R_2+n\cdot\frac{\lambda}{2})^2&\\
+4y\cdot(n\cdot\frac{\lambda}{2}+2R_1)(n\cdot\frac{\lambda}{2}+2R_2)(r1+r2)&\\
-n\cdot\frac{\lambda}{2}\cdot(n\cdot\frac{\lambda}{2}+2R_1)(n\cdot\frac{\lambda}{2}+2R_2)(R_1+R_2+n\cdot\frac{\lambda}{2}+R_1+R_2)&\\
=0&
\end{aligned}
$$

With the abbreviation $K_n=R_1+R_2+n\cdot\frac{\lambda}{2}$ this simplifies to

$$
\begin{aligned}
4y^2\cdot(K_n+(R_1-R_2)(cos(\theta)))(K_n+(R_2-R_1)(cos(\theta)))&\\
+4x^2\cdot K_n^2+4y\cdot(n\cdot\frac{\lambda}{2}+2R_1)(n\cdot\frac{\lambda}{2}+2R_2)(r1+r2)&\\
-n\cdot\frac{\lambda}{2}\cdot(n\cdot\frac{\lambda}{2}+2R_1)(n\cdot\frac{\lambda}{2}+2R_2)(K_n+R_1+R_2).&\\
=0&
\end{aligned}
$$

This equation has the form

$$K_1y^2+K_2y+K_3x^2+K_4=0.$$

7.3 Program Code (Core Calculation of Fresnel Zones)

```
# ======================================================================== #
#                    RZP Parameter calculation
# ======================================================================== #


PLANCK_CONSTANT = D('4.135667516e-15') # in eV*s
SPEED_OF_LIGHT = 299792458 # in m/s
PI = D('3.14159265358979323846264338327950288419716939937 5')

def energy_to_lambda(energy):
    """return lambda in microns. """
    if not isinstance(energy, (D, int)):
        raise ValueError('For␣highest␣precision,␣only␣integer␣or␣' +
            '␣decimal␣float␣are␣allowed')
    return PLANCK_CONSTANT * SPEED_OF_LIGHT / energy * 1000000

cdef cos(x):
    """Return the cosine of x as measured in radians.

    >>> print cos(Decimal('0.5'))
    0.87758256189037271611628158 26
    >>> print cos(0.5)
    0.87758256189
    >>> print cos(0.5+0j)
    (0.87758256189+0j)

    """
    getcontext().prec += 2
    i, lasts, s, fact, num, sign = 0, 0, 1, 1, 1, 1
    while s != lasts:
        lasts = s
        i += 2
        fact *= i * (i-1)
        num *= x * x
        sign *= -1
        s += num / fact * sign
    getcontext().prec -= 2
    return +s

cdef sin(x):
    """Return the sine of x as measured in radians.

    >>> print sin(Decimal('0.5'))
    0.47942553860420300027328793 52
    >>> print sin(0.5)
    0.479425538604
    >>> print sin(0.5+0j)
    (0.479425538604+0j)
```

```
    """
    getcontext().prec += 2
    i, lasts, s, fact, num, sign = 1, 0, x, 1, x, 1
    while s != lasts:
        lasts = s
        i += 2
        fact *= i * (i-1)
        num *= x * x
        sign *= -1
        s += num / fact * sign
    getcontext().prec -= 2
    return +s

cdef class ZoneCalculator:
    # fields declaration:
    cdef:
        # all fields are cdecimal.Decimal objects:
        readonly object _r1, _r2, _theta
        readonly object _e, _a0, _svec, _qvec, _p1
        readonly object _phi, _lambda, _x_stretch_factor
        readonly object _xwidth_bot, _xwidth_top, _ymin, _ymax,
    cdef int _nmin, _nmax
    # the last result calculated with calc_RZP_parameters...
    cdef readonly object last_result
    # instance of the GDSWriter class
    cdef GDSWriter _gds
    # counts the number of RZPs written to file. User can also make prediction
    # of this number, which allows writing the main cell in the beginning
    cdef int _rzp_counter, _rzp_counter_prediction
    # whether the main cell has already been written
    cdef bint _main_written

    # _reference_p1 is necessary if multiple RZPs (with different distance_r1)
    # are added to same GDS-File. By default, every RZP has its own coordinate
    # system where the origin is in the center of the zeroth zone.
    # When the first RZP is calculated (with calc_RZP_parameters...),
    # _reference_p1 is calculated, which is the the distance to the source,
    # projected onto the RZP plane of this first RZP.
    # Following RZPs (calculated by subsequent calls to calc_RZP_parameter)
    # will be shifted in such a way, that the source point is always on the
    # same spot in space, regardless of the given distance_r1 parameter.
    # This shift will be computed and added in write_zones.
    cdef readonly object _reference_p1

    # The user can specify custom polygons by calling
    # ZoneCalculator.write_polygon() or ZoneCalculator.write_rectangle(),
    # which will be written to the gds file when the ZoneCalculator object is
    # destroyed. Each custom polygon is an item in the following list; each
    # item is a (number_of_points, 2)-sized numpy ndarray of floats:
    cdef list _custom_polygon_points_list
    # Each of the custom polygons can be designated a layer, which is saved
    # in the following list (one item (integer) for every custom polygon):
```

```
cdef list _custom_polygon_layers_list


def __init__(self):
    """This class calculates the axes and offsets of ellipses forming a
    reflection zone plate's (RZP) zone borders. After initializing the
    class, the method 'calc_RZP_parameters' can be called to get these
    values for the ellipses intersecting a given rectangle (off-axis-RZP).

    """
    # these fields will be initialized in calc_RZP_parameters:
    self._r1 = D(0)
    self._r2 = D(0)
    self._theta = D(0)
    self._xwidth_bot = D(-1)
    self._xwidth_top = D(-1)
    self._ymin = D(0)
    self._ymax = D(0)
    self._lambda = D(-1)
    self._phi = 0
    self.last_result = None
    self._gds = None
    self._rzp_counter = 0
    self._rzp_counter_prediction = 0
    self._main_written = False
    self._reference_p1 = None
    self._x_stretch_factor = 1.0

    self._custom_polygon_points_list = []
    self._custom_polygon_layers_list = []

def __dealloc__(self):
    if self._rzp_counter != 0 and not self._main_written:
        self._write_main_cell(self._rzp_counter)
    elif self._rzp_counter != self._rzp_counter_prediction:
        print ('Warning: Number of RZPs written does not match number ' +
               'given in setup_gds. GDS file is corrupted.')
    self._write_custom_cell()

cdef _write_main_cell(self, int num_rzp):
    if self._main_written:
        # main cell already written
        return

    cdef char cellname[20] # this length shouldn't be exceeded
    cdef int i, slen
    self._gds._new_cell('main', 4)
    for i in range(num_rzp):
        slen = io.sprintf(cellname, 'RZP%04i', i)
        self._gds._add_reference(
            cellname, slen)
    # add reference to cell where custom polygons will be added:
    self._gds._add_reference("custom_polygons", 15)
```

```
        self._main_written = True

    cdef _write_custom_cell(self):
        """Writes the cell with the custom polygons to file.
        Should only be called from __dealloc__, i.e. when no more custom
        polygons can be added by user."""
        self._gds._new_cell('custom_polygons', 15)
        cdef int num_polygons = len(self._custom_polygon_points_list)
        cdef int i
        for i in range(num_polygons):
            self._gds.add_polygon_to_cell(
                self._custom_polygon_points_list[i],
                layer=0 )

    cdef get_semi_major_axis(self, point):
        """Return the semi-major axis of an ellipsoid with the same
        focal distance defined by the geometry, such that the ellipsoid
        intersects point. point is a vector with length 3 (a numpy array,
        python tuple or list).

        """
        x = point[0]
        y = point[1]
        z = point[2]
        p = (x**2 + y**2 + z**2 + self._e**2) / 2
        return (p + (p**2 - self._e**2 * x**2).sqrt()).sqrt()

    def calc_RZP_parameters(
            self, distance_r1, distance_r2, theta,
            xwidth, ymin, ymax, energy, phi = 0,
            x_stretch_factor=1):

        """Calculate and return the three ellipse_parameters (y-shift,
        half width and half height of ellipse) for each ellipse intersecting
        the clip rectangle.
        The returned list (n x 3 numpy matrix) contains a line for each
        ellipse.

        Parameters:
        distance_r1 : Distance from the RZP's center to the source, in mm
        distance_r2 : Distance from the RZP's center to the detector, in mm
        theta       : Reflection angle (angle between beam and RZP-surface), in degrees
        xwidth      : Width of clip rectangle in mm
        ymin        : Lower boundary of clip rectangle in mm
        ymax        : Upper boundary of clip rectangle in mm
        energy      : Photon energy in eV

        Optional parameter:
        phi         : Phase-shift in microns

        """
        return self.calc_RZP_parameters_trapezoid(
            distance_r1, distance_r2, theta, xwidth, xwidth, ymin, ymax,
```

```
            energy, phi, x_stretch_factor)

    def calc_RZP_parameters_trapezoid(
            self, distance_r1, distance_r2, theta,
            xwidth_bottom, xwidth_top, ymin, ymax, energy, phi = 0,
            x_stretch_factor=1):
        """Calculate and return the three ellipse_parameters (y-shift,
        half width and half height of ellipse) for each ellipse intersecting
        the clip trapezoid.
        The returned list (n x 3 numpy matrix) contains a line for each
        ellipse.

        Parameters:
        distance_r1 : Distance from the RZP's center to the source, in mm
        distance_r2 : Distance from the RZP's center to the detector, in mm
        theta       : Reflection angle (angle between beam and RZP-surface), in degrees
        xwidth_bottom : Width at bottom of clip trapezoid in mm
        xwidth_top  : Width at top of clip trapezoid in mm
        ymin        : Lower boundary of clip rectangle in mm
        ymax        : Upper boundary of clip rectangle in mm
        energy      : Photon energy in eV

        Optional parameter:
        phi         : Phase-shift in microns

        """
        # internally, all lengths are saved in microns:
        self._r1 = D(distance_r1) * 1000
        self._r2 = D(distance_r2) * 1000
        self._theta = D(theta) / 180 * PI
        if ymin == ymax or (xwidth_top == 0 and xwidth_bottom == 0):
            raise ValueError('Please␣specify␣non-empty␣RZP␣area.')
        elif ymin < ymax:
            self._xwidth_bot = D(xwidth_bottom) * 1000
            self._xwidth_top = D(xwidth_top) * 1000
            self._ymin = D(ymin) * 1000
            self._ymax = D(ymax) * 1000
        else:
            # switch top and bottom:
            self._xwidth_top = D(xwidth_bottom) * 1000
            self._xwidth_bot = D(xwidth_top) * 1000
            self._ymin = D(ymax) * 1000
            self._ymax = D(ymin) * 1000
        self._lambda = energy_to_lambda(D(energy))
        self._phi = D(phi)
        self._x_stretch_factor = D(x_stretch_factor)

        # ellipsoid focal distance e:
        self._e = (
            self._r1**2 + self._r2**2 +
            2 * self._r1 * self._r2 * cos(2 * self._theta)).sqrt() / 2

        # semi-major axis a (along line connecting source and detector)
```

```
# of the ellipsoid which just touches the surface at the nearest point:
# This is the smallest ellipsoid which intersects the surface - it will
# be used as reference length for calculating the other ellipsoids.
self._a0 = (self._r1 + self._r2) / 2

# x-component of the point q where the above ellipsoid with _a0 touches
# the surface:
# This point will be the origin of the surface
qx = (self._r1**2 - self._r2**2) / (4 * self._e)
# complete point q:
self._qvec = np.array(
    [qx, -(self._r1**2 - (self._e + qx)**2).sqrt(), 0])

# surface basis vector s:
# (The second basis vector is trivial: r = (0, 0, 1))
h1 = (self._e + qx) / self._r1
h2 = (1 - h1**2).sqrt()
ca = cos(self._theta)
sa = sin(self._theta)
self._svec = np.array([h1*ca + h2*sa, h1*sa - h2*ca, 0])

# projection of source point on RZP-surface:
# (will be needed in write_zones if RZP must be rotated)
self._p1 = <double>(self._r1 * ca)

# self._reference_p1 will be used to put multiple RZPs on same
# coordinate system, using the first RZP as reference
if self._reference_p1 is None:
    self._reference_p1 = self._p1

# calculate amin and amax, i.e. the semi-major axes of the smallest
# and biggest ellipsoid which still touches the clipping rectangle
testpoint = self._qvec + self._ymin*self._svec
amin1 = self.get_semi_major_axis(testpoint)
testpoint = (self._qvec + self._ymin*self._svec +
        (0, 0, self._xwidth_bot / 2 / self._x_stretch_factor))
amin2 = self.get_semi_major_axis(testpoint)

testpoint = self._qvec + self._ymax*self._svec
amax1 = self.get_semi_major_axis(testpoint)
testpoint = (self._qvec + self._ymax*self._svec +
        (0, 0, self._xwidth_top / 2 / self._x_stretch_factor))
amax2 = self.get_semi_major_axis(testpoint)

if self._ymin < 0 and self._ymax > 0:
    amax = max(amin1, amin2, amax1, amax2)
    amin = self._a0
else:
    amin = min(amin1, amin2, amax1, amax2)
    amax = max(amin1, amin2, amax1, amax2)

# using amin and amax from above and the equation
# 2*a(n) = 2*a0 + phi + n*lambda/2 (which is essentially the Fresnel-
```

```
        # relation for constructively interfering waves reflected at different
        # ellipsoids with semi-axes a(n), put into relation to our reference
        # length a0 and an optional phase shift phi),
        # one gets nmin and nmax. Later, iterating between these two values
        # will deliver all RZP zone boundaries in the clipping rectangle.
        self._nmin = int(np.ceil(
            float(4 * (amin - self._a0 - self._phi/2) / self._lambda)))
        self._nmax = int(np.floor(
            float(4 * (amax - self._a0 - self._phi/2) / self._lambda)))

        # the first ellipse must always have an even ellipse number;
        # This way one can ensure that always the same zones are 'filled'
        # independent of the chosen RZP boundaries:
        if self._nmin % 2 != 0:
            self._nmin -= 1

        print('calculating ellipses %i to %i.' % (self._nmin, self._nmax))

        # iterate through all n between nmin and nmax and create the results
        # list:
        self.last_result = self.get_intersection_ellipse_parameters(
                    self._nmin, self._nmax)

        return self.last_result

    cdef get_intersection_ellipse_parameters(self, int nmin, int nmax):
        """Using the ellipsoids with the focal distance defined by the
        geometry and semi-major axes a(n) = a0 + phi/2 + n*lambda/4,
        for n between nmin and nmax (inclusive), calculate the intersections
        these ellipsoids have with the RZP-surface, which are 2D-ellipses.
        Return the parameters of these 2D-ellipses, which are:
            ellipse-origin's y-component (x-component is always 0),
            semi-axis in x-direction (a) and
            semi-axis in y-direction (b).
        The returned list is a (n x 3) numpy matrix, containing a line (with
        the three values above) for each ellipse (i.e. for each n).

        """
        cdef:
            # all variables are cdecimal.Decimal objects:
            e_squared = self._e**2
            a_0 = self._a0 + self._phi / 2
            a_m = self._lambda / 4
            qx = self._qvec[0]
            qy = self._qvec[1]
            sx = self._svec[0]
            sy = self._svec[1]

        cdef np.float64_t y0, A, B

        cdef np.ndarray[np.float64_t, ndim=2] results = np.zeros(
            (nmax - nmin + 1, 3), dtype = np.float64)
        cdef int n
```

```
        cdef int i = 0
        for n in range(nmin, nmax + 1):
            if (n - nmin) % 2000 == 0 and n != nmin:
                print('progress: calculating ellipse %i of %i' %
                      (n-nmin, nmax-nmin+1))
            a_squared = (a_0 + a_m * n)**2
            b_squared = (a_squared - e_squared)
            Drr = 1 / b_squared
            Dss = sx**2 / a_squared + sy**2 / b_squared
            Dqs = (qx * sx / a_squared +
                   qy * sy / b_squared)
            Dqq = qx**2 / a_squared + qy**2 / b_squared

            d1 = 1 - Dqq + Dqs**2 / Dss
            if d1 < 1E-25:
                # if the ellipsoid just barely touches the plane, which is
                # the case for an ellipsoid with a=a0, d1 must be zero.
                # Due to rounding errors, this value might not be reached
                # exactly, and d1 can even become negative, which would be
                # problematic in the calculation of A and B.
                y0 = A = B = 0.0
            else:
                y0 = <np.float64_t>(-Dqs / Dss)
                # y0 can be exactly 0 in theory, but here, it will hardly be
                # exact due to rounding errors. Since this will be a problem
                # later on (e.g. during the final RZP's clipping with a
                # boundary, y0 needs to be tested whether it is 0) and to
                # produce a nicer output, we should approximate to zero here.
                # It should be perfectly save to clip values smaller than
                # 1e-3 nm to zero:
                if math.fabs(y0) < 1e-6:
                    y0 = 0.0
                A  = <np.float64_t>((d1 / Drr).sqrt() * self._x_stretch_factor)
                B  = <np.float64_t>((d1 / Dss).sqrt())
            results[i, 0] = y0
            results[i, 1] = A
            results[i, 2] = B
            n += 1
            i += 1
        print('progress: calculated %i ellipses' % (nmax-nmin+1))
        return results

    def setup_gds(
            self, filename, int rzp_count = 0,
            double unit=1.0e-6, double precision=1.0e-9):
        """
        Initialize a GDSII file for writing the RZP design to.

        Parameters:

            filename    : name of the created GDSII file (please incl. '.gds')
            rzp_count   : number of RZP which will be written to file:
                          It is essential that this number equals the number of
```

```
                    later calls to write_zones(). It can also be 0
                    (default value), in which case the main cell will be
                    written at the end, but then file cannot be previewed
                    during writing.
        unit        : GDS file units, in meters (default: 1.0e-6)
        precision   : GDS file precision, in meters (default: 1.0e-10)

    """
    self._gds = GDSWriter(filename, unit, precision)
    if rzp_count != 0:
        self._rzp_counter_prediction = rzp_count
        self._write_main_cell(self._rzp_counter_prediction)

def write_zones(
        self, unsigned int num_points, double rotation = 0,
        bint fill_odd_zones = False, double q = 0.38,
        unsigned short layer=0, unsigned short datatype=0,
        bint do_clipping = True):
    """
    Write the RZP structure to the GDSII file initialized by setup_gds().
    calc_RZP_parameters must have been called before.

    Parameters:

        num_points      : number of points a single zone is made up of
        rotation        : rotation of the RZP, in degrees (default: 0)
        fill_odd_zones  : If True, odd zones are filled. By default, even
                          zones are filled
        q               : ellipse polygon point distribution factor
                          (for more details see below); default value: 0.38
        layer           : layer used for the RZP in the GDS file (default: 0)
        datatype        : datatype used for the RZP in the GDS file
                          (default: 0)
        do_clipping     : If False, the zones are not clipped by the
                          boundary trapezoid. Default is True.

    q is a value between -1 and 1, smoothly changing the distribution of
    polygon points along the ellipse's boundary.
    If q = 0, the parameter t increases in constant steps (in the ellipse
    parameterization (x, y)=(a*cos[t], b*sin[t])). Its the same as a
    circle drawn with equidistant points which is then stretched. If
    distributed this way, there are too many points at flat areas of the
    polygon while there are too few at round areas (at big semi-major
    axis), making them look edgy if using too few points.
    If q = -1, the points are distributed in a way that the
    angles between lines connecting the ellipse's origin with the points
    are constant, i.e each line is separated by 2pi/numpoints. This
    way, there are even fewer points at the round areas.
    If q = +1, the points are distributed in a way that the angles
    of the normals to the ellipse surface at each point have constant
    difference. This way, there are too few points at flat areas.
    It turns out the best looking value for q is somewhere around 0.38.
```

```
    """

    cdef char cellname[20] # this length shouldn't be exceeded
    cdef int i, npts, slen
    cdef np.ndarray[np.float64_t, ndim=2, mode="c"] rzp_parameter
    cdef double x_shift
    cdef unsigned int num_ellipses, istart

    if self.last_result is None:
        raise ValueError(
            "ZoneCalculator's results contained no ellipses. " +
            "Please run ZoneCalculator.calc_RZP_parameters before.")
    if self._gds is None:
        raise ValueError("Please run ZoneCalculator.setup_gds before.")
    rzp_parameter = self.last_result
    num_ellipses = rzp_parameter.shape[0]
    if rzp_parameter.shape[1] != 3:
        raise ValueError(
            "ZoneCalculator's result does not have shape (num_ellipses, 3)")
    if num_points > MAX_POINTS_PER_POLYGON:
        raise ValueError(("Polygons with more than %i points are not " +
            "supported by the GDSII format.") % MAX_POINTS_PER_POLYGON)

    zpm = ZonePolygonMaker(self._gds, num_points,
        self._xwidth_bot, self._xwidth_top,
        self._ymin, self._ymax, q)

    # calculate x and y shift of zone plate if rotation != 0, so that the
    # rotation is around projection of source point on RZP-plane.
    # The additional y-shift is due to different coordinate systems if
    # multiple RZP with different r1 are added to same GDS file
    # (see comment for self._reference_p1 above __init__).
    x_shift = -self._p1 * math.sin(math.M_PI * rotation / 180.)
    y_shift = (self._p1 * (math.cos(math.M_PI * rotation / 180.) - 1)
               +  self._p1 - self._reference_p1)

    if fill_odd_zones:
        istart = 1
    else:
        istart = 0

    # make rzp cell with references:
    # individual zone cells will be created afterwards
    slen = io.sprintf(cellname, 'RZP%04i', self._rzp_counter)
    self._gds._new_cell(cellname, slen)
    for i in range(np.ceil((num_ellipses / 2) / MAX_ZONES_PER_CELL)):
        slen = io.sprintf(cellname, 'zone%04i_%06i', self._rzp_counter, i)
        self._gds._add_reference(
            cellname, slen,
            originx = x_shift,
            originy = y_shift,
            mirror=0, magnification=1,
            rotation=rotation)
```

```
            self._gds._add_reference(
                cellname, slen,
                originx = x_shift,
                originy = y_shift,
                mirror=1, magnification=1,
                rotation=180 + rotation)
##      for i in range(num_ellipses / 2):
##          slen = io.sprintf(cellname, 'zone%08i', i)
##          self._gds._add_reference(cellname, slen, 0, 0, 0, 1, rotation=0)
##          self._gds._add_reference(
##              cellname, slen, 0, 0, mirror=1, magnification=1,
##              rotation=180)
        # add rectangle:
##      cdef double xbh = self._xwidth_bot / 2.0
##      cdef double xth = self._xwidth_top / 2.0
##      cdef double ptbuffer[8]
##      ptbuffer[0] = -xbh; ptbuffer[1] = self._ymin
##      ptbuffer[2] = xbh; ptbuffer[3] = self._ymin
##      ptbuffer[4] = xth; ptbuffer[5] = self._ymax
##      ptbuffer[6] = -xth; ptbuffer[7] = self._ymax
##      self._gds._add_polygon_to_cell(ptbuffer, 4, layer = 1)

        for i in range(num_ellipses / 2):
            # this only iterates through ellipses upto the maximum even number,
            # creating zones as pairs of ellipses. If there is one ellipse left
            # over (if num_ellipses is odd), then that last ellipse will be
            # ignored.
            if (i+1) % 2000 == 0 and i != 0:
                print('progress: writing zone %i of %i' %
                      (i + 1, num_ellipses / 2))
            # only create a new cell if current cell is full:
            if (i % MAX_ZONES_PER_CELL == 0):
                slen = io.sprintf(cellname, 'zone%04i_%06i', self._rzp_counter,
                    i / MAX_ZONES_PER_CELL)
                self._gds._new_cell(cellname, slen)
            npts = zpm._write_zone(
                &rzp_parameter[istart + 2*i,0],
                &rzp_parameter[istart + 2*i+1,0],
                layer=layer, datatype=datatype, clipping=do_clipping)
            if npts == -1:
                print('WARNING: could not write zone #{0}.'.format(i))
                print('There was an unexpected error finding the correct' +
                      'intersections with the boundary.')
                print('Please try shifting the boundaries a small amount.')
            elif npts == 0:
                print('WARNING: could not write zone #{0}.'.format(i))
                print('One ellipse had no intersections with the boundary' +
                      'or the middle line.')
                print('Please supply the exact same boundaries to the function' +
                      '"write_zones" than supplied to' +
                      'ZoneCalculator.get_RZP_parameters before.')
        print('progress: wrote %i zones to file.' % (num_ellipses / 2))
        self._rzp_counter += 1
```

```
def write_polygon(
        self, np.ndarray[double, ndim=2, mode="c"] points,
        unsigned short layer=0):
    """ Add a custom polygon to the gds file. points must be a numpy
    array of shape (number_of_points, 2) and of dtype float."""
    if points.shape[1] != 2:
        raise ValueError("Please provide points with shape (numpoints, 2)")
    if points.shape[0] > MAX_POINTS_PER_POLYGON:
        raise ValueError("Polygons with more than %i points are not " +
            "supported by the GDSII format." % MAX_POINTS_PER_POLYGON)
    self._custom_polygon_points_list.append(points.copy())
    self._custom_polygon_layers_list.append(layer)

def write_rectangle(
        self, double left, double bottom, double width, double height,
        unsigned short layer=0):
    """ Add a custom rectangle to the gds file."""
    cdef np.ndarray[double, ndim=2] points = \
        np.zeros((4, 2), dtype=np.double)
    points[0, 0] = left;          points[0, 1] = bottom
    points[1, 0] = left + width; points[1, 1] = bottom
    points[2, 0] = left + width; points[2, 1] = bottom + height
    points[3, 0] = left;          points[3, 1] = bottom + height
    self._custom_polygon_points_list.append(points)
    self._custom_polygon_layers_list.append(layer)
```

Selbständigkeitserklärung

Hiermit versichere ich an Eides statt, dass ich in der vorliegenden Dissertation mit dem Titel "Reflection Zone Plates for X-Ray Spectroscopy" alle Hilfsmittel und Hilfen angegeben habe und auf dieser Grundlage die Arbeit selbständig verfasst habe. Ich versichere, dass diese Dissertation noch nicht in einem früheren Promotionsverfahren angenommen oder als ungenügend beurteilt wurde.